RESOURCE FOR PIEZOELECTRIC SINGLE CRYSTALS

Period 1 April 1998 to 30 March 1999

Annual Report

OFFICE OF NAVAL RESEARCH
Contract No. N00014-98-1-0527

APPROVED FOR PUBLIC RELEASE –
DISTRIBUTION UNLIMITED

Reproduction in whole or in part is permitted for any purpose of the United States Government

Thomas R. Shrout

PENNSTATE

1855

THE MATERIALS RESEARCH LABORATORY
UNIVERSITY PARK, PA

REPORT DOCUMENTATION PAGE

Form Approved
OMB No. 0704-0188

Public reporting burden for this collection of information is estimated to average 1 hour per response, including the time for reviewing instructions, searching existing data sources, gathering and maintaining the data needed, and completing and reviewing the collection of information. Send comments regarding this burden estimate or any other aspect of this collection of information, including suggestions for reducing this burden, to Washington Headquarters Services, Directorate for Information Operations and Reports, 1215 Jefferson Davis Highway, Suite 1204, Arlington, VA 22202-4302, and to the Office of Management and Budget, Paperwork Reduction Project (0704-0188), Washington, DC 20503.

1. AGENCY USE ONLY *(Leave blank)*

2. REPORT DATE
30 April 1999

3. REPORT TYPE AND DATES COVERED
Annual Report 01 Apr 98 - 30 Mar 99

4. TITLE AND SUBTITLE
Resource for Piezoelectric Single Crystals

5. FUNDING NUMBERS
ONR Contract No.
N00014-98-1-0527

6. AUTHOR(S)
Thomas R. Shrout

7. PERFORMING ORGANIZATION NAME(S) AND ADDRESS(ES)
Materials Research Laboratory
The Pennsylvania State University
University Park, PA 16802

8. PERFORMING ORGANIZATION REPORT NUMBER

9. SPONSORING/MONITORING AGENCY NAME(S) AND ADDRESS(ES)
Office of Naval Research
ONR 242
Ballston Centre Tower One
800 North Quincy Street
Arlington, VA 22217-5660

Office of Naval Research
Regional Office Chicago
536 S. Clark St, Room 208
Chicago, IL 60605-1588

10. SPONSORING/MONITORING AGENCY REPORT NUMBER

11. SUPPLEMENTARY NOTES

12a. DISTRIBUTION/AVAILABILITY STATEMENT
Approved for Public Release; distribution is unlimited.

12b. DISTRIBUTION CODE

13. ABSTRACT *(Maximum 200 words)*
See following page.

14. SUBJECT TERMS

15. NUMBER OF PAGES

16. PRICE CODE

17. SECURITY CLASSIFICATION OF REPORT

18. SECURITY CLASSIFICATION OF THIS PAGE

19. SECURITY CLASSIFICATION OF ABSTRACT

20. LIMITATION OF ABSTRACT

NSN 7540-01-280-5500

Standard Form 298 (Rev 2-89)
Prescribed by ANSI Std Z39-18
298-102

GENERAL INSTRUCTIONS FOR COMPLETING SF 298

The Report Documentation Page (RDP) is used in announcing and cataloging reports. It is important that this information be consistent with the rest of the report, particularly the cover and title page. Instructions for filling in each block of the form follow. It is important to ***stay within the lines*** to meet ***optical scanning requirements.***

Block 1. Agency Use Only *(Leave blank)*.

Block 2. Report Date. Full publication date including day, month, and year, if available (e.g. 1 Jan 88). Must cite at least the year.

Block 3. Type of Report and Dates Covered. State whether report is interim, final, etc. If applicable, enter inclusive report dates (e.g. 10 Jun 87 - 30 Jun 88).

Block 4. Title and Subtitle. A title is taken from the part of the report that provides the most meaningful and complete information. When a report is prepared in more than one volume, repeat the primary title, add volume number, and include subtitle for the specific volume. On classified documents enter the title classification in parentheses.

Block 5. Funding Numbers. To include contract and grant numbers; may include program element number(s), project number(s), task number(s), and work unit number(s). Use the following labels:

C	Contract	PR	Project
G	Grant	TA	Task
PE	Program Element	WU	Work Unit Accession No.

Block 6. Author(s). Name(s) of person(s) responsible for writing the report, performing the research, or credited with the content of the report. If editor or compiler, this should follow the name(s).

Block 7. Performing Organization Name(s) and Address(es). Self-explanatory.

Block 8. Performing Organization Report Number. Enter the unique alphanumeric report number(s) assigned by the organization performing the report.

Block 9. Sponsoring/Monitoring Agency Name(s) and Address(es). Self-explanatory.

Block 10. Sponsoring/Monitoring Agency Report Number. *(If known)*

Block 11. Supplementary Notes. Enter information not included elsewhere such as: Prepared in cooperation with...; Trans. of...; To be published in.... When a report is revised, include a statement whether the new report supersedes or supplements the older report.

Block 12a. Distribution/Availability Statement. Denotes public availability or limitations. Cite any availability to the public. Enter additional limitations or special markings in all capitals (e.g. NOFORN, REL, ITAR).

DOD - See DoDD 5230.24, "Distribution Statements on Technical Documents."
DOE - See authorities.
NASA - See Handbook NHB 2200.2.
NTIS - Leave blank.

Block 12b. Distribution Code.

DOD - Leave blank.
DOE - Enter DOE distribution categories from the Standard Distribution for Unclassified Scientific and Technical Reports.
NASA - Leave blank.
NTIS - Leave blank.

Block 13. Abstract. Include a brief *(Maximum 200 words)* factual summary of the most significant information contained in the report.

Block 14. Subject Terms. Keywords or phrases identifying major subjects in the report.

Block 15. Number of Pages. Enter the total number of pages.

Block 16. Price Code. Enter appropriate price code *(NTIS only)*.

Blocks 17. - 19. Security Classifications. Self-explanatory. Enter U.S. Security Classification in accordance with U.S. Security Regulations (i.e., UNCLASSIFIED). If form contains classified information, stamp classification on the top and bottom of the page.

Block 20. Limitation of Abstract. This block must be completed to assign a limitation to the abstract. Enter either UL (unlimited) or SAR (same as report). An entry in this block is necessary if the abstract is to be limited. If blank, the abstract is assumed to be unlimited.

Abstract

This report documents work performed over the period of 01 April 1998 through 30 March, 1999 under the Office of Naval Research Contract N00014-98-1-0527. The program titled "Resource for Piezoelectric Single Crystals" combines a critical number of interdisciplinary faculty to address the areas of innovative crystal growth, novel piezoelectric materials, crystallographic and domain engineering, while investigating new application opportunities in the area of MEMs and electrooptics.

Accomplishments in the above areas include the following: *Crystal growth* of $Pb(Zn_{1/3}Nb_{2/3})O_3–PbTiO_3$ (PZN-PT) and $Pb(Mg_{1/3}Nb_{2/3})O_3–PbTiO_3$ (PMN-PT) relaxor-based ferroelectrics continues to utilize high temperature flux growth to synthesize high quality crystals with less than 1 mole% variance of $PbTiO_3$ across 1–2 inch size crystals. Alternatively, the Bridgman growth technique has been implemented for growth of nearly congruently melting PMN-PT materials.

The underlying phenomena of *crystallographic and domain engineering* of high piezoelectric activity in Relaxor-PT crystals was applied to non-PbO perovskites, including $BaTiO_3$ and Zr-modified $BaTiO_3$ crystals, the latter grown by solid state techniques. *Crystallographic engineering* of non-PbO systems resulted in piezoelectric d_{33} coefficients ranging from 350–600 pC/N and electromechanical coupling coefficients k_{33} ~ 75–85%, comparable to superior of present day polycrystalline PZT ceramics.

Novel compositions being investigated in this program include $(Pb(Yb_{1/2}Nb_{1/2})O_3–PbTiO_3$ $Na,BiTiO_3–BaTiO_3$ and $Bi(A)O_3–PbTiO_3$ (A Sc,Fe) systems, for the ultimate realization of high T_c piezoelectrics with enhanced acoustic power.

Domain investigations under various E-field conditions have revealed that polarization fatigue may be crystallographic dependent with no fatigue for [001] oriented crystals . These results may impact future thin film devices, in which minimal polarization fatigue is critical.

Thin film fabrication of the PMN-PT and PYN-PT–$PbTiO_3$ systems using pulsed laser deposition and sol-gel processing resulted in <001> oriented films with piezoelectric coefficients d_{31} ~ 180 pC/N (PMN 70/30) two to three times that reported for state-of-the-art PZT films. PYN-PT oriented films offer a high transition temperature alternative ~ 300°C versus 150°C, with remanent polarization values $> 60\ \mu C/cm^2$.

Electromechanical characterization of rhombohedral PZN-PT crystals using a combination of ultrasonic and resonant techniques has generated a complete list of dielectric (K_{ij}), piezoelectric (d_{ijk}), and elastic stiffness (C_{ijkl}) matrices using a macro symmetry of 4 mm. Issues of domain stability will be overcome using electrical biasing.

Optical characterization including refractive indices as a function of frequency and temperature for PZN-PT single crystals were determined with n_o=2.57, n_e=2.46 for 0.88 PZN-0.12 PT @ 0.633 nm. Relatively large linear E-O coefficients were obtained; r_{33}=134 pM/N, r_{31}=7 pM/N. r_{51}=462 pM/N determined using a modified Mach-Zenhder interferometer. Acousto-optic coefficients of π_0 2.5×10^{-12} Pa^{-1} resulted in a figure of merit for an Acousto-optic Scanner M($10^{-14}m^2/W$) of 56 versus 1.4 and 1.67 for $LiNbO_3$ and fiber glass, respectively. Issues of light scattering due to the engineered domain configuration in rhombohedral systems may limit the potential of these materials in bulk form.

Table of Contents

1. Introduction

This report describes the research performed over the period of 01 April 1998 through 30 March 1999 under the Office of Naval Research Contract No. N00014-98-1-0527 entitled "Resource for Piezoelectric Single Crystals." The program established a resource for the growth, characterization of evaluation of piezoelectrics for high impact defense applications, based on the recent development of crystallographically engineered Relaxor-PT single crystals, resulting in electromechanical coupling factor > 90% with E-field strains > 1%, in contrast to ~ 75% and 0.1% levels in current polycrystalline PZT ceramics, respectively.

The program combines a number of specialist faculty to address the areas of innovative growth, novel materials, crystallographic and domain engineering, and electromechanical characterization, while establishing new application opportunities in the area of MEMs and optics.

Organization of the program includes a resource coordinator and administrator, with specific thrust areas under the direction of various faculty investigators. An organization chart is given in Figure 1, including various technical support personnel comprised of graduate students, visiting scholars, post-docs, and technicians.

To provide *outreach* among the various resource members and staff, a bi-weekly seminar series was established, as highlighted in Figure 2.

Highlights of technical achievements in the main thrust areas are summarized in the following sections. Specific to each area, results in the form of published results are given in the form of appendices.

PSU/CRYSTAL RESOURCE

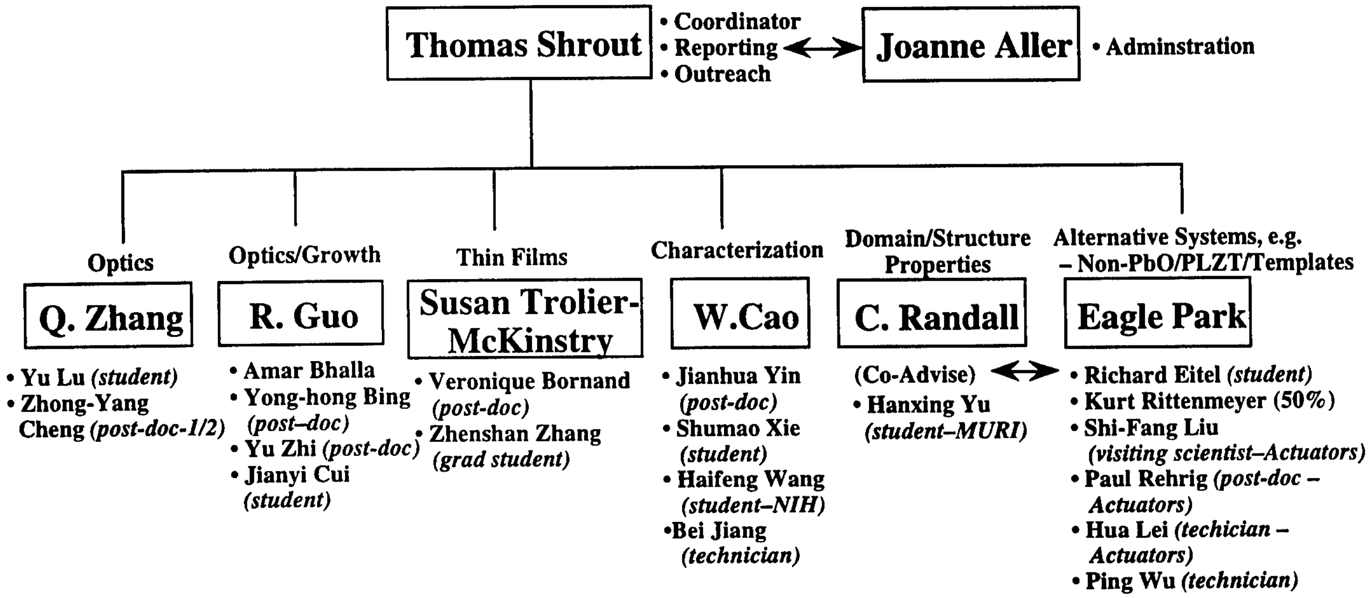

Figure 1. Piezoelectric Resource Organization Chart.

FERROELECTRIC SEMINAR (Materials 590-1)

Center for Dielectric Studies, Resource for Piezoelectric Single Crystals, and FAME Programs

Seminar Series
Thursdays, 3:00–4:30 p.m., Room 250 MRL

Date	Title	Speaker
Jan. 21	Preparation of Thin Films by the Pyrolysis Technique	Veronique Bornand
Jan. 28	Time Domain Analysis of Multilayer Structures PTCR Ceramics and Mixedness	Elena Semouchkina Chuck Kraisinger
Feb. 4	Domain Studies in Relaxor Ferroelectric Crystals Electrooptic Studies in Ferroelectric Crystals	Hanxing Yu Kurt Rittenmyer
Feb. 11	Defect Chemistry of Perovskites Reliability Studies	Yoed Tsur Edward Feng
Feb. 18	Integrated NPO Dielectrics Green Ceramic Tape as a Raw Material	Juan Nino Eric Twiname
Feb. 25	Reliability of Thin Films Dielectric Data on PZT Films	Ron Polcawich Fei Xu
March 4 (Room 189)	Single Crystal Growth and Characterization Electromechanical Characterization of Single Crystal Ferroelectrics	Shi-Fang Liu Jianhua Yin
March 11	SPRING BREAK	
March 18	Simulation of Domains Relaxor Crystal Studies	Shumao Xie Yue Wang
March 25	Dielectric and Optic Properties of Relaxor Ferroelectrics Ferroelectric Thin Films	Zhong-Yang Cheng Won-Youl Choi
April 1	Aqueous Thick Films Thin Layer Metallization	Seyit Ural Doruk Yener
April 8	Growth and Ferroelectric Properties of Pb-based Relaxors Dielectric and Piezoelectric Properties of Modified $BaTiO_3$ Crystals	Jianji Cui Yu Zhi
April 15	ONR WORKSHOP ON TRANSDUCERS	
April 22	Optical Studies of Ferroelectric Crystals Bismuth Pyrochlore Thin Films	Yu Lu Wei Ren
April 26–28	AMERICAN CERAMIC SOCIETY MEETING	
April 29	High K 0–3 Composites	Yi Bai
May 6	Dopant Effects on the Dielectric Properties of BST Dielectric Properties of $Pb,SrTiO_3$ Materials	Ang Chen Y. Somiya
May 13	To be determined	

Figure 2

2. Crystal Growth and New Systems

Flux Growth

The high temperature flux growth technique still remains the method of choice for the growth of PZN-PT crystals owing to its inherent perovskite instability, i.e. perovskite→pyrochlore transformation. As shown in Figure 3, a single point nucleation using spot cooling was used to produce PZN-PT crystals up to 2" in size, as shown in Figure 4.

Evaluation of crystal quality of flux grown PZN-PT revealed less than 1 mole% variation across 1" boules, as determined by Curie temperature variation of less than 4 degrees.

Bridgman Growth

The potential for large crystals of PMN-PT using the Bridgman growth technique arise from PMN-PTs near congruency. Hence, a commercially available Bridgman system was purchased and set up as shown in Figure 5. Crystal growth optimization is underway.

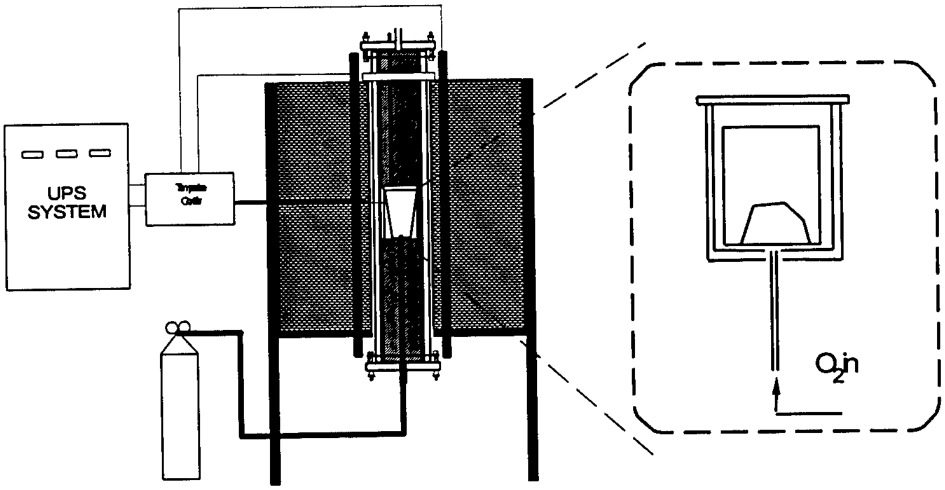

Figure 3. Schematic of high temperature flux growth system with single point nucleation.

Figure 4. An optimized flux grown crystal of PZN-PT.

Laser Heated Pedestal Growth

Following the success in growing single crystals of Pb-containing MPB compositions in the tungsten bronze (Pb,K)Nb_2O_6–(Sr,Na)Nb_2O_6 solid solution system, PMN-PT crystal growth was evaluated. To date, however, the dominant phase of the fiber crystals is pyrochlore, perhaps owing to difficulties in controlling PbO loss.

For non-lead perovskites, however, fiber crystal growth of $Ba(Ti_{1-x}Zr_x)O_3$ (x-0.13,0.20) were successfully grown. Preliminary dielectric results reveal the expected transition temperatures. Further optimization of the growth conditions is underway.

Solid State Growth (SSG)

Alternative to the flux and Bridgman growth techniques, the ability to convert a polycrystalline material into a single crystal using solid state growth has been explored for $BaTiO_3$ and Zr modified $BaTiO_3$ (see Appendices A, B, and C). Using $BaTiO_3$ crystal templates, crystals were grown and characterized. It is important to point out that $BaTiO_3$–Zr crystals grown by solid state were found to possess the same composition as the starting matrix. This is important for the possibility of growing a wide range of solid solutions.

Figure 5. Bridgman Crystal Growth System

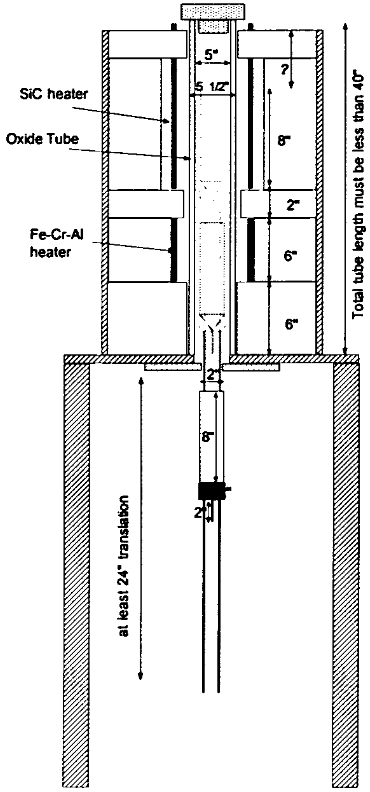

- Maximum 5″ ϕ crystal
- 2-zone furnace for engineered temperature gradient

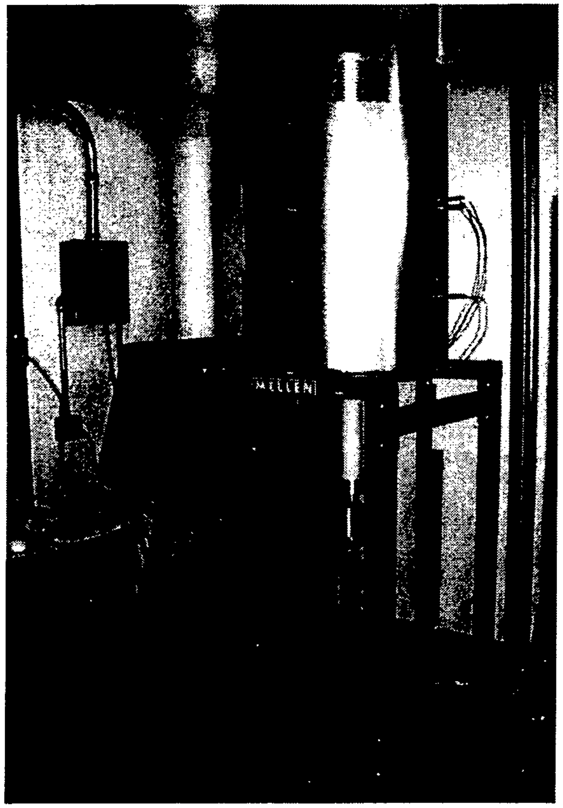

Figures 6 and 7 highlight piezoelectric d_{33} and coupling coefficients for $Ba(Zr_{0.05}(Ti_{0.95})O_3$ crystals grown by SSG. Piezoelectric d_{33} values as high as 600 pC/N and k_{31}–83% were found being comparable to PZTs as shown in Figure 8.

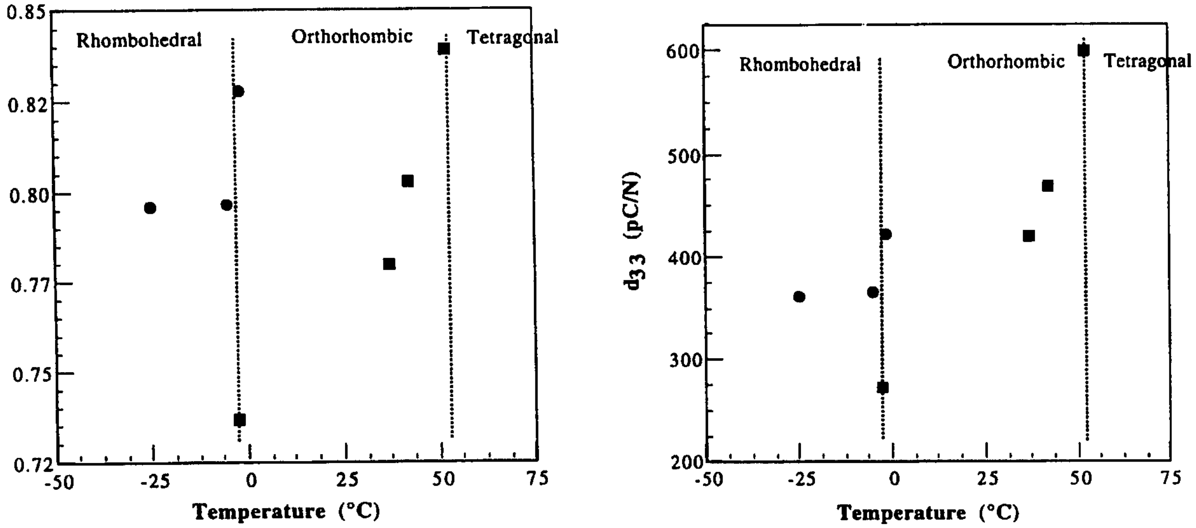

Figures 6 & 7. Electromechanical coupling and piezoelectric d_{33} from SSG $Ba(Zr_{0.05}Ti_{0.95})O_3$ Single Crystals (Room Temperature Orthorhombic).

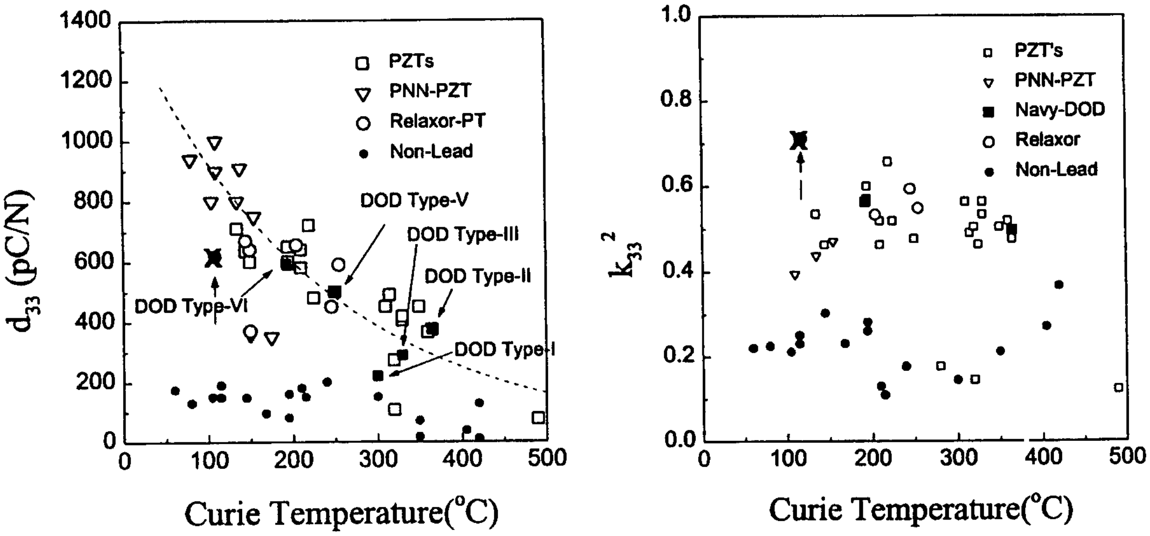

Figure 8. K_{33} and d_{33} room temperature values for both non-lead and PZTs, including BT-Zr SSG crystals (X) showing performance comparable to or better than PZT ceramics.

Future Work

Proposed work in the area of crystal growth and new compositions are summarized in the following:

- Optimization of PMN-PT by Bridgman growth and LHPG
- SSG of $Ba(Zr,Ti)O_3$ using ceramic whiskers (see Figure 9)
- Explore PMN-NBT-PT solid solutions

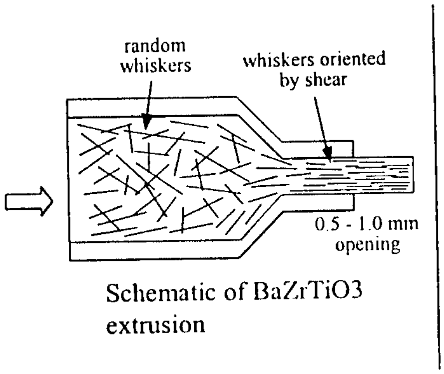

Figure 9. Proposed SSG of $Ba(Zr,Ti)O_3$ textured crystals using $BaTiO_3$ whiskers.

3. Crystallographic Engineering

The opportunity of high piezoelectric activity through crystallographic engineering is the basis of this program. Demonstrated in relaxor-PT systems, and summarized in Table I, crystallographic orientation and an engineered domain configuration result in extraordinarily high piezoelectric activity, in contrast to polycrystalline materials (see Figure 10).

Appendix D reviews this aspect for Relaxor-PTs and new non-PbO systems of $BaTiO_3$ and Zr-$BaTiO_3$ as discussed previous section.

A key aspect to crystallographic engineering is to result in a stable domain configuration leading to a macro-symmetry differing from the local symmetry. For domain engineered systems, i.e. <001> in orthorhombic (2mm) and rhombohedral (3M) symmetries, a macro-symmetry of 4 mm is obtained.

It is important to highlight the necessity of domain stability. As shown in Figure 11, strains as high as 1.0% can be obtained, but are the result of a-c domain reorientation and are not useful for practical applications. Piezoelectric strain E-field behavior for domain stabilized $BaTiO_3$ crystals and corresponding d_{33} values are given in Figure 12.

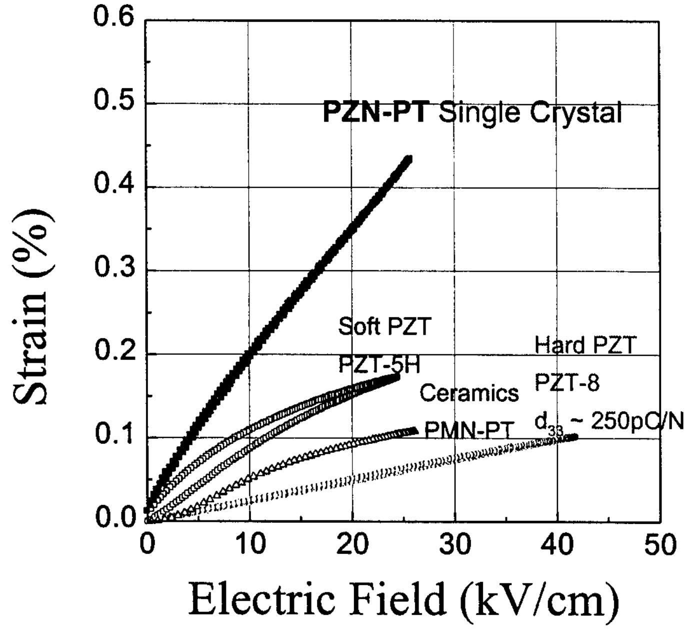

Figure 10. Strain vs. E-field for crystallinity engineered PZN-PT crystals versus polycrystalline piezoelectrics.

Table I.

	d_{33} (pC/N)	Maximum Strain	Hysteresis	Coercivity	Domain Configuration
"Soft" PZT's	>500	~ 0.2%	Large	Soft	unstable
"Hard" PZT's	200	~ 0.1%	Little	Hard	stable
Single Domain Crystals	<100	—	None	—	No wall
Domain Engineered Crystals (Relaxor-PT)	>2000	2%	Little/None	Soft	stable
Domain Engineered Crystal (non-PbO)	>600	—	Little	Soft	biased stabilized

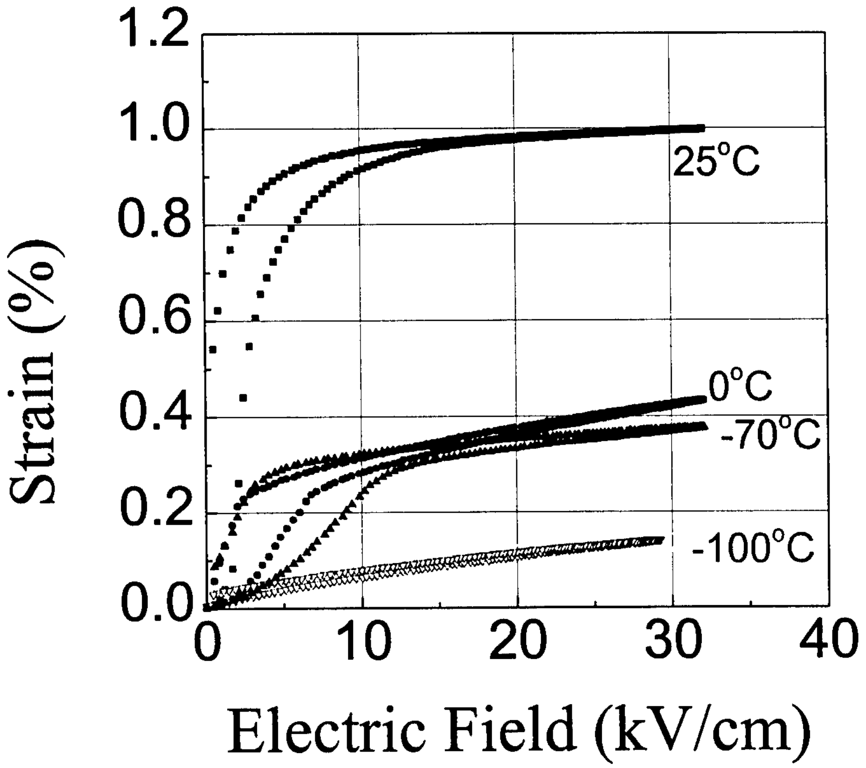

Figure 11. Crystallographic <001> engineering in $BaTiO_3$. Note the crystal structure determines the stability of engineered domain configuration. All regions exhibit 4 mm macro symmetry.

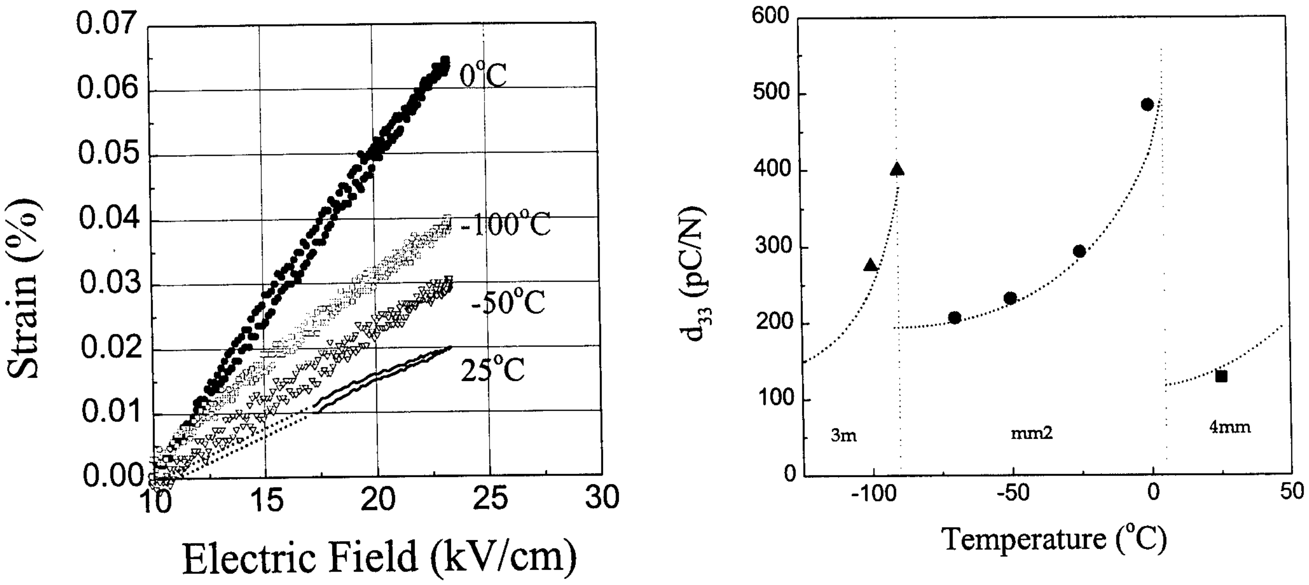

Figure 12. Piezoelectric strain E-field for a crystallographic engineered $BaTiO_3$ crystal. Note: A dc-bias was applied to achieve domain stability.

Future Work

Investigate the potential of crystallographic/domain engineering in alternative Relaxor-PT and non-PbO systems.

4. Domain Investigations

As pointed out in the previous section and Appendix D, crystallographic engineering and domain engineering are fundamentally tied together. Thus, understanding the domain configuration as related to thermal history, electric field and crystal orientation is important Using in-situ optical measurements, various orientation and stress effects on the domain structure morphology were investigated. As shown in Figure 13, dendritric domain structures were induced as defects where the local symmetry is broken from the macro symmetry, influencing the random nature of domain structure.

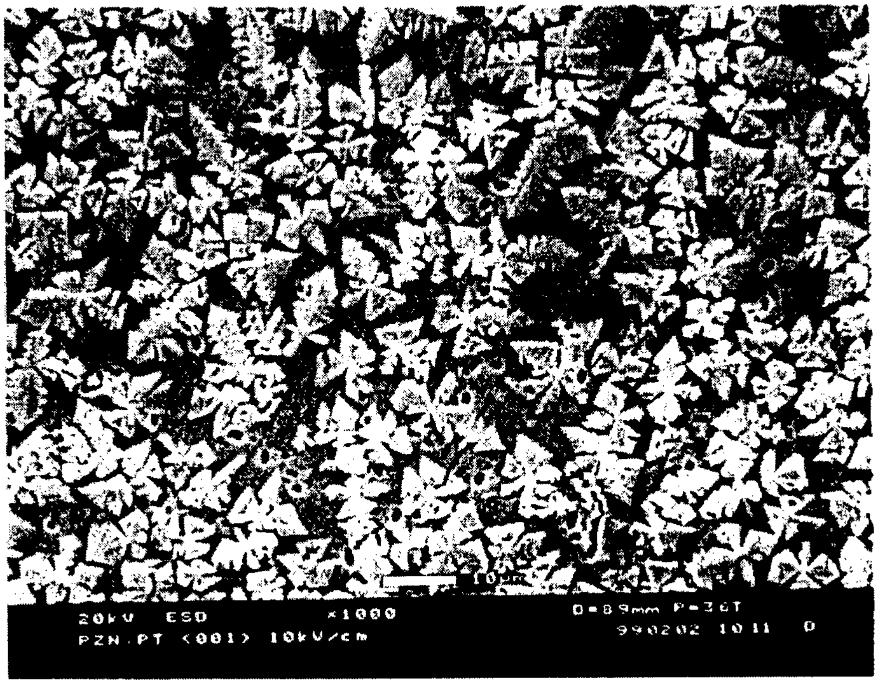

Figure 13. SEM etch structure of domains in PZN-PT as a function of crystallographic direction.

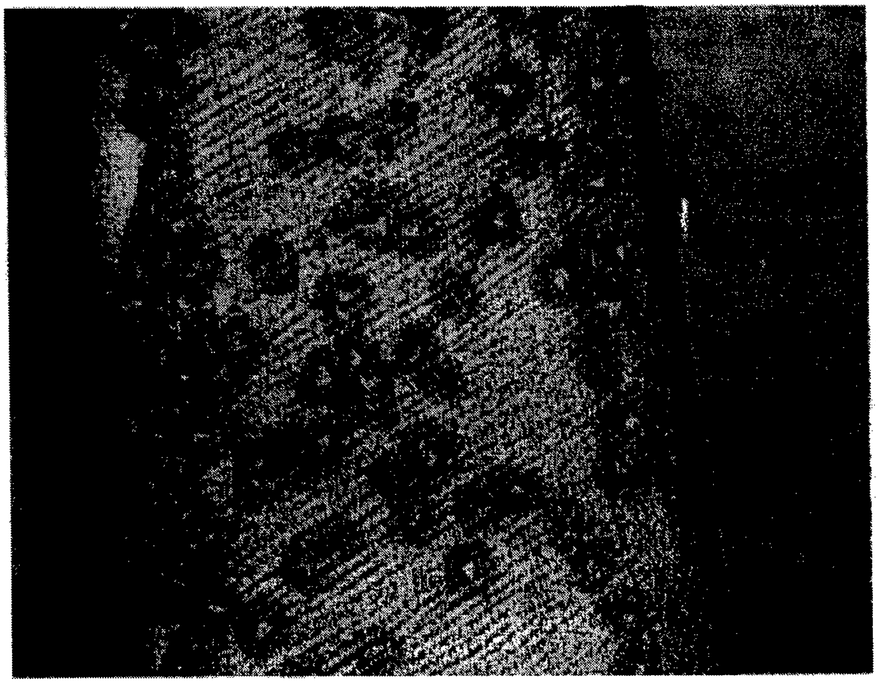

Figure 14. Optical photograph of domains in an E-field poled PZN-PT crystal.

Investigation of polarization fatigue (i.e. reduction of polarization reversed under a bipolar switching with E-fields > E_c is important in a practical application such as Non-Volatile Ferroelectric Memories (NVFM).

In regard to Relaxor-PT crystals, polarization fatigue was investigated as a function of crystallographic direction <111> vs. <001>. As shown in Figure 15, minimal fatigue was noted for <001> crystals to ~ 10^6 cycles, whereas dramatic fatigue was noted for <111> samples.

A qualitative model for observed fatigue behavior is presented in Figure 16, pointing out the importance of domains.

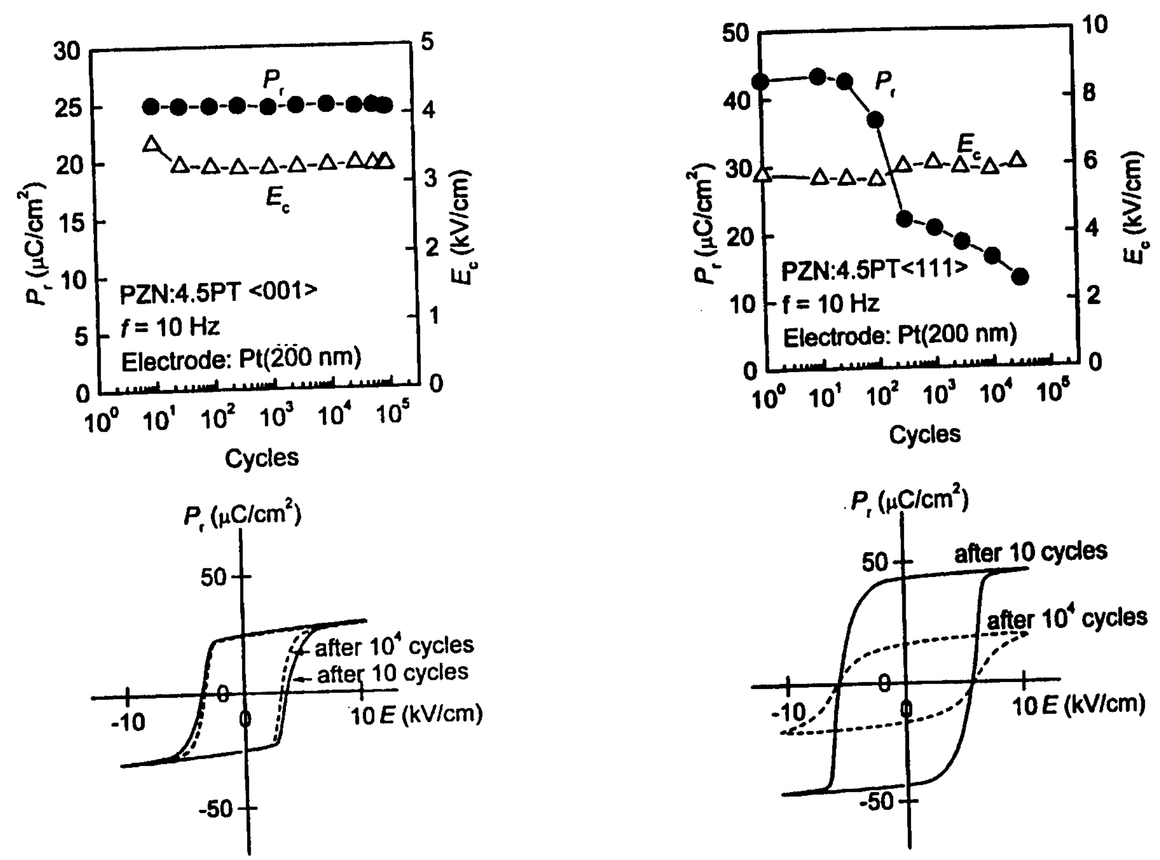

Figure 15. Crystallographic directional dependence of fatigue.

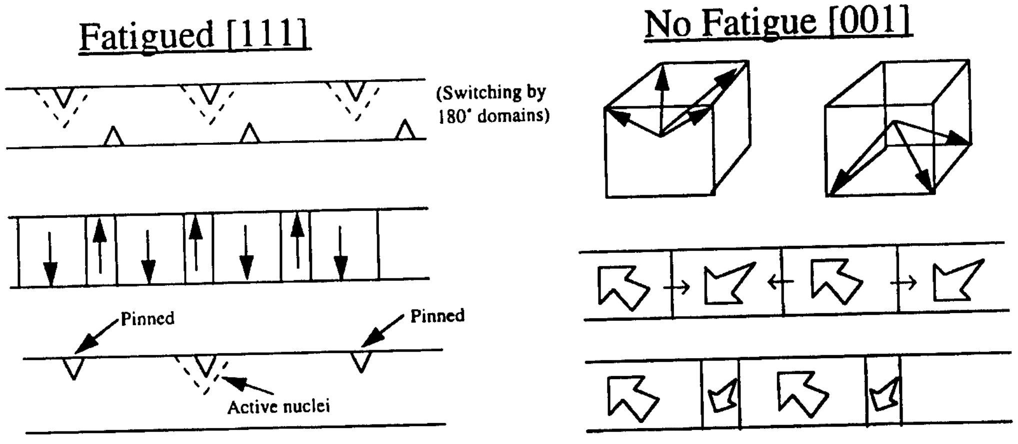

Figure 16. A qualitative fatigue model for single crystal PZN:PT.

Future Work

- Direct domain observation of dendritic structure in other families
- Investigate fatigue/orientation relationship in other systems

5. Thin Film Studies

The objective of thin film studies is to investigate the possibility of crystallographically enhanced properties in epitaxial and oriented relaxor ferroelectric thin films.

Using sol-gel processing (following the work of J.P. Maria, et al., J. Appl. Phys., Vol. 4, 1998), thin films of PMN-PT were fabricated. The dielectric and P/E behavior of <111> and <100> oriented films is shown in Figure 17. A comparison of PMN-PT films produced by both sol-gel processing and pulsed laser deposition are given in Table II. Though significantly reduced from that of bulk crystal PMN-PT piezoelectric d_{33} and d_{31} coefficients of 350 pC/N and −180pC/F, respectively, are 2–3 times that reported for PZT thin films.

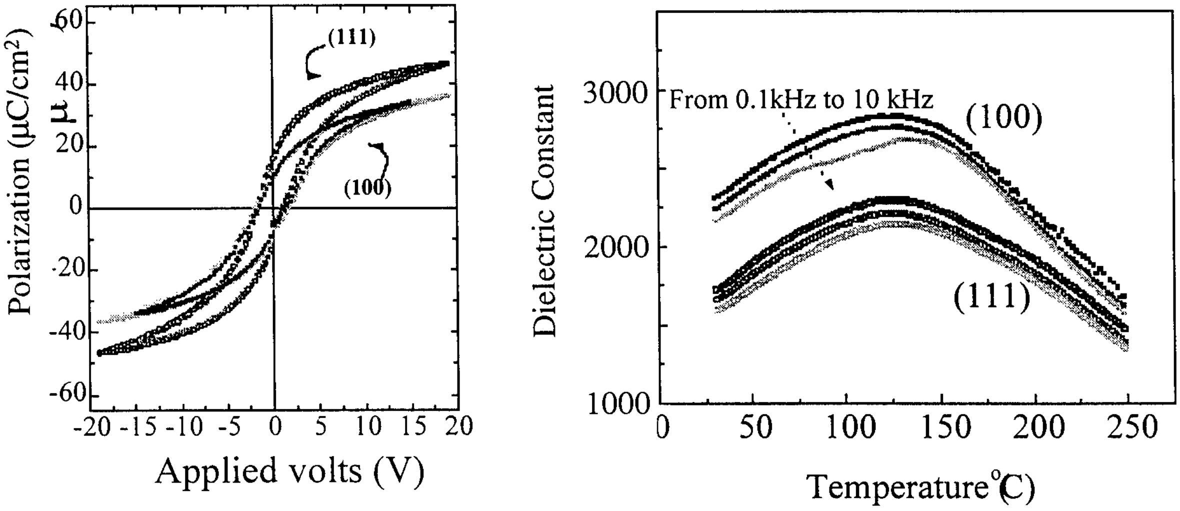

- (100)-preferred film (~1μm) ;

K = ~2200, tan δ < 0.03

P_r = ~10 μC/cm^2, $P_{sat.}$= 32 μC/cm^2

E_c = ~22 kV/cm

- (111)-preferred film (~1μm) ;

K = ~1700, tan δ < 0.03

P_r = ~12 μC/cm^2, $P_{sat.}$= 38 μC/cm^2

E_c = ~20 kV/cm

Figure 17. Dielectric Properties of Sol-Gel 67.5 $Pb(Mg_{1/3}Nb_{2/3})O_3$–32.5 $PbTiO_3$.

Table II. Comparison of Sol-Gel and Pulsed Laser Deposited PMN-PT Films

	Pulsed Laser Deposition	*Sol-Gel Processing*
Substrate	$SrRuO_3/LaAlO_3$	$Pt/Ti/SiO_2/Si$
Crystallinity	(001) epitaxial	(111) or (100) oriented
Area	~ 1cm x 1 cm	Up to 4" diameter
ε_r (25°C, 10 kHz)	~1100	~1500 – 2100
P_r (mC/cm2)	~18	~10

Novel Systems

To date, bulk crystal growth of the relaxor system $Pb(Yb_{1/2}Nb_{1/2})O_3$–$PbTiO_3$ has yet to be successful. The selection of this system was based on its relatively high T_c 350°C vs. 150–160°C for PZN-PT, and potential for higher coercivity. See Figure 18 for the phase diagram, and Table III compares polycrystalline results for various MPB piezoelectric compositions.

Oriented PYN-PT thin films were fabricated using pulsed laser deposition. As shown in Figure 19, large remanent polarization values were obtained, > 60 $\mu C/m^2$.

Future Work

- Determine the piezoelectric properties of PYbN-PT films
- Develop "compliant" substrates to minimize in-plane clamping

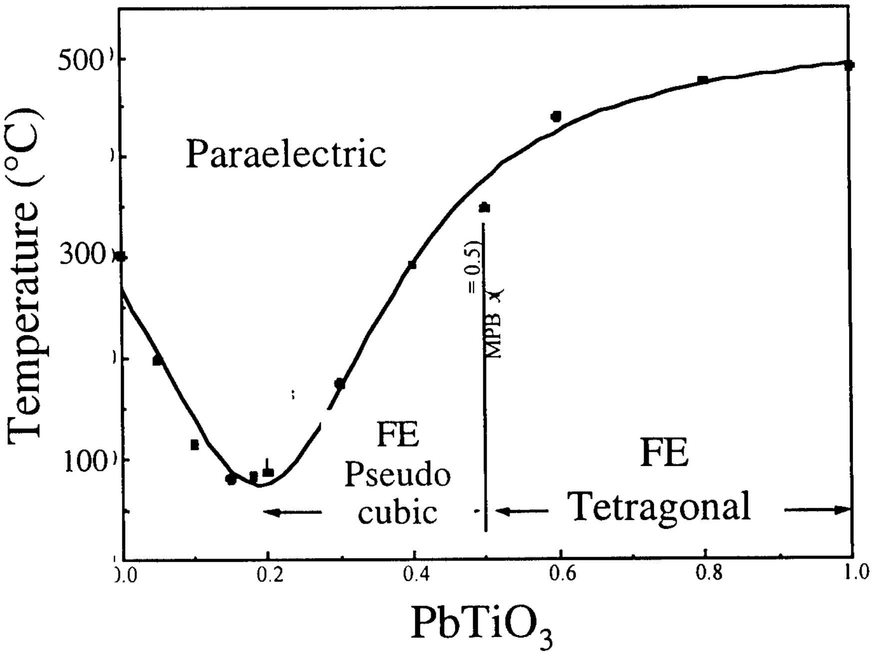

Figure 18. Phase diagram for PYbN-$PbTiO_3$. Note: FE=ferroelectric.

Table III: Properties of various polycrystalline piezoelectric systems.

		ε_r	d_{33}	k_p	k_t	T_c
PZT (53/47)	$Pb[Zr_{0.53}Ti_{0.47}]O_3$	~800	220	0.58		360
PMN-PT (70/30)	$Pb[Mg_{1/3}Nb_{1/3}]O_3$-$PbTiO_3$	5000	670	0.63		140
PSN-PT (58/42)	$Pb[Sc_{1/2}Nb_{1/2}]O_3$-$PbTiO_3$	2200	450	0.71	0.56	260
PST-PT (55/45)	$Pb[Sc_{1/2}Nb_{1/2}]O_3$-$PbTiO_3$	4000	655	0.61		205
PYbN-PT (50/50)	$Pb[Yb_{1/2}Nb_{1/2}]O_3$-$PbTiO_3$	1950		0.53	0.44	360

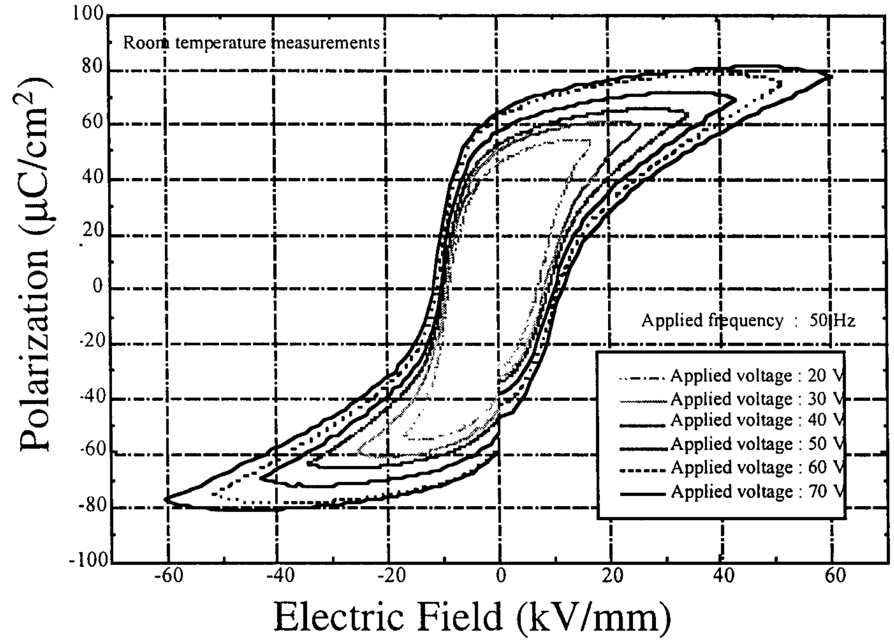

Fig. 19: Polarization – field behavior for a PYbN-PT film. Thickness – 1.2 μm, f(001) = 88%, ε_r = 1500, tan δ = 0.08

6. Optical Studies

The optical refractive indices as a function of frequency were determined for rhombohedral PZN-PT (4.5%PT) (see Figure 20) and tetragonal PZN-PT (12% PT). Table IV compares various refractive indices of selected perovskites and related materials

A key issue to determination of optical properties of the relaxor-PT crystals is optical transmittance. Owing to the domain engineered state in rhombohedral crystals and hence light scattering, tetragonal PZN-PT (12% PT) were selected. Both the electro-optic and acousto-optic effects for a 4mm tetragonal symmetry are presented in the following:

Figure 22 presents the r_{33} coefficient as a function of bias for PZN-PT (12% PT). Table V compares various electro-optic coefficients for PZN-PT, $LiNbO_3$ and SBN, showing a very high r_{51} coefficient for the relaxor-PT material. A schematic for measuring the EO effect is given in Figure 21.

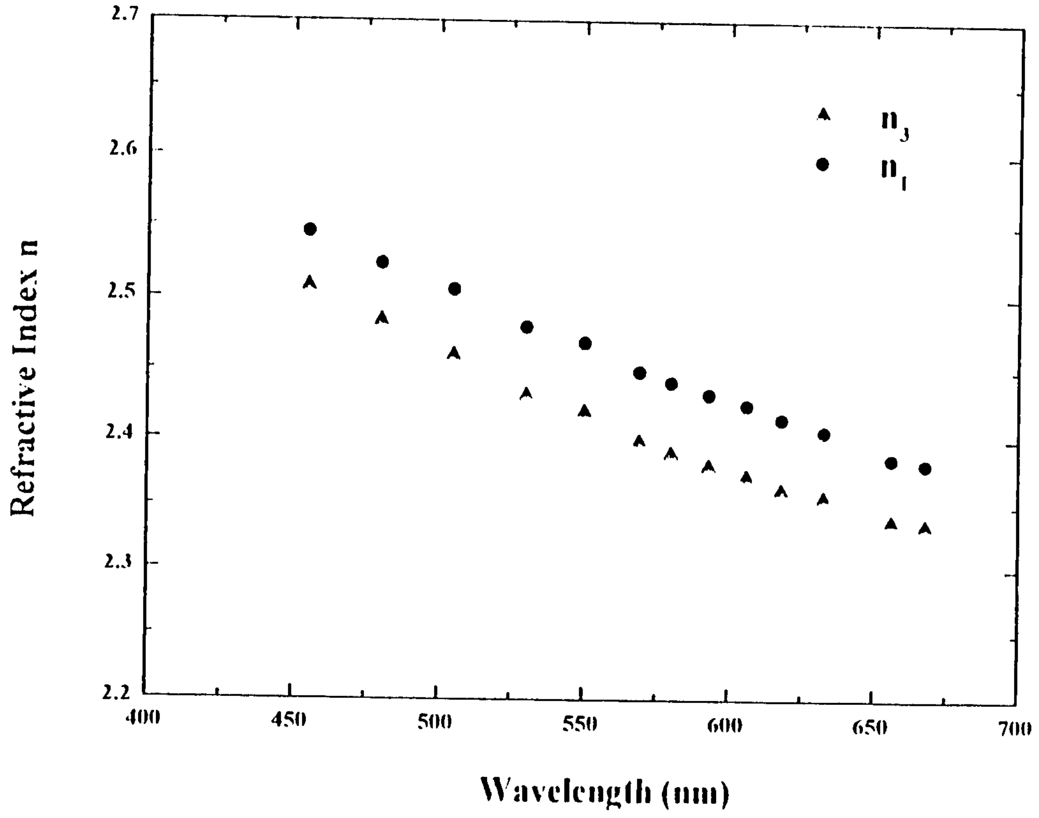

Figure 20. Refractive index as a function of wavelength for PZN-4.5%PT.

Table IV. Refractive indices for selected perovskites.

Materials	n_o	n_c	Wavelength	Notes
$BaTiO_3$	2.428	2.371	5893	Tetragonal
$PbTiO_3$	2.668	2.659	6328	Tetragonal
PMN	2.52		6328	Relax Cubic RT
PZN	2.45		5000	Trigonal (3m)
	2.41		7000	
PZN-4.5%PT	2.542		6328	Rhombohedral-pseudocubic T_c 150°C
PZN-12%PT	2.57		2.46	~Tetragonal
$Pb_2(Nb_{1.87}Mg_{0.13})O_7$	2.59		6328	Pyrochlore

ELECTRO-OPTIC EFFECT MEASUREMENT

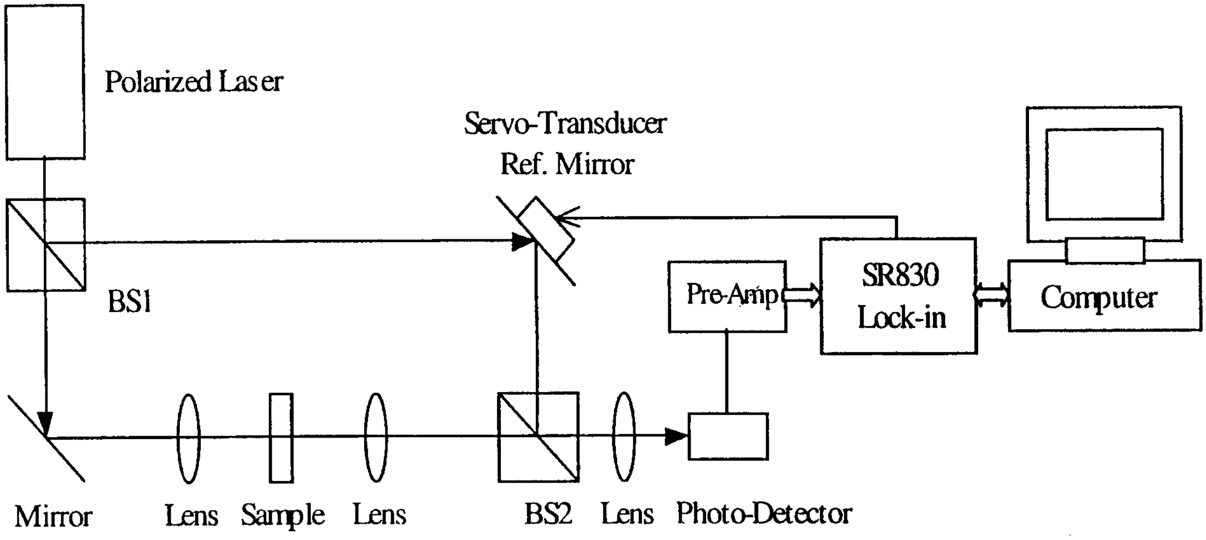

Figure 21. Schematic drawing of the setup for E-O measurements.

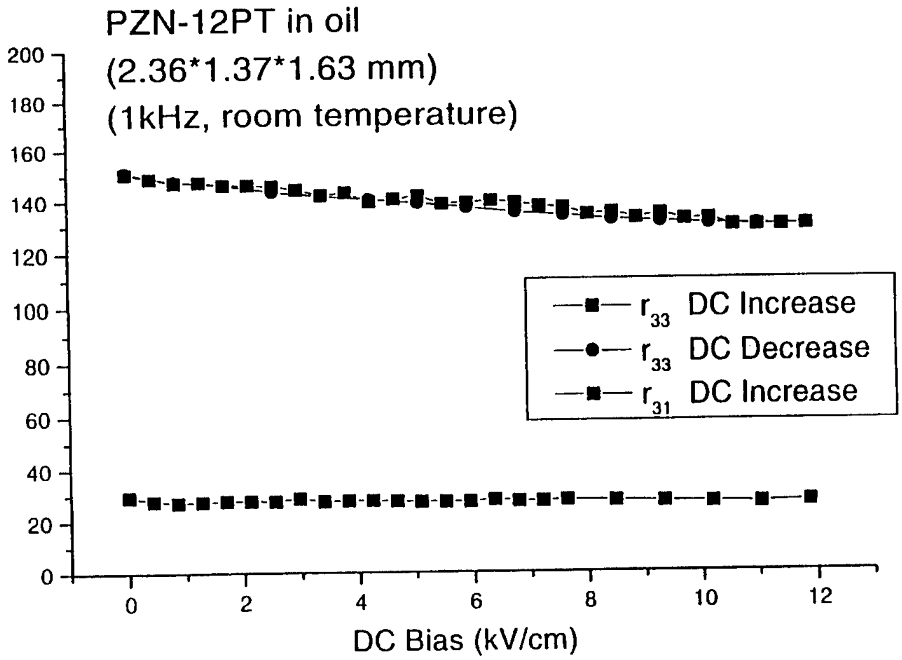
PZN-12PT in oil
(2.36*1.37*1.63 mm)
(1kHz, room temperature)
200
180
160
140
120
100
80
60
40
20
0
0
2
4
6
8
10
12
DC Bias (kV/cm)
—■— r_{33} DC Increase
—●— r_{33} DC Decrease
—■— r_{31} DC Increase

Figure 22.

Table V. Electro-Optic Coefficients

Material	Electro-optic Coefficient
0.88PZN-0.12PT	r_{33}=134 pm/V, r_{31}=7 pm/V, r_{51}=462 pm/V
$LiNbO_3$	r_{33}=30.8 pm/V, r_{31}=8.6 pm/V, r_{51}=28 pm/V
SBN (75/25)	r_{33}=1300 pm/V, r_{31}=66 pm/V, r_{51}=40 pm/V

It was anticipated that large acousto-optical coefficients could be achieved for crystals near the MPB. The hydrostatic acousto-optic coefficients for PZN-PT (12%PT) are presented in Table VI, and compared to other materials.

Using a figure of merit for acousto-optic scattering M:

$$M = \frac{p^2 n^6}{\rho \upsilon^3}$$

PZN-PT is about 40 times better than traditional materials.

Table VI. Acousto-optic Coefficient (P_r) under Hydrostatic Pressure

	Pr	M
PZN-PT (12%PT)	Pr=1.0	M=5.6×10^{-13} m^2/W
$LiNbO_3$	0.31	M=1.4×10^{-14} m^2/W
$LiTaO_3$	0.322	M=1.6×10^{-14} m^2/W
Flint Glass	0.25	M=1.67×10^{-14} m^2/W

Future Work

- Develop optic system for characterizing the acousto-optic coefficients under uniaxial stress.
- Characterize the A-O coefficients for PZN-PT near MPB.
- Carry out these measurements over an extended temperature range.
- Device development: optic hydrophone, stress sensor, scanner, and modulators.
- Characterize the E–O and A–O coefficients for PZN-PT thin films.
- Develop optic waveguide on the thin films for optic modulator and sensors.

7. Electromechanical Characterization

As a resource, the importance of generating a reliable method or methods of full characterization of single crystal piezoelectrics is essential. In addition to composition and phase, key issues include the domain engineered macro symmetry (4mm?) domain stability (fully polarized), sample geometry. In this work and described in Appendix , two approaches were used: (1) ultrasonic and (2) resonance techniques, as shown in Figure 23. Assuming a macrosymmetry of 4mm, the full elastic, dielectric, and piezoelectric matrices were determined for <001> PZN-4.5%PT and 8%PT. The orientations dependence of phase velocities were also determined as given in Figure 24, showing large anisotropy in k_{31} coupling.

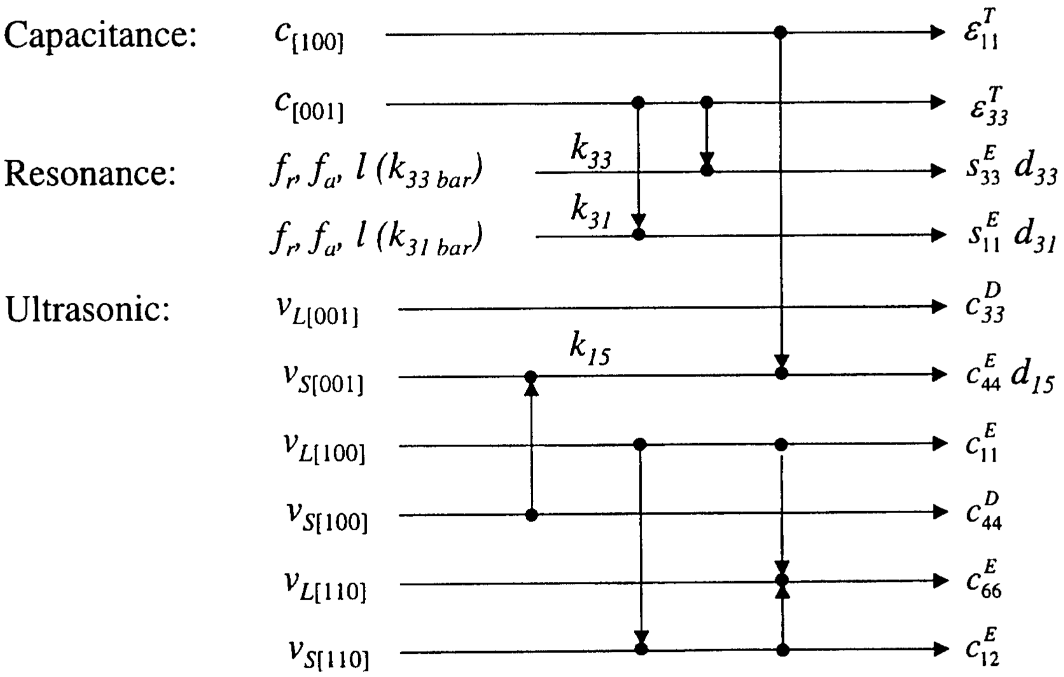

Figure 23. Combined characterization techniques for electromechanical characterization.

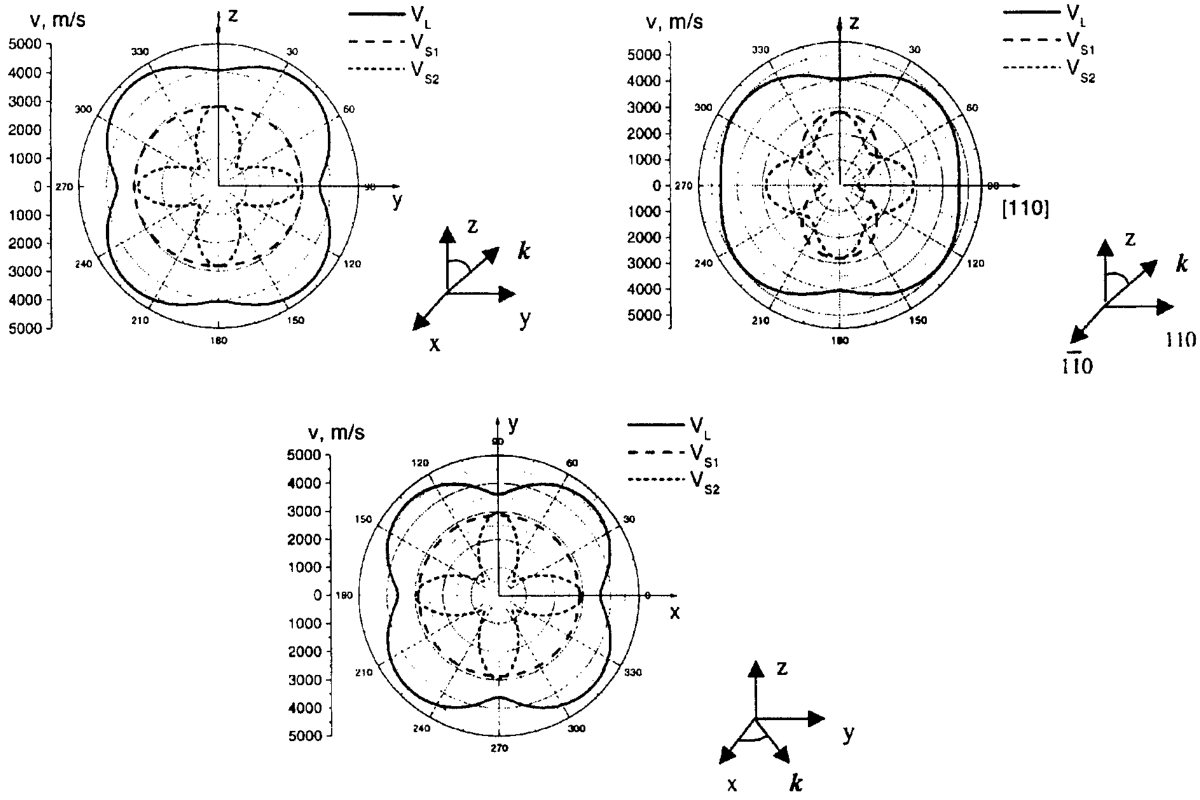

Figure 24. Orientational dependence of phase velocities.

Table VII. Measured Material Properties of PZN-4.5%PT Single Crystal.

Elastic Constants: c $(10^{10}C/m^2)$, s $(10^{-12}\ C/N)$

c^E_{11}	c^E_{12}	c^E_{13}	c^E_{33}	c^E_{44}	c^E_{66}
10.7	9.82	9.13	8.95	6.48	6.64

c^D_{11}	c^D_{12}	c^D_{13}	c^D_{33}	c^D_{44}	c^D_{66}
11.1	10.2	8.21	11.2	6.75	6.64

s^E_{11}	s^E_{12}	s^E_{13}	s^E_{33}	s^E_{44}	s^E_{66}
83.0	-30.6	-53.3	120.0	15.4	15.1

s^D_{11}	s^D_{12}	s^D_{13}	s^D_{33}	s^D_{44}	s^D_{66}
62.2	-51.4	-7.97	20.6	14.8	15.1

Electromechanical Coupling Constants:

k_{15}	k_{31}	k_{33}
0.20	0.50	0.91

Dielectric Constants: $\varepsilon\ (\varepsilon_0)$, $\beta\ (10^{-4}/\varepsilon_0)$

ε^S_{11}	ε^S_{33}	ε^T_{11}	ε^T_{33}
2975	869	3099	5242

β^S_{11}	β^S_{33}	β^T_{11}	β^T_{33}
3.36	11.5	3.23	1.91

Piezoelectric Constants: e (C/m^2), d $(10^{-12}C/N)$ g $(10^{-3}\ m^2/C)$ and h $(10^8 N/C)$

e_{15}	e_{31}	e_{33}	d_{15}	d_{31}	d_{33}
8.43	-5.34	13.1	130	-981	2140

g_{15}	g_{31}	g_{33}	h_{15}	h_{31}	h_{33}
4.74	-21.1	46.3	3.20	-6.94	17.1

Density: $\rho = 8310\ g/cm^3$

Table VIII. Measured Material Properties of PZN-8%PT Single Crystal.

Elastic Constants: c (10^{10}C/m^2), s (10^{-12} C/N)

c^E_{11}	c^E_{12}	c^E_{13}	c^E_{33}	c^E_{44}	c^E_{66}
11.1	10.2	9.97	10.2	6.1	6.56
c^D_{11}	c^D_{12}	c^D_{13}	c^D_{33}	c^D_{44}	c^D_{66}
12.6	11.7	7.93	13.0	6.45	6.56
s^E_{11}	s^E_{12}	s^E_{13}	s^E_{33}	s^E_{44}	s^E_{66}
82.0	-29.1	-51.5	110	16.41	5.2
s^D_{11}	s^D_{12}	s^D_{13}	s^D_{33}	s^D_{44}	s^D_{66}
59.0	-52.1	-4.17	12.8	15.5	15.2

Electromechanical Coupling Constants:

k_{15}	k_{31}	k_{33}
0.23	0.53	0.94

Dielectric Constants: ε (ε_0), β ($10^{-4}/\varepsilon_0$)

ε^S_{11}	ε^S_{33}	ε^T_{11}	ε^T_{33}
2848	579	3012	5689
β^S_{11}	β^S_{33}	β^T_{11}	β^T_{33}
3.51	17.3	3.32	1.76

Piezoelectric Constants: e (C/m^2), d (10^{-12}C/N) g (10^{-3} m^2/C) and h (10^8N/C)

e_{15}	e_{31}	e_{33}	d_{15}	d_{31}	d_{33}
9.39	-8.84	11.8	154	-1080	2231
g_{15}	g_{31}	g_{33}	h_{15}	h_{31}	h_{33}
5.78	-21.4	43.9	3.73	-17.2	23.1

Density: $\rho = 8315$ g/cm^3

Future Work

- Refine the measurements on material properties in the PMN-PT systems and try to figure out the source for the inconsistencies.
- Modify the ultrasonic systems so that bias can be applied to the systems which will allow the measurement of single domain data.
- Try to see if the discrepancies were from nonlinear effects, since the domain process is intrinsically lossy and nonlinear.
- Try to correlate the domain pattern to the measured material properties. Build up a data base for future theoretical analysis.
- Further theoretical development to address the symmetry and effective material property problems.

8. Honors and Awards

A.S. Bhalla

Elected Trustee of Electronics Division, ACerS, 1999
Editor, "Ferroelectrics Review"

R. Guo

Elected Secretary of Electronic Division, AceS, 1999–2000

S.E. Park

1998 Faculty Achievement Award (MRL/PSU)

C.A. Randall

Wilson Teaching Award, The Pennsylvania State University, 1998

T.R. Shrout

1998 Faculty Achievement Award (MRL/PSU)
Chairman, 9th US-Japan Seminar on Dielectric and Piezoelectric Ceramics, Okinawa, Japan, 1999

Q. Zhang

Outstanding Research Award, College of Engineering, Penn State University, 1999

9. Papers Published in Refereed Journals

1. S.E. Park and T.R. Shrout, "Electric Field Anisotropy in Electrostrictive $Pb(Mg_{1/3}Nb_{2/3})O_3$–$PbTiO_3$ Crystals," Ferroelectrics 207, 519–576 (1998).

2. T. Li, A.M. Scotch, H.M. Chan, M.P. Harmer, S.E. Park, and T.R. Shrout, "Single Crystals of PMN-35 mol%PT from Polycrystalline Precursors," J. Amer. Cer. Soc., 8[1],224–248 (1998).

3. D.-S. Paik, S.–E. Park, S. Wada, S.–F. Liu, and T.R. Shrout, "E-field Induced Phase Transition of <001> Oriented Rhombohedral $0.92Pb(Zn_{1/3}Nb_{2/3})O_3$ Crystals," Journal of Applied Physics, 85[2], 1080–1083 (1999).

4. S.–F. Liu, S.–E. Park, T.R. Shrout, and L.E. Cross, "E-field Dependence of Piezoelectric Properties for Rhombohedral $0.955Pb(Zn_{1/3}Nb_{2/3})O_3$–$0.045PbTiO_3$ Single Crystals," Journal of Applied Physics, 85[5], 2810–2814 (1999).

5. D.–S. Paik, S.–E. Park, T.R. Shrout, and W. Hackenberger, "Dielectric and Piezoelectric Properties of Perovskite Materials at Cryogenic Temperature," J. Mat. Sci. 34, 469–473 (1999).

10. Papers Published in Non-Refereed Journals

1. T.A. Ritter, K.K. Shung, S.–E. Park, X. Geng, and T.R. Shrout, "1–3 Single Crystal Composites for Ultrasonic Transducer Arrays," Proceedings of SPIE Medical Imaging 1998: Ultrasonic Transducer Engineering, Vol. 3341, pp. 249–263, SPIE Press, 1998.

2. P.D. Lopath, S.–E. Park, K.K. Shung, and T.R. Shrout, "Single Crystal PZN/PT Transducers," Proceedings of SPIE Medical Imaging 1998: Ultrasonic Transducer Engineering, Vol. 3341, pp. 242–249, SPIE Press, 1998.

11. Papers Submitted for Publication

1. Yonghong Bing, Ruyan Guo, and Amar Bhalla, "Optical properties of relaxor perovskite oxides as function of temperature and various polarization conditions," (to be published in Ceramic Transactions, 1999).

2. J. Cui, Ruyan Guo, and A.S. Bhalla, "Growth and ferroelectric property studies of lead containing relaxor ferroelectric crystals by LHPG method," (to be published in Ceramic Transactions, 1999).

3. Ruyan Guo, Yu Zhi, Jenny Cui, and Amar Bhalla, "Growth and properties of PMN-PT single crystals grown by the LHPG technique," (to be published in Materials Letters, 1999).

4. W. Cao, S. Tavener, and S. Xie, "Simulation of Finite Size Effects and Boundary Condition Influence in Ferroelectric Systems," Journal of Applied Physics, submitted (1999).

5. Jon-Paul Maria, J.F. Shepard, Jr., S. Trolier-McKinstry, T.R. Watkins, and A.E. Payzant, "Piezoelectric analysis of $Pb(Mg_{1/3}Nb_{2/3})O_3$–$PbTiO_3$ epitaxial thin films," submitted to Journal of Applied Physics.

6. J. Erhard and W. Cao, "Effective Material Properties in Twinned Ferroelectric Crystals," J. Applied Physics, accepted (1999).

7. J.H. Yin, B. Jiang, and W. Cao, "Elastic, Piezoelectric, and Dielectric Properties of PZN-PT Single Crystals," Proc. SPIE Imaging 99, in print (1999).

12. Patents and Submitted Patents

1. S.–E. Park and T.R. Shrout, "High Strain Actuator Using Ferroelectric Single Crystal," US Patent No. 5,804,907 (1998).

2. P.W. Rehrig, S.–E. Park, Satoshi Wada, T.R. Shrout, G.L. Messing. PSU Invention Disclosure.

13. Books (and Sections Thereof)

1. Amar Bhalla and Ruyan Guo, Pyroelectricity, Encyclopedia of Electrical and Electronics Engineering, editor, J.G. Webster, John Wiley & Sons, Inc. (1999).

2. Chapter 3 in Adaptronics and Smart Structures—basics, materials, design, and applications," ed. H. Janocha, Springer Verlag, Berlin (1999).

14. Invited Presentations

1. Amar Bhalla, "Relaxor Ferroelectrics," Electronics Materials Symposium, 1998, Baton Rouge, LA.

2. A.S. Bhalla, "Properties of Nanoregions and Boundaries in Ferroelectrics," presented at the Third Pacific Rim International Conference on Advanced Materials and Processing, Honolulu, Hawaii, July 1998.

3. D.M. Hatch and W. Cao, "Determination of Domain and Domain Wall Formation at Ferroic Transition," The 5th International

4. W. Cao, "Materials Born to be Smart and Made to be Smart," Plenary Lecture at the 4th Annual German-American Frontiers of Science Symposium, Irvine, CA, June 4–6, 1998.

5. W. Cao, "Physical principles of domain engineering in PZN-PT single crystal systems," Medical Imaging 1999, San Diego, CA, Feb. 20–26, 1999.

6. W. Cao, "Ferroelectric Materials and Their Applications," Los Alamos National Lab., New Mexico, June 12, 1998.

7. W. Cao, "Landau-Ginzburg Theory for Inhomogeneous Structures Resulting a Ferroelectric Phase Transition," Department of Physics, Nanjing University, Nanjing, Oct. 12, 1998.

8. W. Cao, "Observation of Ferroelectric Domains and Computer Simulations," Laboratory of Solid State Microstructures, Nanjing University, Nanjing, China, Oct. 13, 1998.

9. S.–E. Park, "Relaxor based single crystals for high performance piezoelectrics," Lucent Technology, Murray Hill, NJ, January 1999.

10. S.–E. Park and T.R. Shrout, "Crystallographic Engineering in High-Performance Piezoelectric Crystals," SPIE's 6th Annual International Symposium on Smart Structures and Materials, Invited Paper, Newport Beach, CA, March 1999.

11. T.R. Shrout, S.–E. Park, P.D. Lopath, R. Meyer, Jr., K.K. Shung, T.A. Ritter, J. Van Tassel, and C.A. Randall, "Innovations in Piezoelectric Materials and Processing for Ultrasonic Transducers," SPIE's International Symposium on Medical Imaging, Invited paper, San Diego, CA, February 1999.

12. T.R. Shrout, "Relaxor Based Single Crystals for High Performance Piezoelectrics," ISAF, Switzerland (1998).

13. P.D. Lopath, R. Meyer, S.–E. Park, T.R. Shrout, and X. Geng, "1–3 Single-Crystal Composites for Ultrasonic Transducer Arrays," SPIE's International Symposium on Medical Imaging, San Diego, CA, February 1999.

14. T.A. Ritter, K.K. Shung, S.–E. Park, T.R. Shrout, and X. Geng, "1–3 Single-Crystal Composites for Ultrasonic Transducer Arrays," SPIE's International Symposium on Medical Imaging, San Diego, CA, February 1999.

15. S. Trolier-McKinstry, J.–P. Maria, R. Polcawich, J.F. Shepard, Jr., W. Ren, and F. Xu, "Ferroelectric Films for MEMS Applications," International Conference on Metallurgical Coatings and Thin Films, San Diego, CA April 1999.

16. S. Trolier-McKinstry, J.–P. Maria, and J.H. Park, "Epitaxial and Oriented $Pb(Mg_{1/3}Nb_{2/3})O_3$–$PbTiO_3$ Films," Materials Research Society Meeting, San Francisco, CA, April 5–9, 1999.

17. S. Trolier-McKinstry and J.–P. Maria, "Structure-Property Relations in Epitaxial $Pb(Mg_{1/3}Nb_{2/3})O_3$-$PbTiO_3$/$SrRuO_3$/$LaAlO_3$ Heterostructures," Pittsburgh Diffraction Conference, Pittsburgh, PA, Nov. 5–7, 1998.

Contributed Papers

1. Farrah C. Gaskins (mentor: R. Guo), "Thermal Expansion Study of Ferroelectric Relaxor Materials," The Pennsylvania State University Summer Research Opportunities Program Symposium, Aug. 1998, University Park, PA.

2. Yonghong Bing, Ruyan Guo, and A.S.Bhalla, "Optical properties of relaxor perovskite oxides as function of temperature and various polarization conditions," AcerS 1999 Annual Meeting, Apr. 25–28, 1999, Indianapolis, IN.

3. J. Cui, Ruyan Guo, and A.S. Bhalla, "Growth and ferroelectric property studies of lead containing relaxor ferroelectric crystals by LHPG method," AcerS 1999 Annual Meeting, Apr. 25–28, 1999, Indianapolis, IN.

4. Farrah C. Gaskins and Ruyan Guo, "Thermal Expansion Study of Ferroelectric Relaxor Materials," ONR 1999 Transducer Materials and Transducers Workshop, Apr. 13–15, 1999, University Park, PA.

5. Ruyan Guo, Howard Evans, and Amar Bhalla, "Crystal Structure Analysis and Identification of Polarization Mechanisms in Relaxor Ferroelectric Tungsten Bronze Materials," ONR 1999 Transducer Materials and Transducers Workshop, Apr. 13–15, 1999, University Park, PA.

6. Jiri Erhart, W. Cao, and J. Fousek, "A study of S-Walls in a m3m-mmm Ferroelastic Phase Transitions," The XI International Symposium on Application of Ferroelectrics, Montreux, Switzerland, Aug. 24–27, 1998.

7. J.H. Yin, B. Jiang, and W. Cao, "Elastic, piezoelectric and dielectric properties of PZN-PT single crystals," Medical Imaging 1999, San Diego, CA, Feb. 20–26, 1999.

8. W. Cao, A. Saxena, D. Hatch, and G. Barsch, "Theory of Domain Walls in Improper Ferroelastic Phase Transition Driven by Zone Boundary Phonon," APS March Meeting, Atlanta, GA, March 1999.

9. H. Yu and C.A. Randall, "The Studies of Dendritic Structures in PZN:PT Single Crystal Materials," 101st American Ceram. Soc.

10. D. Paik, S.–E. Park, and W. Hackenberger, "Cryogenic Behavior of Perovskite Materials," American Ceramic Society Meeting, Cincinnati, OH, May 1998.

11. T.R. Watkins, E.A. Payzant, J.–P. Maria, S. Trolier-McKinstry, S.T. Misture, and S.M. Pilgrim, "Electroactive Characterization of PMN by X-Ray Diffraction," poster presentation at Pittsburgh Diffraction Conference, Pittsburgh, Nov. 1998.

12. J.–P. Maria, E.A. Payzant, J.F. Shepard, Jr., and S. Trolier-McKinstry, "Epitaxial $Pb(Mg_{1/3}Nb_{2/3})O_3–PbTiO_3$ Thin Films," oral presentation: International Symposium on Applications of Ferroelectrics, Montreux, Switzerland, Aug. 25–27, 1998.

13. S. Trolier-McKinstry, F. Xu, J.–P. Maria, R. Polcawich, and J.F. Shepard,Jr., "Piezoelectric Thin Films for MEMS Applications, " oral presentation at the International Symposium on Integrated Ferroelectrics, Colorado Springs, CO, March 7–10, 1999.

APPENDIX A

TEMPLATED GRAIN GROWTH OF BARIUM TITANATE SINGLE CRYSTALS

Paul W. Rehrig,* Gary L. Messing,* and Susan Trolier-McKinstry*

Materials Research Laboratory, The Pennsylvania State University, University Park, Pennsylvania 16802

Single crystals of $BaTiO_3$ were grown by templated grain growth (TGG). TGG involves contacting a single crystal "template" to a sintered polycrystalline matrix and then heating the assemblage to a temperature that promotes the migration of the single crystal boundary through the matrix. In this investigation mm-sized single crystals of $BaTiO_3$ were produced by heating a 97% dense polycrystalline matrix with a Ba/Ti ratio < 1.00 at temperatures above the eutectic temperature. The initial matrix composition was controlled by leaching different amounts of Ba from the matrix powder. Initial crystal growth rates of were measured as a function of template orientation and matrix composition. Growth rates ranged from ~590-790 µm/h, ~180-350 µm/h, and ~42-59 ~m/h for {111}, {100}, and {110} oriented single crystal templates, respectively. The lower and higher limits to these ranges correspond to a matrix composition of 4.4 and 2.7 mol% excess Ti, respectively. Following formation of crystal facets for the {111} and {100} templates, the growth rates then slowed appreciably. Exaggerated matrix grains were shown to influence the crystal growth rates at times greater than 10 hours at 1350°C.

Based in part on the thesis submitted by Paul W. Rehrig for the Ph.D. degree in Materials Science and Engineering, Pennsylvania State University, University Park, PA 1998.

Supported by the Defense Advanced Research Projects Agency, under AFOSR Grant # F49620-94-1-0428

* Membership in the American Ceramic Society

I. Introduction

Some single crystal systems cannot be produced easily by melt techniques due to either incongruent melting or phase transitions. Currently most large single crystals of $BaTiO_3$ are synthesized by top-seeded solution growth (TSSG)$^{1-3}$ from a TiO_2-rich melt because the hexagonal-to-cubic phase transition at 1430°C causes fracture on cooling.^{4} Generally such techniques are both time consuming and costly. Therefore, it is important to develop alternate routes for producing single crystals.

One method for growing single crystal barium titanate, known as twin-plane reentrant edge (TPRE) growth, has been described recently by Yoo *et al.*.^{5} They reported that a small amount of SiO_2 placed on top of a $BaTiO_3$ green compact nucleated a few seed grains with twin lamella, i.e. {111} growth twins, during subsequent sintering. By controlling the number of twins and taking advantage of the TPRE growth mechanism they were able to grow cm-sized crystals at rates of approximately 200 μm/h. The crystals produced from this method contained growth twins and a few volume percent trapped porosity.

Another approach for growing single crystals of barium titanate (as well as a number of other systems) is templated grain growth (TGG). TGG involves bringing a seed crystal and a sintered polycrystalline matrix into contact and then heating to produce a single crystal by sustained directional growth of the interface into the polycrystalline matrix. The driving force for boundary migration is the grain boundary free energy, which increases with decreasing grain size. Therefore, the grain size of the matrix is a critical parameter for successful crystal growth by this approach.

It is well known that a small amount of excess TiO_2 reacts with $BaTiO_3$ to form $Ba_6Ti_{17}O_{40}$ at high temperatures and at 1332°C $Ba_6Ti_{17}O_{40}$ reacts with $BaTiO_3$ to form a eutectic melt.^{4,6} When uncontrolled, this liquid phase can lead to exaggerated grain growth. Very small amounts of liquid can greatly influence grain growth behavior; exaggerated grain growth is believed to be caused by the heterogeneous distribution of a limited amount of liquid phase as well as the presence of grains much larger than the average population size.[7] To reduce the nucleation of exaggerated grains in the matrix during templated grain growth, the liquid should be uniformly distributed. Careful control of stoichiometry during processing of barium titanate is a very important issue.[7-10] It is difficult to sinter barium titanate and thus, a small amount of liquid phase is often intentionally introduced to enhance densification. It is the careful balance and control of the liquid phase that determines the resulting microstructure. Although exaggerated grain growth in barium titanate has been studied extensively, most research has focused on inhibiting exaggerated grain growth. Only recently has this material characteristic been used in a more positive way to enhance the growth of single crystals via a polycrystalline to single crystal conversion process.

The challenge in using exaggerated grain growth in a way that enhances the growth of a few grains (or a single grain) while limiting the growth of others is that conditions must be maintained so that the growth of a large grain is favored, while the conditions are such that growth of matrix grains is suppressed. In the barium titanate matrix, grain growth inhibition has been successfully achieved mostly by doping. Although the effect of doping on matrix grain growth is well understood, there are few models that describe exaggerated grain growth in barium titanate.

The goal of this study was to determine what factors could be controlled to accelerate the growth of crystals by TGG. In contrast to the approach of Yamamoto and Sakuma, Ti-rich $BaTiO_3$ was used to create a liquid at the growth temperatures and thus accelerate diffusion. To gain a more fundamental understanding of the rate-controlling processes, the kinetics and thermodynamics of TGG were evaluated as a function of template orientation. It was found that appreciable growth could be achieved without using either pressure or a solution precursor to bond the seed to the matrix.

II. Background

The TGG process has been investigated for growing single crystals in many different systems. Early work on TGG includes a 1982 patent for producing single crystal ferrites.

Matsuzawa *et al.*[11] brought a fine-grained, dense polycrystalline matrix into contact with a single crystal of similar composition, $(Mn_xZn_{1-x})Fe_2O_4$, at 1350°C for 3 hours. They were able to produce 5 - 10 mm thick crystals. They did not report the kinetics or thermodynamics of the system, though they did identify some of the critical experimental parameters for successful boundary migration of the single crystal into the matrix, including purity, a fine-grained matrix, uniform contact between the matrix and seed crystal, and a low enough temperature to avoid exaggerated grain growth. Due to the occurrence of exaggerated grain growth in titanium-rich $BaTiO_3$, similar parameters also apply to the barium titanate system. Matsuzawa *et al.*[11] also used a solution-derived precursor at the interface to enhance boundary migration; however the mechanisms of the enhancement were not reported. Imaeda and Matsuzawa[12] used a very similar technique to produce 5 - 10 mm single crystals of yttrium iron garnet at 1500°C under 1500 atm of pressure. In their process, a solution precursor was not used at the interface, but they did find that hot isostatic pressing enabled them to achieve optical quality single crystals. More recently, TGG has been applied to the $Pb(Mg_{1/3}Nb_{2/3})O_3$ - 35 mol% $PbTiO_3$ system.[13] In this work, a single crystal seed was embedded within an unfired polycrystalline powder compact and the compact was then heated to temperatures between 900°C and 1200°C. The polycrystalline matrix was significantly PbO excess and therefore there was a liquid phase present during the growth. Growth from the initial ~ 1 mm seed was on the order of 1-2 mm after 140 h at 1150°C.

As mentioned above, TGG can also be applied to the barium titanate system. DeVries was the first to take advantage of exaggerated grain growth in $BaTiO_3$ to grow single crystals of $BaTiO_3$.[14] He employed a steep temperature gradient or the addition of seed crystals to achieve the growth of larger single crystals than those achieved by exaggerated grain growth alone. Yamamoto and Sakuma[15,16] achieved millimeter growth of $BaTiO_3$ by a TGG process. They bonded a $BaTiO_3$ crystal to a polycrystalline matrix at 1200°C for 2 hours at either 15 MPa[15] or 1.5 MPa[16] and then heated the assembly at 1300°C for 30 hours to obtain 3 × 3 × 0.4 - 0.5 mm crystals. They reported that the single crystals included porosity from the polycrystalline matrix, which was 98.6 percent of theoretical density. They limited crystal growth to temperatures below the eutectic temperature to limit exaggerated grain growth in the polycrystalline matrix. The growth of the single crystal was hindered because of the porosity and the exaggerated matrix grains (~100 μm), which resulted in an average growth rate after 20 h of 50 μm/h. From SEM micrographs of sample cross sections, Yamamoto and Sakuma[16] observed that the growth front of the single crystal had a pyramid shape with a (001) basal plane and four {012} habit planes.

Hennings *et. al.*[8] described exaggerated grain growth in $BaTiO_3$ as a solution-segregation process. He used the addition of "seed grains," large grains from a previously sintered polycrystalline matrix, to control the exaggerated grain growth in a Ti-rich $BaTiO_3$ powder. It was reported that a $BaTiO_3$ compact with 2 to 3 mol% excess TiO_2 (without seed grains) had an average grain size of only 1 to 2 μm when sintered at 1300°C for over 60 h. All of the grains observed in microstructures of compacts sintered at temperatures below the eutectic contained growth twins. However, at temperatures above the eutectic, 1332°C, compacts containing excess TiO_2 were mostly consumed by exaggerated grains in less than 1 hour. Hennings *et al.*[8] also found that the number of exaggerated grains increased exponentially with time, but the growth rates were linear with time.

Most of the experiments conducted by Hennings *et al.*[8] were for times less than 15 minutes, but average growth rates of exaggerated grains can be extracted from some of the plots for samples containing 2 and 4 mol% excess TiO_2 sintered at 1330°C. From the behavior of their system they presumed that the heat treatment was conducted above the eutectic temperature. For the 2 mol% TiO_2 excess sample a growth rate of 155 μm/h was calculated for a grain of 5 μm at time ~ 0 h. On the other hand, the 4 mol% TiO_2 excess sample exhibits a growth rate of 90 μm/h with a initial grain size of 7 μm at time ~ 0 h. Hennings[8] attributes the drop in growth rate to an increase in liquid phase volume associated with an increase in TiO_2 excess. This results in a thicker liquid phase layer and a shallower concentration gradient between small and large grains.

Kolar[7] studied the effects of excess TiO_2 on the microstructural evolution of $BaTiO_3$. Electronic grade $BaTiO_3$ powder with a titanium/barium ratio of ~1 was mixed with $Ba_6Ti_{17}O_{40}$ to achieve a 2 mol% Ti-excess powder. The powder was sintered to ~92-95% of theoretical density at 1300°C for 1 h. The resulting grain size was approximately 1 µm. Upon heating the samples to 1350°C, i.e., above the eutectic temperature, exaggerated grains grew in the matrix. Kolar reported an average nucleation rate for exaggerated grains of 120 $mm^{-2}min^{-1}$ at 1350°C; within 1 h the microstructure was mostly consumed by exaggerated grains with an average size of ~ 25-30 µm. It was also reported that the growth rate of the exaggerated grains was approximately 360 µm/h during the first 10 min, but slowed to rates orders of magnitude lower.

Yamamoto and Sakuma[15] were the first to report rate data for $BaTiO_3$ single crystals grown specifically by TGG. In their system it was found that the single crystal/polycrystalline matrix boundary grew the largest distance at temperatures below the eutectic temperature because exaggerated grain growth in the matrix was avoided. For temperatures exceeding the eutectic temperature, migration of the interface quickly slowed due to impingement with large grains. At 1350°C the boundary migrated approximately 300 µm within 1 h (300 µm/h), but did not migrate an appreciable amount after that. The grain size was ~200 µm after 10 h at 1350°C (initial grain size 1.7 µm). At 1300°C, at temperatures where exaggerated grain growth was suppressed, the boundary migrated approximately 750 µm within 5 h (150 µm/h), and the crystal grew greater than 1 mm in size with times up to 20 h. Yamamoto and Sakuma report that growth obeyed parabolic growth kinetics up to 5 h with a growth constant of 2.8×10^{-11} m^2/s. They compared this to a value obtained for polycrystalline $BaTiO_3$ of 1.4×10^{-17} m^2/s, but they did not report the source of this data.

The goal of this study was to determine what factors could be controlled to accelerate the growth of crystals by TGG. In contrast to the approach of Yamamoto and Sakuma, Ti-rich $BaTiO_3$ was used to create a liquid at the growth temperature and thus accelerate diffusion. It was found that appreciable growth could be achieved without using either pressure or a solution precursor to bond the template to the matrix. To gain a more fundamental understanding of the rate-controlling processes, the kinetics and thermodynamics of TGG were evaluated as a function of template orientation, temperature, and matrix composition. Growth rates are calculated as a function of template orientation.

III. Experimental Procedure

Single crystal $BaTiO_3$ cut-offs (Lockheed Sanders Inc., Nashua, NH) were used as template crystals for TGG. The orientation of the crystals was determined by four-circle X-ray or backscattered X-ray Laue analysis techniques. The crystals were sectioned along the desired crystallographic orientation using a diamond saw to sizes in the range of a few mm in size × 0.3 mm thick. One side of the template was polished with 1 μm diamond paste. Cut and polished surfaces were within ±1° of the desired crystallographic plane.

A high-purity (99.9%) and nanocrystalline (90 nm) $BaTiO_3$ powder (BT-01, Sakai Chemical Co., Ltd., Sakai, Japan) was used to fabricate the polycrystalline matrix. The powder was washed in pH 2.5-3.0 water. The pH of the slurry was maintained at 3-4 with HNO_3 and the slurry was stirred with occasional sonication for 5-10 minutes. The slurry was centrifuged to remove the supernatant containing leached barium. The powder was then re-washed with pH 2.5-3.0 water 1-3 times, to vary the amount of excess Ti in the sample. The leachant concentration was confirmed by inductively coupled plasma (ICP) analysis of the supernatant following each washing step. After the last washing, the powder was dispersed in ethanol and then poured into a Pyrex pan and dried overnight. The powder was rinsed in ethanol to remove any excess water which may lead to hard agglomerates during drying. After drying, the powder was sieved to < 44 μm (325 mesh). The granulated powder was uniaxially pressed at 35 MPa into discs 3 mm thick × 12.7 mm in diameter, and further cold isostatically pressed at 276 MPa. The green compacts were sintered in air at 1350°C for 2 h to achieve ~97% relative density with an average grain size of ~2 μm. Some compositions with less Ba leaching did not densify completely and had a range of grain sizes. For the grain growth studies the sintered samples were heated at 1350°C for 4 to 32 h and for 8 h at temperatures from 1350 to 1400°C.

Two different matrix compositions were used in this study. For later sections M1 refers to the matrix composition that was washed 3 times at pH 2.5-3.0 and had 2.4 mol% Ba leached from the powder, and M2 refers to the composition that was washed 3 times at pH 3.0 and had 1.4 mol% Ba leached from the powder.

For TGG one side of the sintered polycrystalline matrix was polished with 1 μm diamond paste and then one of the {100}, {111} or {110} surfaces of the template was brought into contact, without pressure, with the polished surface of the polycrystalline matrix and the assemblage was heated in air to 1350°C for 1 to 15 h. TGG was also carried out at temperatures ranging from 1350-1400°C to observe the effect of temperature on boundary migration.

Cross sections of the grown crystal in the polycrystalline matrix were examined by optical microscopy and scanning electron microscopy. After grain growth the samples were polished with 1 μm diamond paste and then thermally etched at 1300°C for 30 min. Porosity in the grown crystals and porosity and grain size of the polycrystalline matrix was measured by image analysis (NIH Image 1.6) of SEM images and confirmed by Archimedes measurements for the polycrystalline matrix. The kinetics of boundary migration were observed by measuring the maximum extent of boundary migration from the initial interface. For the (100) and (111) cases facets formed after a certain period of time, after which, the initial template plane was no longer the growing plane. Therefore, the data was separated for the different cases. To determine the composition of the grown crystals relative to the polycrystalline matrix, qualitative microprobe scans were performed along a cross section of the crystal growing into the polycrystalline matrix.

III. Results

(1) *Preliminary Experiments*

The Appendix describes a series of preliminary experiments that helped to define some of the systems for TGG used in this study. Some of the conclusions of that work are stated below. In contrast with Yamamoto and Sakuma,[15,16] there was negligible boundary migration of the single crystal template into the polycrystalline matrix when a stoichiometric matrix composition was heated at 1350°C for 8 h. However, when a Ti-rich composition was used, there was boundary migration above the eutectic temperature, 1332°C, due to the presence of a liquid phase.[4] The role of the liquid may be two-fold; one is that it provides a mechanism for contacting or bonding the single crystal template to the polycrystalline matrix and second is that it enhances diffusion in the system. Yamamoto and Sakuma used pressure to bond the crystal to the matrix prior to TGG. If the role of the liquid phase in this research is to achieve bonding between the crystal and matrix then, once bonded, the crystal should grow at temperatures below the eutectic temperature. However, an experiment in this research was conducted where a {100} oriented template crystal was allowed to grow at 1350°C for 30 minutes and then the temperature of the furnace was lowered to 1300°C and held for an additional 6 hours. The amount of boundary migration was the same as for samples grown at 1350°C for 30 minutes. Therefore, boundary migration is strongly controlled by the presence of a liquid phase.

(2) *Processing*

Leaching was used as the method to adjust the Ba/Ti ratio. As reported in the literature, washing in acidic solution leaches barium from the surface.[17] Figure 1 shows the theoretical phase stability diagram for the system Ba-Ti-CO_2-H_2O system. Because carbonate free water was not used it was important during washing to use a pH below 5 (See Figure 1), so that no $BaCO_3$ would form on the surface of the washed powder. Figure 2 shows a TEM micrograph of HNO_3-washed (pH ~ 3.0) particles. For the M1 matrix an approximately 7 nm amorphous layer can be observed surrounding the particle. This TiO_2-rich surface layer surrounds a stoichiometric $BaTiO_3$ core. Based on the amount of barium leached from the surface, 2.4 mol% Ba (equivalent to a Ba/Ti ratio of ~0.95), the equilibrium concentration of liquid at 1350°C is ≈ 5.5-6 vol%, assuming the entire Ti-rich layer reacts to form a liquid.

As mentioned before two different matrix powder compositions were prepared. M1 refers to the matrix composition that was washed 3 times at pH 2.5-3.0 and had 2.4 mol% Ba leached from the powder, and M2 refers to the composition that was washed 3 times at pH 3.0 and had 1.4 mol% Ba leached from the powder. There is a large difference in the amount of barium that was leached from these two samples with a small change in pH. This can be explained by the stability diagram for aqueous suspensions of TiO_2 as shown in Figure 3. As the pH approaches 2.5, the system is on the edge of the stability region where TiO_2 becomes soluble in H_2O. At pH above 2.5 an Ti-rich equilibrium leached layer forms and inhibits further barium leaching. In the pH range of 2.0-2.5 some titanium will also be leached, opening the Ti-rich leached layer and therefore allowing more barium to be leached from the $BaTiO_3$ particles. This is very similar to the corrosion behavior of glass surfaces. Figure 4 shows the five characteristic types of glass surfaces as characterized by Hench and Clark.[21] The $BaTiO_3$ system in this study is approximately a Type II and Type IV surface. The pH 3 leached particles have an equivalent Type II surface where it possesses a Ti-rich layer which protects or inhibits further leaching of barium from the underlying surface. The pH 2.5 surface is similar to a Type IV surface where Ba is leached from the surface, but leaching of Ti as well opens the surface to further leaching of Ba.

Figure 5 shows the cumulative mol% Ba with respect to $BaTiO_3$ that was leached for two different leaching conditions as a function of the number of HNO_3 washing steps. It shows that for S1 powder the amount of Ba leached was significantly higher than for S2 powder, although the amount leached with number of washes follows approximately the same trend. A summary of the characteristics of the ceramics prepared from matrix powder (B2) washed a different number of times and their resulting microstructural characteristics is given in Table 1. Table 1 shows that as the number of washings increases and hence the amount of Ba leached increases, the average density, average grain size and the amount of liquid phase at 1350°C increases. The amount of liquid at 1350°C was calculated from ICP data on barium concentration in the leachant. Although the leached layer is most likely an amorphous TiO_2, it was assumed that for every mole of Ba leached, 1 mole of TiO_2 was left behind. With the amount of barium leached from the surface the total starting powder, the amount of excess titanium with respect to the stoichiometric core of the $BaTiO_3$ particles was calculated and the amount of liquid phase was calculated from the phase diagram at a fixed temperature using the lever law. When the amount of liquid increases it may enhance diffusion for an increase in densification, but as a larger amount of liquid is formed, the diffusion path increases and hence the driving force for grain growth decreases.

Figure 6 shows the microstructure of a sintered acid-washed compact (M1) after 2 h at 1350°C. The compact has a density of 97% and an average grain size of 2 μm. Figure 7 is a plot of average grain size and the size of exaggerated grains as a function of annealing time at 1350°C. Using the data from Figure 7 for the matrix grain growth and assuming parabolic growth laws, a growth constant of 3.3×10^{-17} m^2/s is calculated, although the experimental fit to parabolic kinetics is not very good ($R \sim 0.92$). The R value for experimental fit to cubic growth law is even lower ($R \sim 0.91$). The best fit is for matrix grain growth which is proportional to time. Exaggerated grains do not appear in large quantities in the matrix for up to 8 h, at which time exaggerated grain growth begins to consume the polycrystalline matrix. After more than 32 h at 1350°C or after 8 h at temperatures above 1350°C (Figure 8) the entire matrix consists of 100 to 300 μm grains. This is essentially the same result reported by Yamamoto and Sakuma[16], except they reported a critical temperature of 1300°C for stoichiometric compact. Once nucleated, the exaggerated grains grow at approximately 9 μm/h in diameter.

(3) Kinetics

On the basis of the above observations, it appears that the optimum conditions for TGG occur at times less than 8h at 1350°C and before the onset of substantial matrix grain growth. Consequently most subsequent growths were done under these conditions.

Figures 9 and 10 show the habit planes of the growing crystals as a function of template crystal orientation after several hours at 1350°C. As determined by X-ray Laue techniques, all grown crystals have the same crystallographic orientation as the template crystals. For samples with {100} and {111} oriented templates, boundary migration perpendicular to the template/matrix initial interface is initially fast (180 and 590 μm/h, respectively for M1 matrix composition) but the fast growing planes grow themselves out and slower growing surfaces are formed. A schematic representing this is shown in Figure 9c and 10b for {100} and {110} oriented templates, respectively. The shape of the crystal grown from a {100} oriented template is a pyramid with (100) basal plane and four equivalent habit planes which were undetermined because the boundary did not lie near any primary crystallographic plane although they formed an angle of approximately 35° with the original template face. For the {110} template crystal the boundary remains relatively flat as slow growth rates (40 μm/h for M1 matrix composition) are observed in directions both parallel and normal to the initial boundary. A cross-section view of a crystal grown from an {111} oriented template is shown in Figure 9b. Although, the fast growing planes of crystals grown from this orientation also grew themselves out similar to a {001} oriented template, the habit planes that formed were not determined due to the complexity of the grown shape. Variability in the angles that the new facets formed with respect to the initial interface could not be accounted by the error in orientation associated with the crystal preparation which was ±1°. Some of the planes formed an angle of approximately 35° with respect to the initial template (which would represent {110} planes), but the observed shape depended on how the sample was sectioned.

Figure 11 shows a larger magnification of the interface of a growing crystal and the polycrystalline matrix for a {100} oriented template after 8 h at 1350°C. At this magnification the boundary is relatively flat and there is no evidence for grain boundary curvature as seen in other TGG work.[13]

The optimum growth temperature for TGG was determined by growing crystals with a {110} template orientation for 8 h at temperatures ranging from 1350 to 1400°C. The {110} orientation was used because the boundary migration rate is not affected by the formation of habit planes. Hence any decrease in the boundary migration rate will be due to either thermodynamic effects or kinetic effects. Figure 12 shows the boundary migration as a function of TGG temperature for 8 h. The extent of boundary migration decreases with increasing temperature. The decrease is due to coarsening of the matrix grains at temperatures greater than 1350°C (See this chapter, Section (1)), which results in a decrease in the driving force for migration. On the basis of the phase diagram[4] an increase in temperature also causes the amount of liquid to increase and hence the thickness of the liquid layer, unless through capillary action the liquid begins to fill the pores at high temperatures. From SEM observations there was no buildup of a Ti-rich phase at the interface and therefore the liquid was either filling the pores or being redistributed throughout the matrix. In either case the coarsening of the grains is the major factor for a decrease in the driving force. From the data reported above it was determined that the optimum conditions for TGG were 1350°C for times up to 8 h.

Figures 13 and 14 show boundary migration as a function of time and template crystal orientation at 1350°C for matrix compositions M1 and M2. A template orientation of {111} results in the fastest boundary migration rate prior to habit plane formation, ~590 and 790 µm/h for M1 and M2, respectively. A template orientation of {100} results in an initial boundary migration rate of approximately 180 and 480 µm/h for M1 and M2, respectively, however with both the {100} and {111} orientations, the boundary migration rate slows to approximately 30 µm/h once the habit planes form. As shown below these rates are close to the rates for growth from a {110} oriented template. For the {110} template orientation, the initial boundary migration rate is 40 and 60 µm/h for M1 and M2, respectively. Growth continues at a relatively constant rate, until at times greater than 7 h when the rate slows to rates approximately 10 µm/h slower, most likely due to a decrease in the driving force associated with matrix grain growth. At times greater than 10 h impingement with exaggerated grains hinders the boundary migration further. It is observed that the growth behavior as a function of template orientation follows similar trends for both matrix compositions and the growth rate remains constant up to facet formation, although the absolute growth rates change. The rates all increase 1.5-2.5 times for matrix composition M2. These are the rates that are used in Chapter 4 for application of a model to the TGG growth mechanisms, where the rate change will be addressed in more depth.

One result of the different boundary migration rates is that varying amounts of porosity are trapped in the grown crystal. The initial matrix porosity is approximately 3.0 to 4.0 vol%. For the {111} oriented template crystals, which initially grow the fastest, all of the matrix porosity is trapped in the crystal. The {100} oriented template samples are able to sweep ~2 vol% of the pores out, resulting in a grown crystal with approximately 1.5 vol% pores. This trend is observed for all the samples, in that as the boundary migration rate decreases, so does the vol% trapped porosity. All samples retain at least some portion of porosity, which limits the applications of the grown crystals. This problem should be alleviated by starting with a fully dense ceramic.

Figure 15 shows the extent of boundary migration as a function of template crystal size for {001} oriented templates at 1350°C. If a larger template is used (6 × 6 mm, instead of 3 × 3 mm), the extent of boundary migration can be increased, resulting in larger grown crystals. The difference for the 3 × 3 mm template, is that a fully faceted crystal is observed after ~0.7 mm of growth. As shown, the extent of boundary migration after 8 h is approximately twice that of the smaller template. Hence, the extent of boundary migration is a function of template size, whereas the boundary migration rate is a function of template orientation. The size of the template crystal limits the lateral size of the grown crystal that can be produced since relatively little lateral growth is observed. From Figure 14, the growth from a {100} oriented template appears to be time dependent in the initial state of growth if a small template is used, but as shown in Figure 15 the growth continues essentially at the same rate with time until a facet forms.

It is possible to use template crystals other than $BaTiO_3$ to grow $BaTiO_3$ single crystals. Single crystals of $BaTiO_3$ were grown in the same manner as described above by using a single crystal of $SrTiO_3$ as the template crystal as shown in Figure 16 for an M1 polycrystalline matrix. The template crystal was {100} oriented and the boundary migration rates were similar to those grown with {100} oriented $BaTiO_3$ crystals, ~200 µm/h. Microprobe analysis showed that only an approximately 5 to 10 µm region at the interface contained interdiffused Sr and Ba, and the Ba/Ti ratio remained constant throughout the rest of the grown crystal. The ability to use alternative templates makes the TGG method much more flexible in terms of the crystal compositions which can be grown.

(4) Composition of TGG-Grown $BaTiO_3$ Crystals

Since the ceramic produced from the acid-washed powder is Ti-rich, at the temperatures used for TGG, 1350°C, a liquid phase forms. The Ti-rich layer reacts with $BaTiO_3$ to form the hexabarium titanate, $Ba_6Ti_{17}O_{40}$, followed by the subsequent formation of $BaTiO_3$ and a Ti-rich liquid phase at temperatures greater than 1332°C.[4] Figure 17 shows the boundary between the TGG single crystal and the polycrystalline matrix after 10 h at 1350°C. As evidence of the high temperature liquid phase, dark regions can be seen that have segregated into pools in the polycrystalline matrix. These dark regions are hexabarium titanate that has crystallized from regions that had high titanium concentration. In these micrographs the liquid does not appear to build up along the boundary between the grown crystal and the matrix, but it is difficult to estimate the distribution of liquid at high temperatures. The question that arises is what happens to this excess Ti-rich liquid during TGG and what influence it has on the grown crystal.

Figure 18a and 18b gives the results of microprobe analysis on a grown crystal. Figure 18a shows a backscattered scanning electron micrograph of a template crystal on top of a grown crystal region in a polycrystalline matrix. The lighter regions on the left are exaggerated grains, while the black circular objects are pores. There is also a variation in color in the polycrystalline matrix, which is the result of regions of $Ba_6Ti_{17}O_{40}$ and $BaTiO_3$ as shown in Figure 17.[22] The direction of the microprobe scan is shown on Figure 18 as a white arrow as it scanned from the grown crystal, across the single crystal / polycrystalline boundary, and into the polycrystalline matrix. Figure 18b shows the result of the scan. It can be seen that the Ba/Ti ratio remains constant throughout the grown crystal and the signal only changes as the scan crosses over pores (which is shown on Figure 18b as a drop in both the Ba and Ti signals). As the scan crosses the boundary there is no indication of a buildup of a Ti-rich phase. However, as the scan continues into the matrix, drops in the Ba signal accompanied by increases in the Ti signal are observed. This is the result of passing through the $Ba_6Ti_{17}O_{40}$ phase regions. This information coupled with the dielectric property and high field measurements conducted in Chapter 5 suggest that the Ba/Ti ratio is constant through the grown crystal and also that the crystals are close to stoichiometric. Therefore, although the matrix contains excess Ti, and this aids the TGG process kinetically through the formation of a liquid phase, it is not incorporated into the grown crystals.

IV. Conclusions

Templated grain growth provides a potentially inexpensive method for producing single crystals of various materials relative to current high temperature solution techniques. It is an alternative to conventional high temperature solution techniques with similar growth rates. In this study the growth of single crystals of $BaTiO_3$ were studied to better understand the role of kinetics and thermodynamics on the TGG process. The results of this study are summarized below. $BaTiO_3$ single crystals of mm-size can be produced by heating a 97% dense polycrystalline matrix (grain size ~ 2 μm) with a Ba/Ti ratio < 1 for 8 h at 1350°C. Boundary migration rates are a function of template orientation, with rates as high as 790 μm/h from a {111} oriented template. The maximum extent of boundary migration is approximately proportional to the template size. Boundary migration rates slow when habit planes are formed. The Ba/Ti ratio of the grown crystal remains constant. It is important to use processing conditions that avoid the presence of exaggerated grains, because once the grains reach a critical size (>30 μm), they either inhibit the migration of the single crystal boundary or are incorporated into the growing crystal. This has been demonstrated for both the barium titanate[16] and manganese zinc ferrite[11] systems.

Acknowledgement: We would like to thank Shangcong Cheng (Materials Characterization Laboratory, Penn State) for TEM, Mark Angelone (Materials Characterization Laboratory, Penn State) for microprobe analysis and Dr. W. Coblenz for helpful comments. Financial support from the Defense Advanced Research Projects Agency on AFSOR Grant No. F49620-94-1-0428, DARPA contract N00014-93-0502, and on ONR Grant No. N00014-98-1-0527 are gratefully acknowledged.

References

1) A. Linz, V. Belruss and C. S. Naiman, "Solution-Grown Perovskites," *J. Electrochem. Soc.*, **112** [6] 60C (1965).

2) D. Rytz, B. A. Wechsler, C. C. Nelson and K. W. Kirby, "Top-seeded Solution Growth of $BaTiO_3$, $KNbO_3$, $SrTiO_3$, $Bi_{12}TiO_{20}$ and $La_{2-x}Ba_xCuO_4$," *J. Crystal Growth*, **99** [4-Jan] 864-8 (1990).

3) Y. Tomita, "Technique for Preparation of $BaTiO_3$ Single Crystal," *New Ceram.*, **4** [5] 1-6 (1991).

4) K. W. Kirby and B. A. Wechsler, "Phase Relations in the Barium Titanate-Titanium Oxide System," *J. Am. Ceram. Soc.*, **74** [8] 1841-7 (1991).

5) Y.-S. Yoo, M.-K. Kang, J.-H. Han, H. Kim and D.-Y. Kim, "Fabrication of $BaTiO_3$ Single Crystals by Using the Exaggerated Grain Growth Method," *J. Eur. Ceram. Soc.*, **17** 1725-1727 (1997).

6) D. E. Rase and R. Roy, "Phase Equilibrium in the System $BaTiO_3$-TiO_2," *J. Am. Ceram. Soc.*, **38** 102-113 (1955).

7) D. Kolar, "Discontinuous Grain Growth in Multiphase Ceramics," *Ceram. Trans.*, **7** 529-545 (1988).

8) D. F. K. Hennings, R. Janssen and P. J. L. Reynen, "Control of Liquid-Phase-Enhanced Discontinuous Grain Growth in Barium Titanate," *J. Am. Ceram. Soc.*, **70** [1] 23-7 (1987).

9) Y.-S. Yoo, H. Kim and D.-Y. Kim, "Effect of SiO_2 and TiO_2 Addition on the Exaggerated Grain Growth of $BaTiO_3$," *J. Eur. Ceram. Soc.*, **17** 805-811 (1997).

10) M. Demartin, C. Herard, C. Carry and J. Lemaitre, "De-densification and Anomalous Grain Growth During Sintering of Undoped Barium Titanate," *J. Am. Ceram. Soc.*, **80** [5] 1079-84 (1997).

11) S. Matsuzawa and S. Mase, "Method for Producing a Single Crystal of Ferrite," *U.S. Patent 4339301* (Jul. 13, 1982).

12) M. Imaeda and S. Matsuzawa, "Growth of Yttrium Iron Garnet Single Crystal by Solid-Solid Reaction," *1st Japan International SAMPE Symposium*, 419-24 (Nov. 28-Dec. 1, 1989).

13) T. Li, A. M. Scotch, H. M. Chan, M. P. Harmer, S. Park and T. R. Shrout, "Single Crystals of $Pb(Mg_{1/3}Nb_{2/3})O_3$-35 mol% $PbTiO_3$ from Polycrystalline Precursors," *J. Am. Ceram. Soc.*, **81** [1] 244-8 (1998).

14) R. C. DeVries, "Growth of Single Crystals of $BaTiO_3$ by Exaggerated Grain Growth," *J. Am. Ceram. Soc.*, **47** [3] 134-6 (1964).

15) T. Yamamoto and T. Sakuma, "Preparation of $BaTiO_3$ Single Crystals by Sintering," *2nd Japan International SAMPE Symposium*, 209-15 (Dec. 11-14, 1991).

16) T. Yamamoto and T. Sakuma, "Fabrication of Barium Titanate Single Crystals by Solid-State Grain Growth," *J. Am. Ceram. Soc.*, **77** [4] 1107-9 (1994).

17) D. A. Anderson, J. H. Adair, D. Miller, J. V. Biggers and T. R. Shrout, "Surface Chemistry Effects on Ceramic Processing of $BaTiO_3$ Powder," pp. 485-492 in Ceramic Powder Science II. Vol.1, Westerville, OH., 1988.

18) P. Bendale, S. Venigalla, J. R. Ambrose, E. D. Verink, Jr., J. H. Adair, "Preparation of Barium Titanate Films at 55°C by an Electrochemical Method," *J. Am. Ceram. Soc.*, **76** [10] 2619-27 (1993).

19) M. Pourbaix, Atlas of Electrochemical Equilibria in Aqueous Solutions, 2nd English Ed., 1974, translated by J. A. Franklin, National Association of Corrosion Engineers, Houston TX.

20) C. F. Bases, Jr., and R. E. Mesmer, The Hydrolysis of Cations, John Wiley and Sons, Inc., New York, 1976.

21) L. L. Hench and D E. Clark, "Physical Chemistry of Glass Surfaces," *J. Non-Cryst. Solids*, **28**, 83-105 (1978).

22) H. Oppolzer and H. Schmelz, "Investigation of Twin Lamellae in $BaTiO_3$ Ceramics," *J. Am. Ceram. Soc.*, **66** [6] 444-6 (1983).

List of Figures

Fig. 15 Maximum boundary migration as a function of template size and time at 1350°C for M2 and a {001} oriented template.

Fig. 16 Scanning electron micrograph of a $BaTiO_3$ crystal grown into a Ti-rich polycrystalline matrix (M1) after 8 h at 1350°C from a {100} oriented $SrTiO_3$ template (Bar = 500 μm).

Fig. 17 Scanning electron micrograph of TGG single crystal and polycrystalline boundary after 10 h at 1350°C, showing evidence of segregation of $Ba_6Ti_{17}O_{40}$ (Bar = 100 μm). Outline indicates area of higher magnification (Bar = 20 μm).

Fig. 18 (a) Backscattered scanning electron micrograph of boundary between grown crystal and polycrystalline matrix. (b) Microprobe scan of boundary between TGG single crystal and polycrystalline matrix along path shown in the scanning electron micrograph.

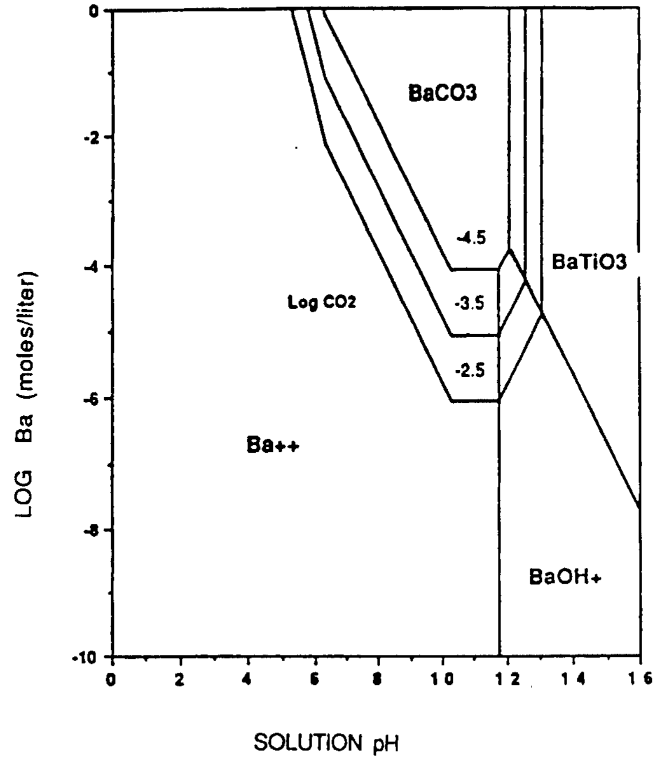

Fig. 1 The theoretical phase stability diagram for the Ba-Ti-CO_2-H_2O system. [From Bendale *et al.*, 1993][19]

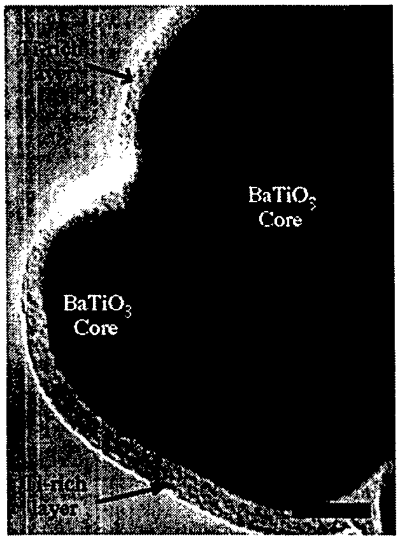

Fig. 2 Transmission electron micrograph of HNO_3-washed (pH ~ 3.0) $BaTiO_3$ particles (M1 matrix composition. (Bar = 25 nm)

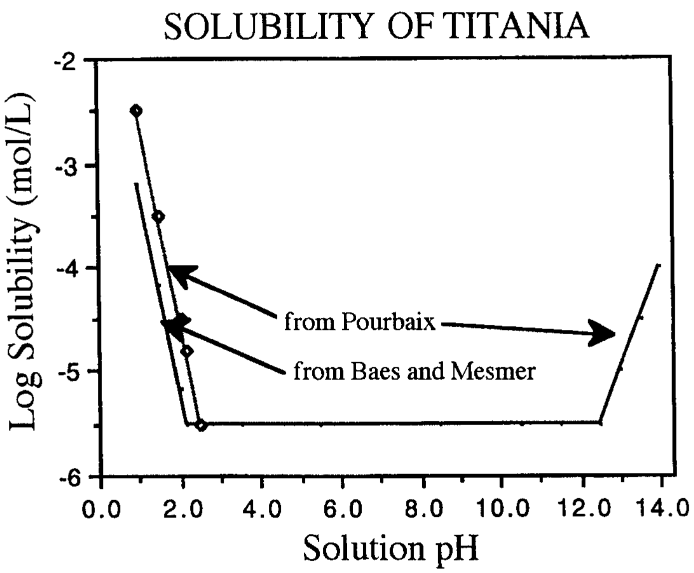

Fig. 3 The theoretical stability diagram for aqueous TiO_2 suspensions. [After data from Porbaix, 1974[19] and Bases and Mesmer, 1986[20]]

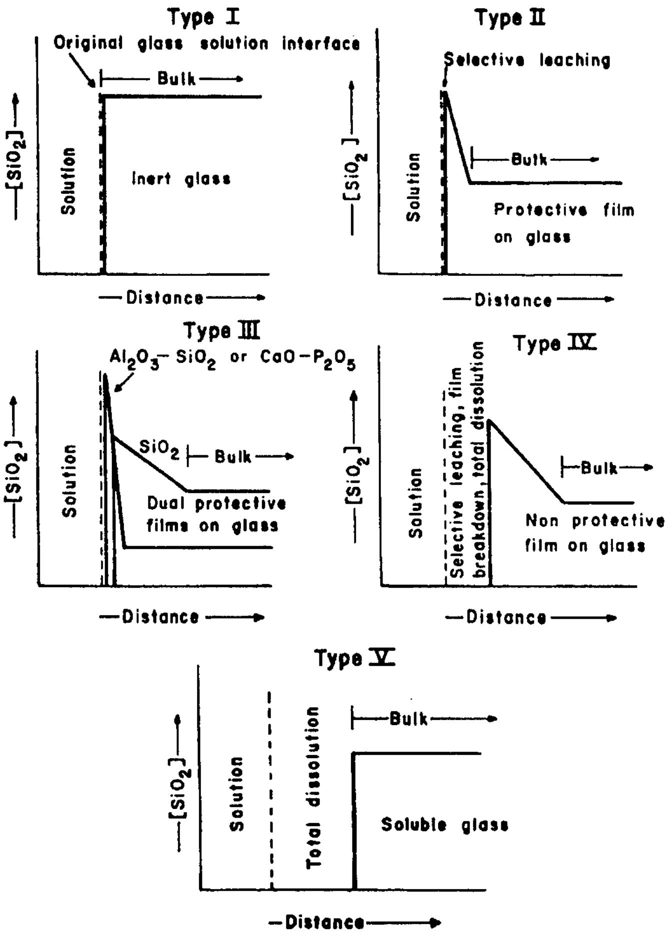

Fig. 4 Five characteristic types of glass surfaces. (From Hench and Clark, 1978)[21]

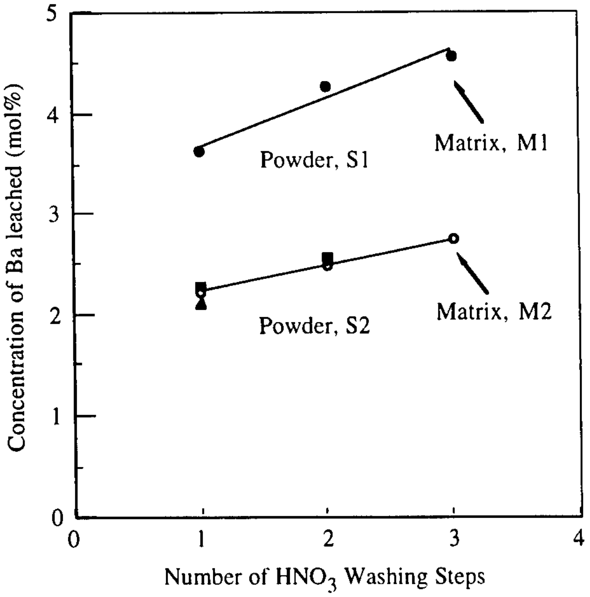

Fig. 5 Concentration of barium leached from $BaTiO_3$ powder as a function of nitric acid washing steps. The differences between matrix powder S1 and matrix powder S2, were leaching pH as well as the storage conditions which may have lead to aging effects.

Table 1 Acid-washed matrix (B2) powder characteristics showing cumulative mol% barium leached as well as the number of acid washings and the resulting physical characteristics of ceramics sintered at 1350°C for 2 h.

Number of HNO_3 washings	Leached Ba (mol%)	Density (% ρ_{theor})	Grain Size (μm)	Liquid at 1350°C (mol%)
3	2.7	94.8	2.3±1.3	4.0
2	2.6	91.2	3.5±1.7	3.7
1	2.1	82.4	4.4±2.3	3.0

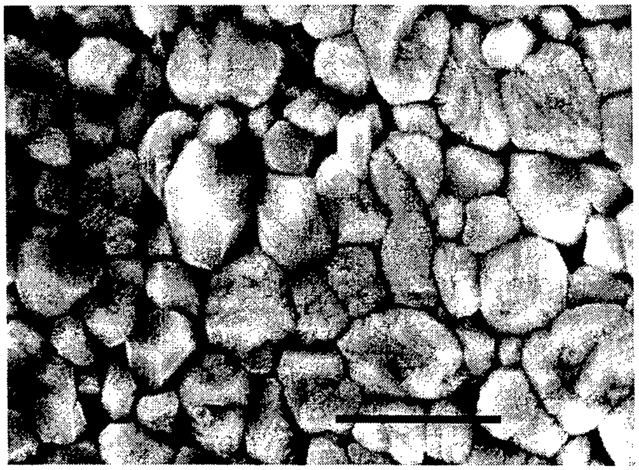

Fig. 6 Scanning electron micrograph of the microstructure of the polycrystalline matrix sintered at 1350°C for 2h (M1 matrix composition). (Bar = 5 μm)

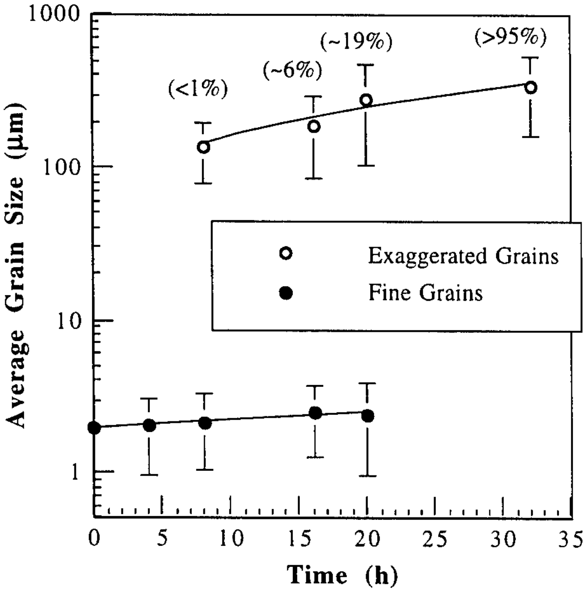

Fig. 7 Average matrix grain size as a function of annealing time at 1350°C for sintered compacts of M1. Parentheses indicate volume percent exaggerated grains. (Error bars indicate the average standard deviation in the grain size measurement of 3 different samples)

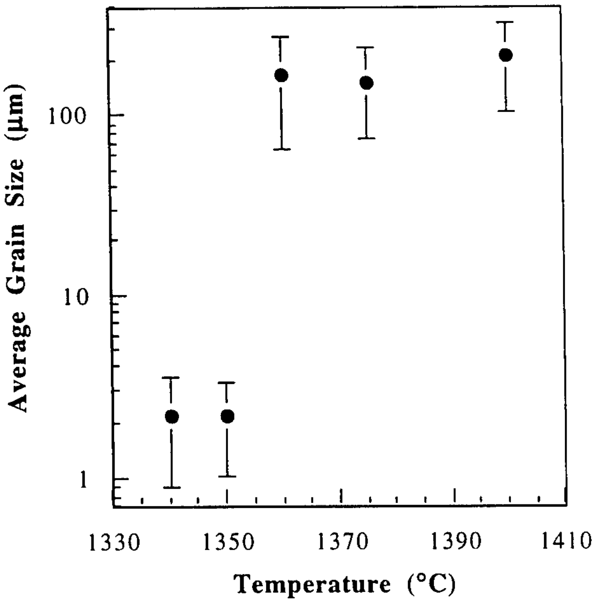

Fig. 8 Average matrix grain size as a function of annealing temperature for 8 h anneals of M1. (Bars indicate the average standard deviation in the grain size measurement of 3 different samples)

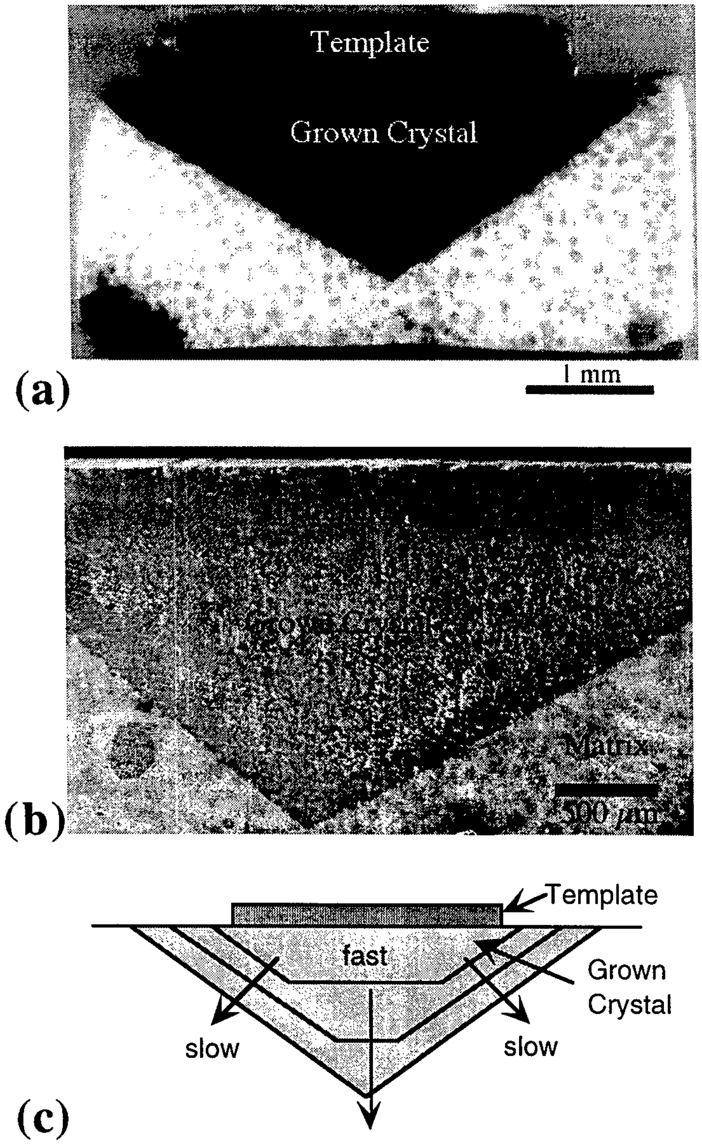

Fig. 9 (a) Optical micrograph of a $BaTiO_3$ crystal grown into a Ti-rich polycrystalline matrix after 8 h at 1350°C from a {100} oriented template (Bar = 1 mm). (b) SEM micrograph of a $BaTiO_3$ crystal grown into a Ti-rich polycrystalline matrix after 5 h at 1350°C from a {111} oriented template (Bar = 500 μm). (c) Schematic showing habit plane formation for growth from {100} oriented templates.

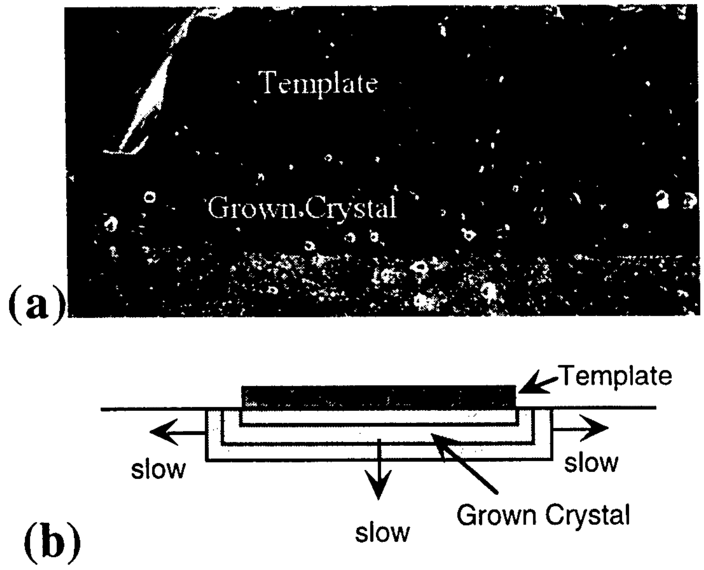

Fig. 10 (a) Scanning electron micrograph of a $BaTiO_3$ crystal grown into a Ti-rich polycrystalline matrix after 8 h at 1350°C from a {110} oriented template (Bar = 0.1 mm). (b) Schematic showing habit plane formation for growth from {110} oriented templates.

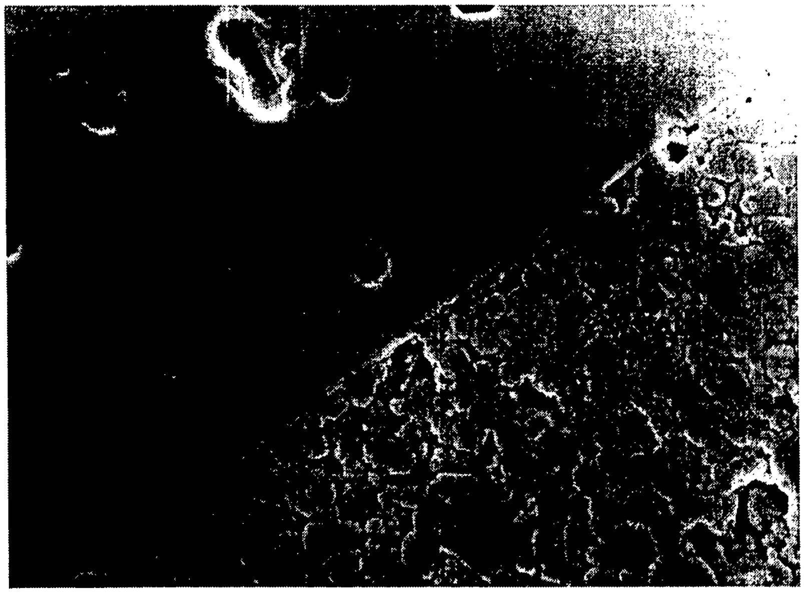

Fig. 11 Scanning electron micrograph of the interface of a $BaTiO_3$ crystal grown into a Ti-rich polycrystalline matrix after 8 h at 1350°C from a {100} oriented template (Bar = 25 μm).

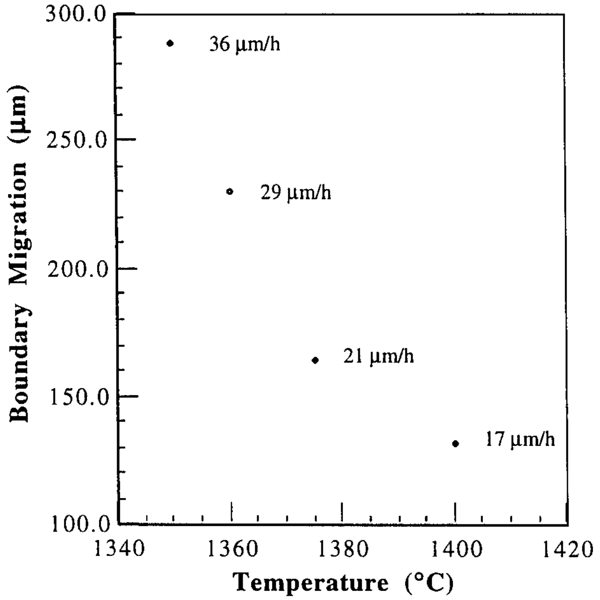

Fig. 12 Boundary migration as a function of temperature for M1 and a {110} oriented template. All dwell times were 8 h and numbers indicate approximate growth rates.

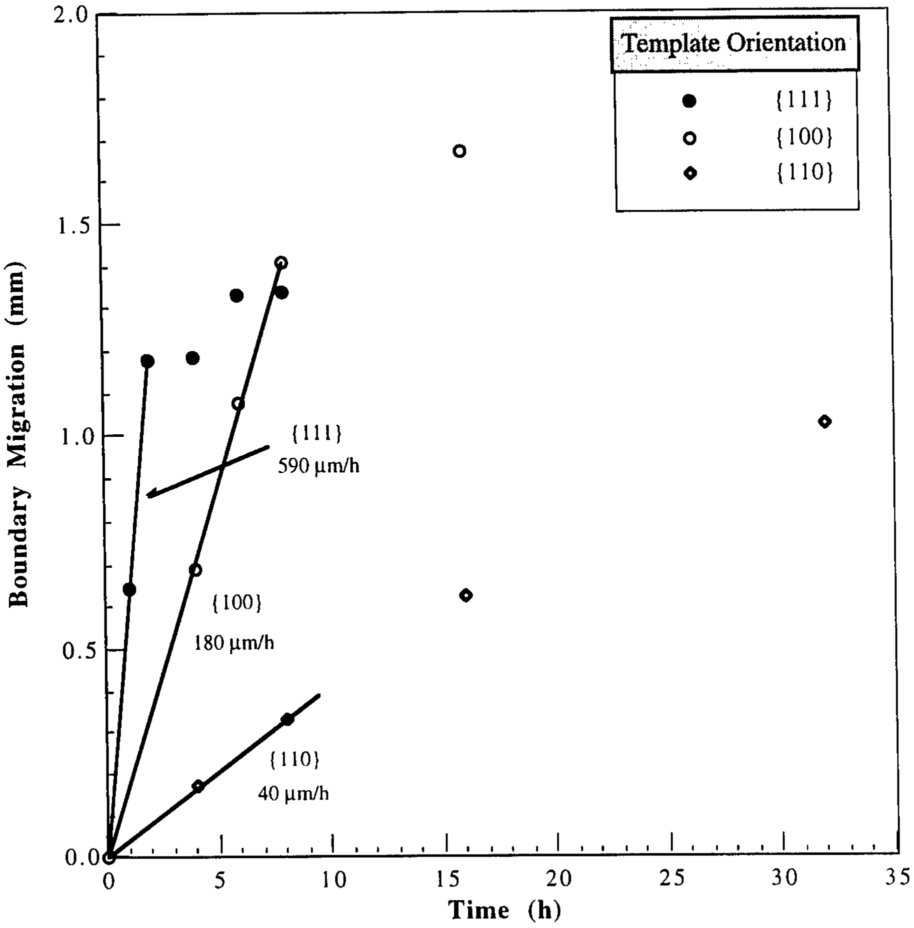

Fig. 13 Maximum boundary migration as a function of template orientation and time at 1350°C for M1. Growing planes are represented by {hkl} symbols next to appropriate lines. The growing plane changes for templates with an initial orientation of {100} or {111} after facet formation.

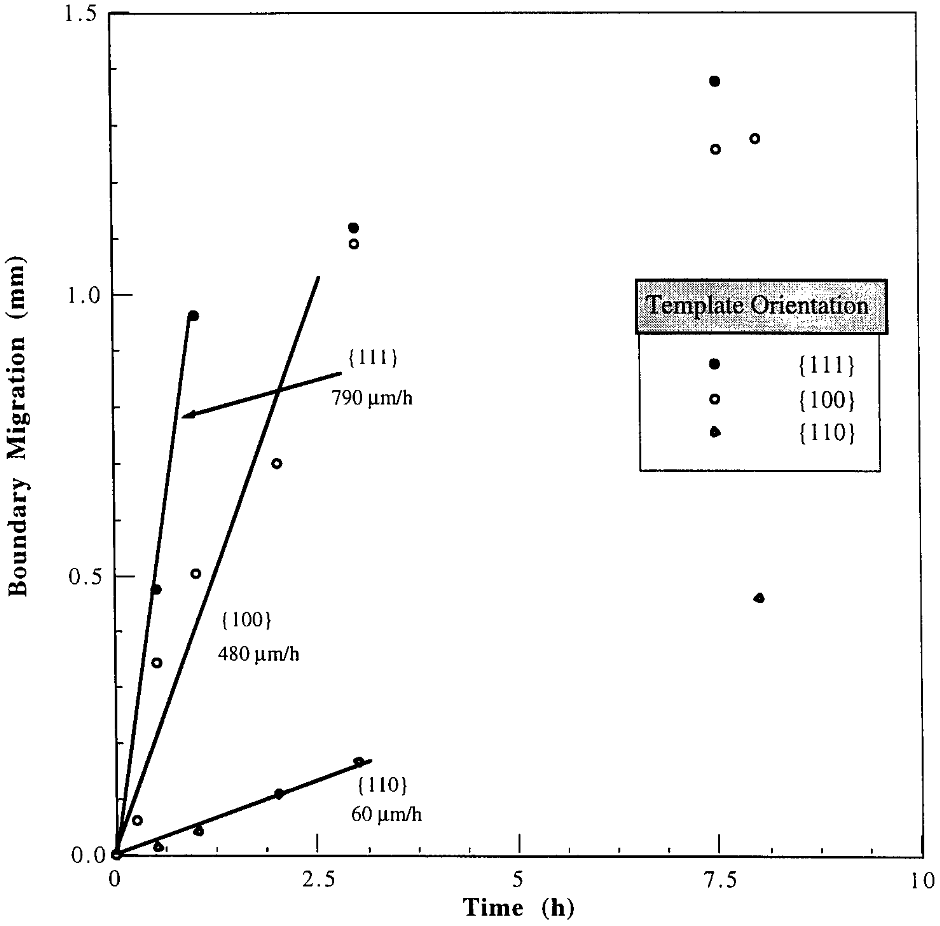

Fig. 14 Maximum boundary migration as a function of template orientation and time at 1350°C for M2. Growing planes are represented by {hkl} symbols next to appropriate lines. The growing plane changes for templates with an initial orientation of {100} or {111} after facet formation.

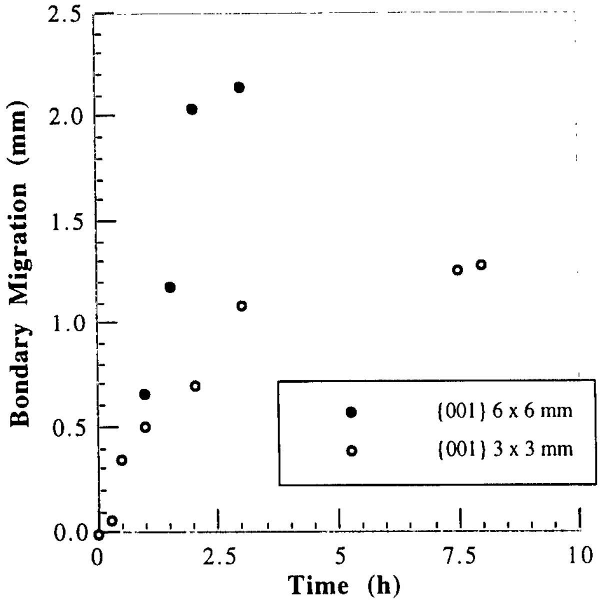

Fig. 15 Maximum boundary migration as a function of template size and time at 1350°C for M2 and a {001} oriented template.

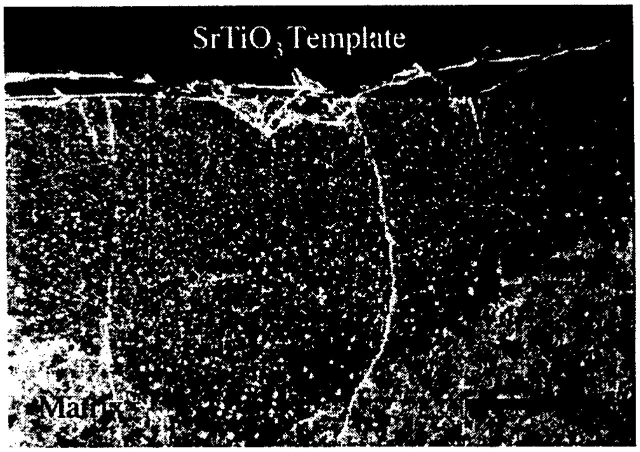

Fig. 16 Scanning electron micrograph of a $BaTiO_3$ crystal grown into a Ti-rich polycrystalline matrix (M1) after 8 h at 1350°C from a {100} oriented $SrTiO_3$ template (Bar = 500 μm).

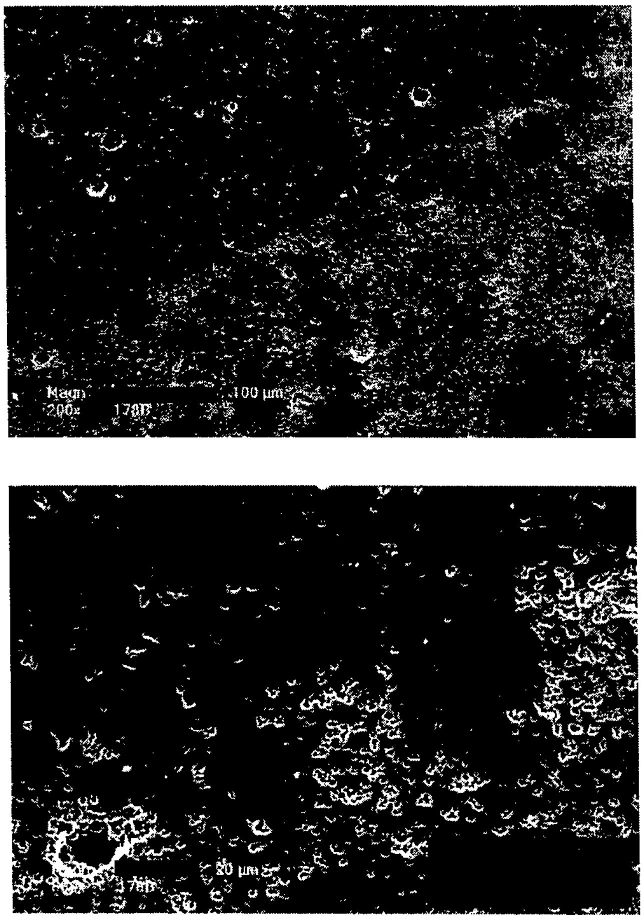

Fig. 17 Scanning electron micrograph of TGG single crystal and polycrystalline boundary after 10 h at 1350°C, showing evidence of segregation of $Ba_6Ti_{17}O_{40}$ (Bar = 100 µm). Outline indicates area of higher magnification (Bar = 20 µm).

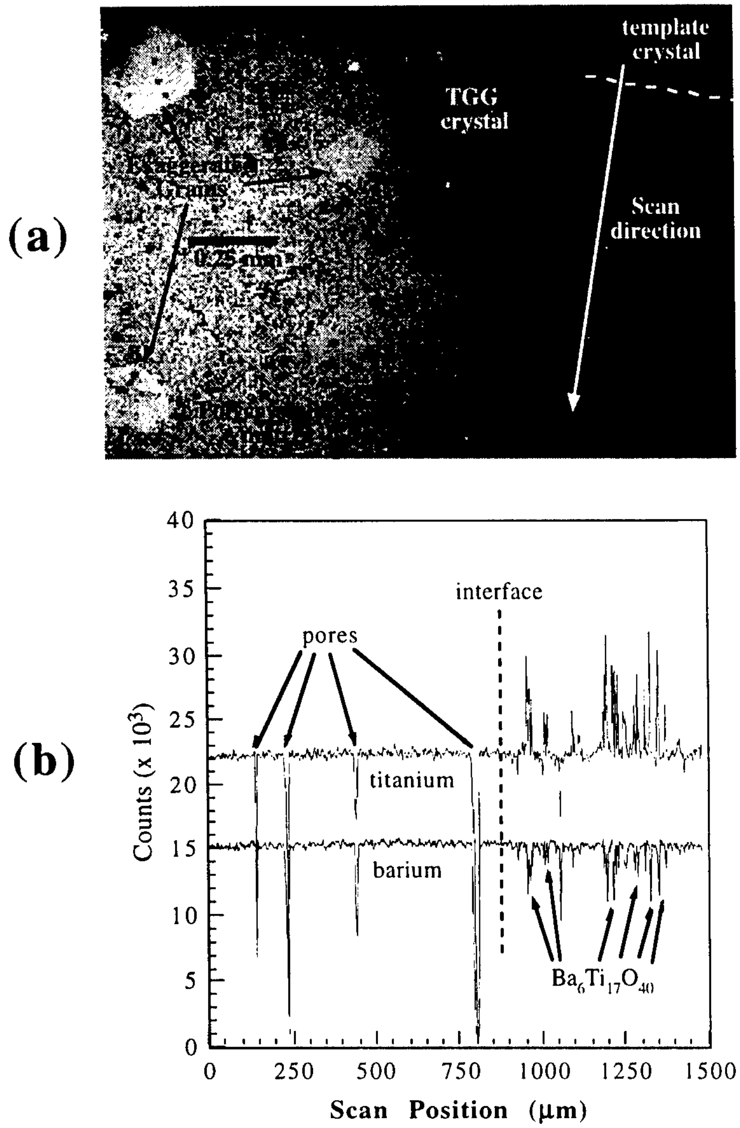

Fig. 18 (a) Backscattered scanning electron micrograph of boundary between grown crystal and polycrystalline matrix. (b) Microprobe scan of boundary between TGG single crystal and polycrystalline matrix along path shown in the scanning electron micrograph.

APPENDIX B

DIELECTRIC AND ELECTROMECHANICAL PROPERTIES OF BARIUM TITANATE SINGLE CRYSTALS GROWN BY TEMPLATED GRAIN GROWTH

Paul W. Rehrig,* Susan Trolier-McKinstry,* Seung-Eek Park,* and Gary L. Messing,*
Materials Research Laboratory, The Pennsylvania State University, University Park, Pennsylvania 16802

Single crystals of $BaTiO_3$ were grown by templated grain growth (TGG). TGG involves contacting a single crystal "template" to a sintered polycrystalline matrix and then heating the assemblage to a temperature that promotes the migration of the single crystal boundary through the matrix. In this investigation the properties of mm-sized single crystals of $BaTiO_3$ grown by TGG were examined and evaluated. A dielectric constant, ε_{33}^T, of 260, polarizations of $P_R \sim 12\ \mu C/cm^2$ and $P_{sat} \sim 21.5\ \mu C/cm^2$, electromechanical coupling coefficients of $k_{33} \sim 0.51$ and $k_{31} \sim 0.18$, and piezoelectric coefficients of $d_{33} \sim 133$ pC/N and $d_{31} \sim -25$ pC/N were achieved. It was found that entrapped porosity in the crystals made it difficult to fully pole the crystals.

Based in part on the thesis submitted by Paul W. Rehrig for the Ph.D. degree in Materials Science and Engineering, Pennsylvania State University, University Park, PA 1998.

Supported by the Defense Advanced Research Projects Agency, under AFOSR Grant # F49620-94-1-0428

* Membership in the American Ceramic Society

I. Introduction

The properties of $BaTiO_3$ single crystals have been studied since soon after its discovery in 1943. Early studies were conducted on flux grown crystals produced by the Remeika technique.[1] More recently, other crystal growth techniques such as the floating-zone method and top-seeded solution growth (TSSG) provided larger and higher quality crystals with fewer residual impurities and defects.[2-5] In recent years there has been increasing research to develop alternative routes to growing single crystals that would reduce both the cost and time consuming nature of current techniques.

One of the techniques which has been applied to the $BaTiO_3$ system is templated grain growth (TGG).[6-10] Single crystals of $BaTiO_3$ on the order of a few millimeters in size have been produced this way.[10]

As observed before, the properties of crystals grown by different flux or melt techniques can differ appreciably.[11] Impurities can shift the Curie temperature while porosity can decrease the dielectric constant, electromechanical coupling coefficients, and the transverse piezoelectric coefficient.[11-13] Of particular concern in the current work is that, to date, TGG $BaTiO_3$ single crystals incorporate some of the original matrix porosity. Therefore it was the purpose of this research to determine how this affects the dielectric and electromechanical properties of single crystals of $BaTiO_3$ grown by TGG.

II. Experimental Procedure

The processing used follows that described in Chapter 3. The crystals used for property measurements were grown from {001} templates by heating in air to 1350°C for 10 h. Grown crystals were sectioned from the template and polycrystalline matrix so that property measurements were performed on the grown crystals alone (i.e. none of the original $BaTiO_3$ crystal remained). The faces of grown crystals were oriented along {001} via X-ray Laue techniques and polished with 1 μm diamond paste, followed by gold-sputtering to form electrodes. A multifrequency meter (HP 4284A LCR meter) was used in conjunction with a computer controlled temperature chamber (Delta Design Inc., Model MK 9023) to measure the dielectric constant as a function of temperature on cooling (175°C to -100°C) at frequencies between 100 Hz and 100 kHz. A multifrequency meter (HP 4274A LCR meter) was used in conjunction with a computer controlled temperature chamber (Delta Design Inc., Model MK 2300) to measure the pyroelectric current as a function of temperature from room temperature to 135°C. The sample was poled by field cooling in the sample holder at 10 kV/cm in air, and then just prior to pyroelectric current measurement the field was removed. The saturation polarization was calculated by integrating the pyroelectric current as a function of temperature.

High field measurements (1-50 kV/cm) on ⟨001⟩ oriented crystals included simultaneous polarization (P) and strain (S) hysteresis curves obtained using a computer-controlled modified Sawyer Tower system and a linear variable displacement transducer (LVDT) sensor driven by a lock in amplifier (Stanford Research Systems, Model SR830). The voltage was supplied using either a Trek 609C-6 high voltage DC amplifier or a Kepco BOP 1000M amplifier. The same system was used to measure unipolar strain curves on poled ⟨001⟩ oriented crystals. The value for d_{33} was estimated from the slope of the unipolar strain vs. electric field (E) curve. Electromechanical coupling was measured using the IEEE resonance technique (ANSI/IEEE Std. 176-1978).

III. Results and Discussion

(1) Dielectric Properties

Figure 1 shows the dielectric constant (a) and dielectric loss (b) as a function of temperature and frequency for an unpoled TGG crystal. The crystal exhibited very little dispersion in the dielectric constant as a function of temperature. The transition temperatures occur at, $T_{O\text{-}T}$ (orthorhombic-tetragonal)= 9°C, and T_C (Curie temperature) = 131°C. This is in good agreement with the literature for pure single crystals of $BaTiO_3$.[11,14] The 1 kHz room temperature dielectric constant and loss for the unpoled crystal are approximately 2570 and 0.003, respectively. The value for dielectric constant is approximately what is expected for an unpoled crystal where the domains are randomly oriented. The trapped porosity will also lower the dielectric constant due to mixing rules.[15] If logarithmic mixing rules are assumed, for 3 vol% porosity a room temperature dielectric constant of 3280 is calculated for a fully dense crystal. Figure 2 shows the temperature dependence of the dielectric constant along the a (ε_a) and c (ε_c) axes in the tetragonal phase measured at1 kHz on poled samples. The room temperature values of ε_a and ε_c are 2430 and 770, respectively. Although the trends shown in Figure 2 is the same as reported in the literature,[11] the values for ε_a and ε_c are too low and too high, respectively as shown in Table 1. This is because the samples partially depole after removal of electric fields. The 1 kHz room temperature dielectric loss measured along the a-axis and c-axis was 0.005 and 0.009, respectively. One of major contributions to dielectric loss at room temperature is domain wall motion; the low values suggest that the mobility of some of the domain walls is low.

Above T_C the Curie-Weiss law is obeyed with Curie constants and Curie-Weiss temperatures in the range of C = 1.5-2.0 × 10^5°C and T_0 = 107-116°C, respectively; i.e. $\varepsilon_R \cong 1.8\times10^{5\,\circ}C/(T-112^\circ C)$ (averaged values). If the dielectric data is corrected with logarithmic mixing laws to account for porosity, the Curie constant is 0.3 × 10^5°C higher and the Curie-Weiss temperature is decreased 1-2°C. The observed value for the Curie constant is in the range expected for $BaTiO_3$ single crystals (on the order of ~10^5 °C), and is in very good agreement with Wemple *et al.*[14] who reported a value of C = 1.8 × 10^5°C. The Curie-Weiss temperature is also in good agreement with a reported value of 112°C.[14]

Figure 3 shows the small signal dielectric constant as a function of DC bias along the c-axis. The sample was measured with a small AC signal over the externally applied DC bias. Although the sample was poled by field cooling prior to the room temperature capacitance measurement, the sample exhibited a dielectric constant higher than expected, indicating that the sample was not fully poled. The measurement was taken with the application of a DC bias in an attempt to pole the sample as fully as possible and therefore approach the true ε_{33}^{T} (T = stress free state) value. This led to a room temperature ε_{33}^{T} = 260±10 at 18 kV/cm, suggesting that even at high field, not all domains were aligned with the applied field. This is probably due to pinning of domains by the defects in the crystal, namely the entrapped pores. The pores may be considered as macro-sized defects, where the local electric field is distorted and localized strain effects pin domains in a particular orientation. Table 1 compares the dielectric properties of TGG crystals with values for high quality crystals from the literature.

Figure 4 shows the saturation polarization, P_{sat}, from pyroelectric measurements as a function of temperature. A smooth parabolic line would be expected, but the measurement of polarization from pyroelectric data is highly dependent on heating rate. In the experimental setup that was used, it was difficult to achieve a steady state heating rate, which could have lead to the wavy nature of the curve shown in Figure 4. However, the distinct transition in the curve, confirms that the Curie transition of TGG grown $BaTiO_3$ crystals is of the first order and is approximately 133°C. The result shown in Figure 4 is that the room temperature P_{sat} is approximately 19 μC/cm^2. This value is lower than the expected value of 26 μC/cm^2 for $BaTiO_3$ single crystals.[14-16] The fact that the saturation polarization only reaches ~73% of the spontaneous polarization is an indicator that not all the domains were aligned by application of an electric field. As mentioned before, some portion of domains are pinned by defects associated with the pores. However this polarization value is still much higher than for ceramics (i.e. randomly oriented polycrystalline structures) of similar composition (8 μC/cm^2).[15]

(2) Effect of Electric Field

Figure 5 shows the bipolar polarization and strain behavior along [001] as a function of electric field at 10 Hz. The first aspect to notice is that the polarization loop is not as square as expected for a single crystal. The remanent polarization, P_R is approximately 12 $\mu C/cm^2$ (versus 26 $\mu C/cm^2$ for fully dense single crystals of $BaTiO_3$.[15,16] The coercive field, E_C is approximately 3 kV/cm. This is higher than for Remeika or TSSG $BaTiO_3$ single crystals, which exhibit a $E_C \sim 1$ kV/cm. It is well known that structural defects such as pores in the material tend to impede the motion of domain walls and therefore increase the electric field necessary to orient affected domains. In the TGG crystals a relatively large fraction of the original matrix porosity is entrapped in the crystal. It is believed that these pores impede the motion of domains, resulting in a higher coercive field. These same defects may also influence the remanent polarization characteristics, also by pinning domain walls. Again, the values for P_R and E_C are intermediate between those of other single crystals and ceramics of similar composition. The strain behavior exhibits typical butterfly loops. Neither the polarization nor the strain curves saturate over the electric field range measured, therefore higher field measurements were necessary to attempt to achieve a single domain state.

Figure 6 shows the unipolar polarization and strain behavior along [001] as a function of electric field. In an attempt to observe fully saturated polarization and strain behavior, an electric field was applied until breakdown of the sample occurred. The sample had a breakdown strength of 105 kV/cm and the data just prior to breakdown is shown in Figure 6a. Because the sample did not reach full saturation during the bipolar measurements, unipolar measurements at the highest fields were conducted and then the starting polarization value normalized to the bipolar data at lower electric fields. The crystal was able to withstand the higher field using unipolar field and very close to a single domain state was achieved. As shown in Figure 6a, the crystal shows a remanent polarization of approximately 16 $\mu C/cm^2$. By extrapolating the curve back to a low field state however, it is shown that under these conditions the crystal has a saturation polarization, P_{sat} of approximately 21.5 $\mu C/cm^2$, which much more closely approaches the value of TSSG single crystals of $BaTiO_3$ than does the data from bipolar measurements. This is approximately 83% of the single domain value and is also in close agreement with the saturation polarization value of 19 $\mu C/cm^2$ found from pyroelectric measurements (Figure 4).

The unipolar strain versus electric field is shown in Figure 6b. From this curve, significant domain reorientation is observed at fields up to 65-75 kV/cm, above which the strain behavior begins to saturate. As mentioned previously, above 100 kV/cm the sample exhibits close to a single domain state. By calculating the slope in the saturated high field region the piezoelectric coefficient, d_{33} was found to be ~140 pC/N. This agrees well with previous reports for single domain $BaTiO_3$ single crystals.[17] A summary of polarization, coercive field, and piezoelectric coefficients calculated from the polarization measurements are presented in Table 2.

The polarization and strain behavior of TGG grown crystals were also measured for crystals grown from {111} and {110} template orientations. Figure 7 shows the bipolar polarization and unipolar strain behavior for a {111} grown crystal oriented along [111] as a function of electric field. Although the bipolar polarization loop is more square than for [001] oriented crystals, it is still not as square as expected for a single crystal. The remanent polarization, P_R is approximately 8 $\mu C/cm^2$. Since the polar direction is along [001] the [111] P_r value should be multiplied by $\sqrt{3}$ to get the P_r along [001], which is 14 $\mu C/cm^2$ (versus 26 $\mu C/cm^2$ for fully dense single crystals of $BaTiO_3$[15,16]). The coercive field, E_C is approximately 3 kV/cm. The unipolar strain versus electric field is shown in Figure 7b. From this curve, significant domain reorientation is observed at fields up to 10 kV/cm, above which the strain behavior begins to saturate. By calculating the slope in the saturated region, the piezoelectric coefficient, d_{33} was found to be ~260 pC/N. The values for a [110] oriented crystal grown from a {110} oriented template were as follows: $P_r \sim 3.4$ $\mu C/cm^2$, $E_c \sim 1.2$ kV/cm.

(3) *Electromechanical Coupling, Piezoelectric and Elastic Properties*

Figure 8 shows the electromechanical coupling coefficients, k_{33} and k_{31} as a function of DC bias. The observed increase in coupling coefficients with DC bias is consistent with the observation that as-poled crystals had low remanent polarization. The value increases from 0.42 at 0 kV/cm DC bias to 0.51 at ~2 kV/cm. It seems likely that the value would converge towards the value previously reported for single crystals (0.56)[15] at higher bias values. Figure 8b shows the transverse electromechanical coupling coefficient as a function of DC bias. As in the case for the longitudinal coupling coefficient, an increase in magnitude with increasing DC bias is observed. The maximum value of k_{31} was 0.18, which is significantly lower than the expected value of 0.32 for fully poled crystals.[15,18] The magnitude of the electromechanical coupling coefficients is influenced by the presence of voids, because these macro-defects can impede domain wall motion. The resulting difficulty in fully poling these crystals results in lower observed electromechanical coupling coefficients. There is also sample to sample variability in the ability to achieve a well poled state, which probably accounts for the low k_{31} values relative to the observed k_{33}. This is similar to what was observed for the polarization behavior, where high fields (100 kV/cm) are needed to approach a single domain state. Because the samples partially depole with removal of the field, the domain state is not stable, resulting in low electromechanical coupling coefficients even after poling at high fields.

Many material constants can be calculated by using the electromechanical coupling coefficients in conjunction with dielectric constant data. The formulas for each calculation are listed below:[15]

$$\frac{1}{S_{11}^{E}} = 4\rho f_R^2 l^2 \qquad S_{11}^{D} = S_{11}^{E}\left(1 - k_{31}^{2}\right) \qquad d_{31} = k_{31}\sqrt{\varepsilon_{33}^{T} S_{11}^{E}} \qquad g_{31} = d_{31}/\varepsilon_{33}^{T}$$

$$S_{33}^E = S_{33}^D/\left(1-k_{33}^2\right) \qquad \frac{1}{S_{33}^D} = 4\rho f_A^2 l^2 \qquad d_{33} = k_{33}\sqrt{\varepsilon_{33}^T S_{33}^E} \qquad g_{33} = d_{33}/\varepsilon_{33}^T$$

where ρ is the density of the sample (97% ~ 5.84 g/cm^3), f_a and f_r are the anti-resonant and resonant frequencies, respectively and l is the sample length. The calculated values for these constants are shown in Table 3. For elastic compliances, S_{ij}^D (open circuited sample) and S_{ij}^E (close circuited sample), measured from longitudinal properties (S_{33}^D) the value is higher than expected. The effect of porosity on these values was calculated using mixing rules and it was found that as volume percent porosity increases, Young's modulus decreases and hence compliance increases.[19] However, the amount of increase cannot sufficiently account for the total increase in the values shown in Table 3. Therefore, the increase in the values must be associated with the lower electromechanical coupling coefficients and higher values for the dielectric constant which lead to errors in the calculated values. The calculated piezoelectric coefficient, d_{33} has a value of approximately 135 pC/N and any errors from the calculation of this value should cancel out. This is in good agreement with the value calculated from high field polarization data (Figure 6). The piezoelectric coefficient, g_{33} was calculated to be 30.6 Vm/N as compared to 57.5 for fully poled $BaTiO_3$ single crystals. The g_{33} coefficient is associated with the production of voltage in response to a mechanical stress, and it's value is primarily lower because of the higher value of ε_{33}^T. The piezoelectric coefficients, d_{31} and g_{31} measured from transverse properties show similar results to that of the longitudinal results with values lower than expected. The elastic compliances, however match literature values closely.

IV. Conclusions

Single crystals of $BaTiO_3$ were grown by TGG and the dielectric properties and crystal quality were evaluated and compared to high quality TSSG crystals as cited in the literature. The largest effect of porosity on the TGG crystals was difficulty in poling the crystals even under high fields (100 kV/cm), which decreases the electromechanical coupling efficiency. A majority of the experimental data closely matches the literature values, indicating that pores do not affect the electronic properties to a degree that they could not be used in devices. It is likely that the properties of these crystals may be improved further by eliminating the porosity from the crystals.

Acknowledgements

Financial support from the Defense Advanced Research Projects Agency on AFSOR Grant No. F49620-94-1-0428, DARPA contract N00014-93-0502, and ONR Grant No. N00014-98-1-0527 is gratefully acknowledged.

References

1) J. P. Remeika, "A Method for Growing Barium Titanate Single Crystals," *J. Am. Ceram. Soc.*, **76** [2] 940-1 (1954).

2) F. Brown and W. H. Todt, "Floating-Zone $BaTiO_3$: Preparation and Properties," *J. Appl. Phys.*, **35** [5] 1594-8 (1964).

3) A. Linz, V. Belruss and C. S. Naiman, "Solution-Grown Perovskites," *J. Electrochem. Soc.*, **112** [6] 60C (1965).

4) D. Rytz, B. A. Wechsler, C. C. Nelson and K. W. Kirby, "Top-seeded Solution Growth of $BaTiO_3$, $KNbO_3$, $SrTiO_3$, $Bi_{12}TiO_{20}$ and $La_{2-x}Ba_xCuO_4$," *J. Crystal Growth*, **99** [4-Jan] 864-8 (1990).

5) Y. Tomita, "Technique for Preparation of $BaTiO_3$ Single Crystal," *New Ceram.*, **4** [5] 1-6 (1991).

6) S. Matsuzawa and S. Mase, "Method for Producing a Single Crystal of Ferrite," *U.S. Patent 4339301* (Jul. 13, 1982).

7) M. Imaeda and S. Matsuzawa, "Growth of Yttrium Iron Garnet Single Crystal by Solid-Solid Reaction," *1st Japan International SAMPE Symposium*, 419-24 (Nov. 28-Dec. 1, 1989).

8) T. Yamamoto and T. Sakuma, "Fabrication of Barium Titanate Single Crystals by Solid-State Grain Growth," *J. Am. Ceram. Soc.*, **77** [4] 1107-9 (1994).

9) T. Li, A. M. Scotch, H. M. Chan, M. P. Harmer, S. Park and T. R. Shrout, "Single Crystals of $Pb(Mg_{1/3}Nb_{2/3})O_3$-35 mol% $PbTiO_3$ from Polycrystalline Precursors," *J. Am. Ceram. Soc.*, **81** [1] 244-8 (1998).

10) P. W. Rehrig, G. L. Messing and S. Trolier-McKinstry, "Templated Grain Growth of Barium Titanate Single Crystals," *In Preparation*, (1998).

11) S. H. Wemple, J. M. DiDomenico and I. Camlibel, "Dielectric and Optical Properties of Melt-Grown $BaTiO_3$," *J. Phys. Chem. Solids*, **29** 1797-1803 (1968).

12) K. S. Mazdiyasni and L. M. Brown, "Microstructure and Electrical Properties of Sc_2O_3-Doped Rare-Earth-Oxide-Doped and Undoped $BaTiO_3$," *J. Am. Ceram. Soc.*, **54** 539-43 (1971).

13) S. S. Lopatin and T. G. Lupeiko, "Properties of Porous Piezoelectric Lead Zirconate Titanate Ceramics," *Inorg. Mater.*, **27** [9] 1948-51 (1991).

14) S. H. Wemple, "Polarization Fluctuations and the Optical-Absorption Edge in $BaTiO_3$," *Phys. Review B*, **2** [7] 2679-88 (1970).

15) B. Jaffe, W. R. Cook and H. L. Jaffe, Piezoelectric Ceramics, Vol. 3, *Non-Metallic Solids*, Academic Press Ltd., New York, 1971.

16) F. Jona and G. Shirane, Ferroelectric Crystals, Vol. 1, Dover Publications, New York, 1993.

17) S.-E. Park and S. Wada, "Properties of Engineered Domain State Barium Titanate Single Crystals," *In Preparation*, (1998).

18) M. Zgonik, P. Bernasconi, M. Duelli, R. Schlesser, P. Günter, M. H. Garrett, D. Rytz, Y. Zhu and X. Wu, "Dielectric, Elastic, Piezoelectric, Electro-optic, and Elasto-optic Tensors of $BaTiO_3$ Crystals," *Physical Review B*, **50** [9] 5941-8 (1994).

19) W. D. Kingery, H. K. Bowen and D. R. Uhlmann, pp. 208, 364, 776 in Introduction to Ceramics, Vol. 2nd., John Wiley & Sons, New York, 1976.

List of Figures

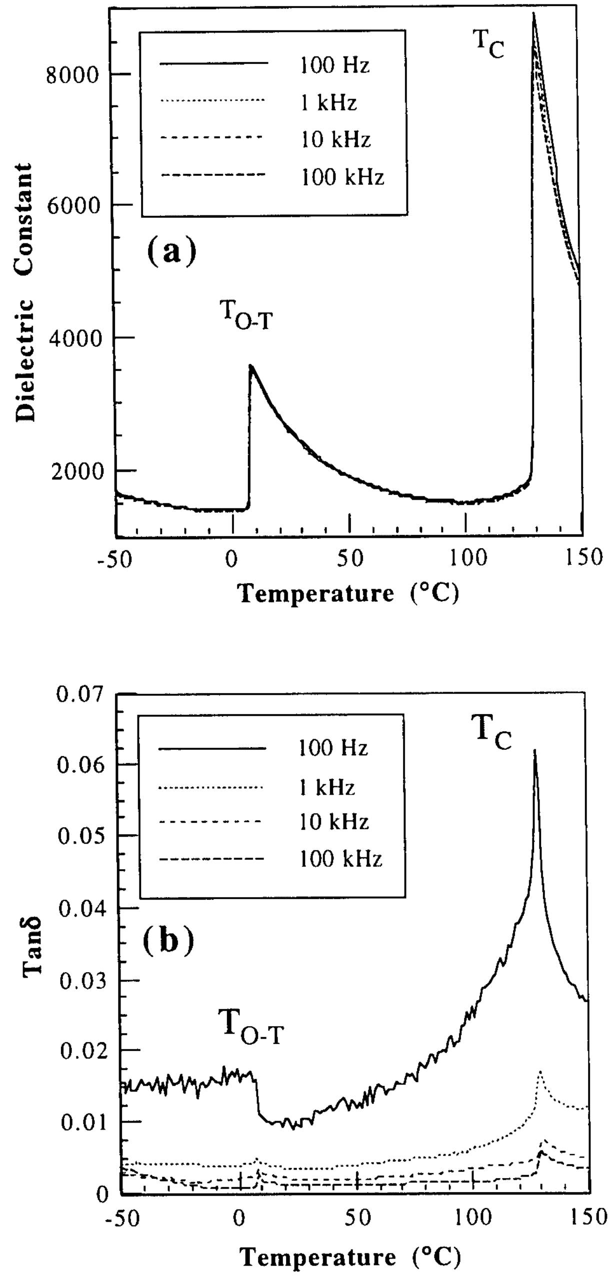

Fig. 1 Dielectric constant (a) and dielectric loss (b) as a function of temperature and frequency for TGG grown $BaTiO_3$ single crystal measured in one of the pseudocubic <100> directions. ($T_{R\text{-}O}$ = rhombohedral to orthorhombic transition, $T_{O\text{-}T}$ = orthorhombic to tetragonal transition, T_C = Curie temperature)

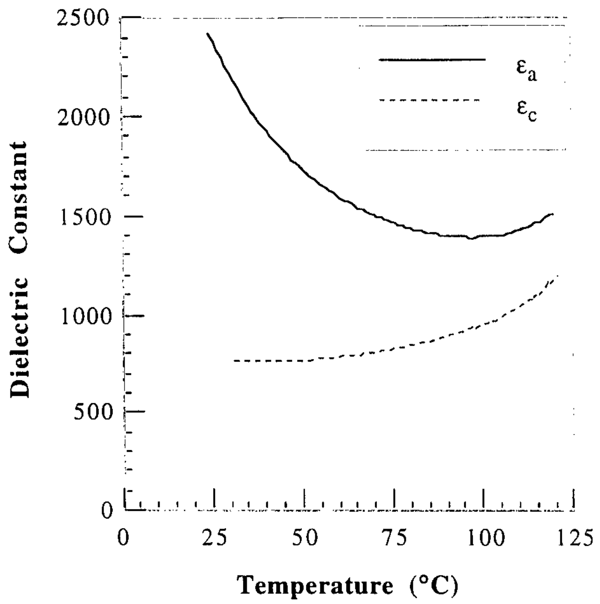

Fig. 2 Dielectric constant (1 kHz) along the *a* (ε_a) and *c* (ε_c) axes in the tetragonal phase as a function of temperature for TGG grown $BaTiO_3$ single crystal.

Table 1 Summary and comparison of dielectric properties of TGG single crystal of $BaTiO_3$ and single crystals prepared by TSSG as reported in the literature.

Property (RT, 1 kHz)	Reported Value (single domain)[†]	TGG Crystal
ε_a	3600	2430
Tanδ (a-axis)	<0.01	0.005
ε_c	135	770
Tanδ (c-axis)	<0.01	0.009
ε_{33}^T	135	263 (DC bias)
Tanδ	<0.01	0.003
T_C (°C)	135	132
C (°C)	1.8×10^5	1.8×10^5
T_0 (°C)	112	112

[†] S. H. Wemple, *et al.*, J. Phys. Chem. Solids **29**, 1797-1803 (1968) and S. H. Wemple, Phys. Rev. B **2** [7] 2679-89 (1970)

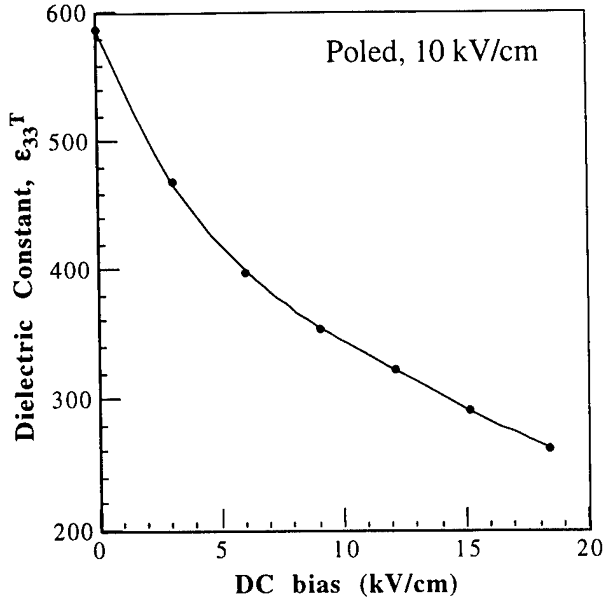

Fig. 3 Dielectric constant, ε_{33}^T, as a function of DC bias for TGG grown $BaTiO_3$ single crystal.

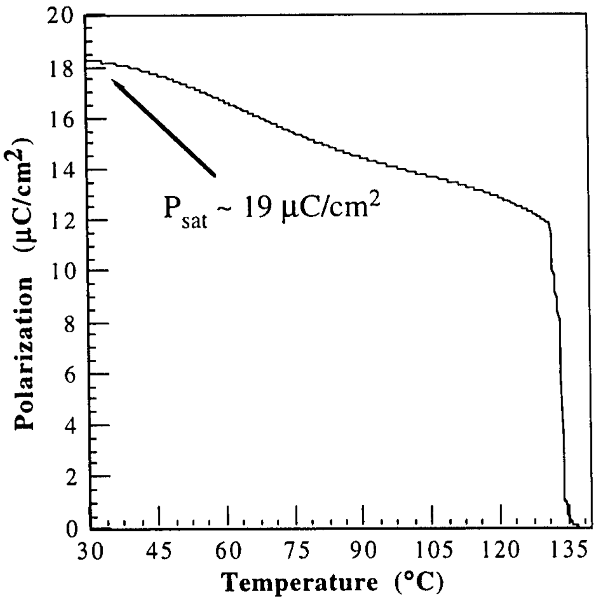

Fig. 4 Saturation polarization as a function of temperature for TGG grown $BaTiO_3$ single crystal.

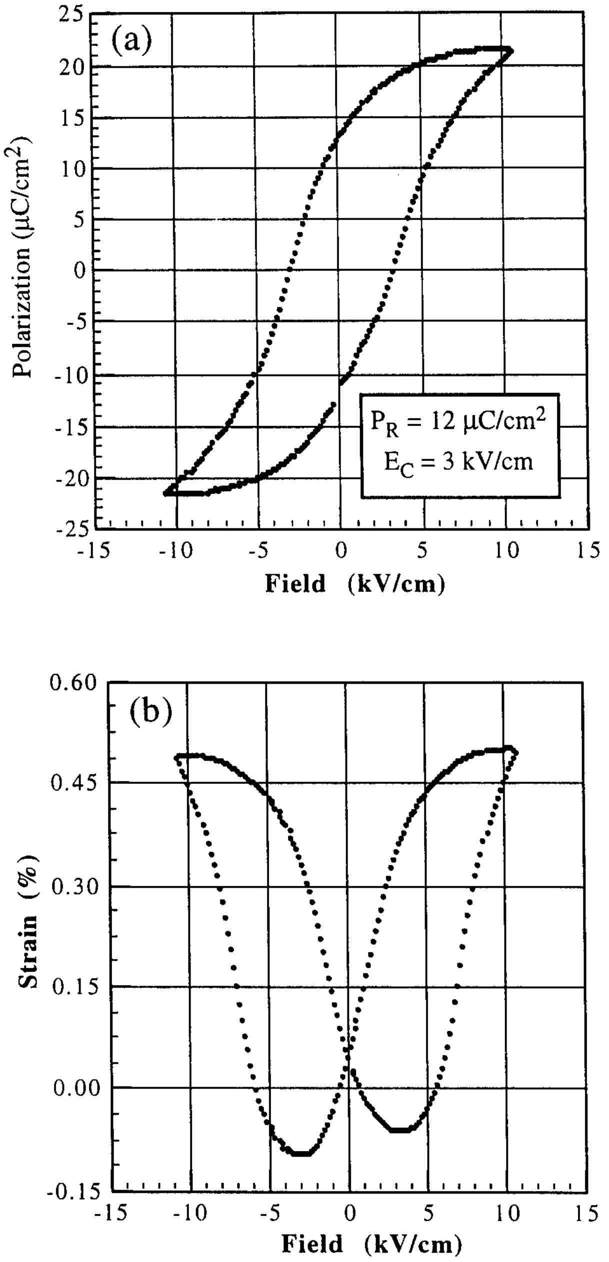

Fig. 5 Bipolar polarization (a) and strain (b) as a function of electric field for TGG grown $BaTiO_3$ single crystal.

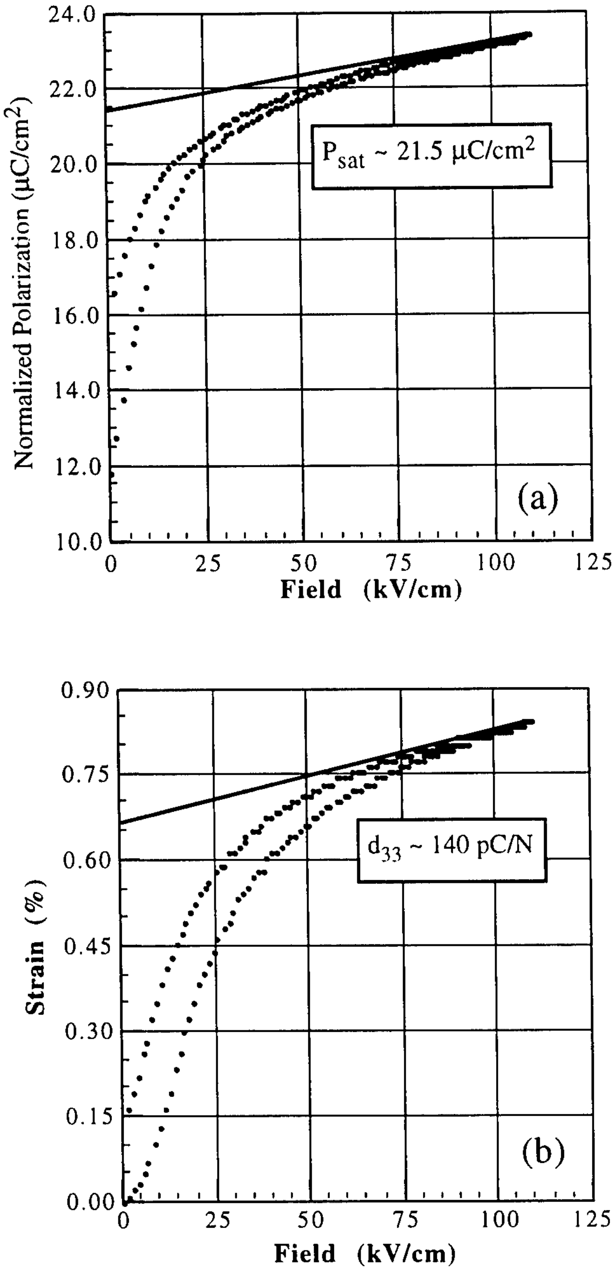

Fig. 6 Unipolar polarization (a) and strain (b) as a function of electric field at high applied electric fields for TGG grown $BaTiO_3$ single crystal.

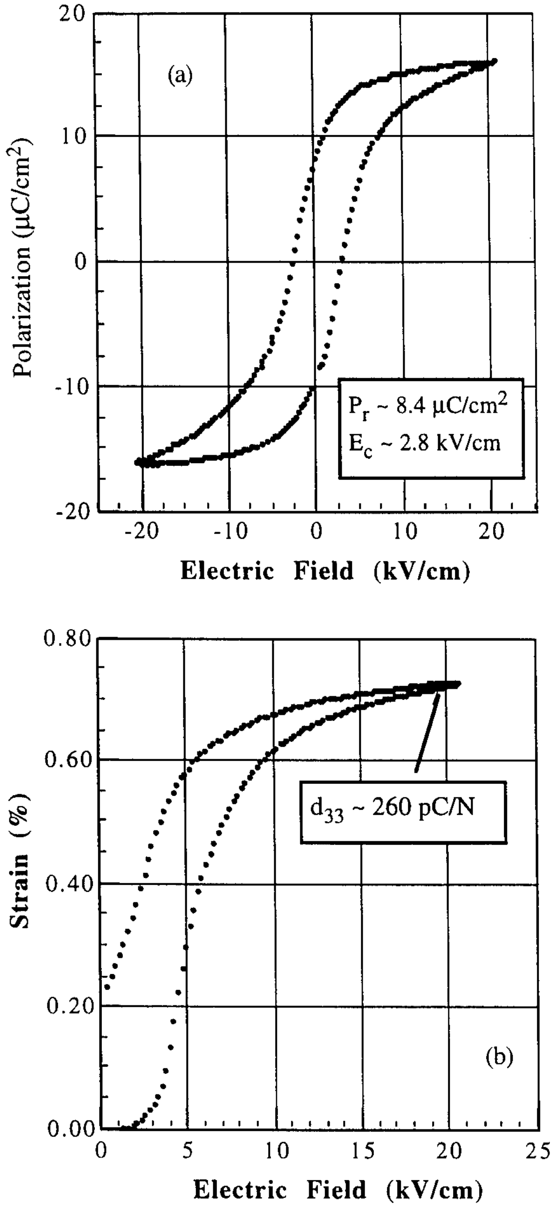

Fig. 7 Bipolar polarization (a) and unipolar strain (b) as a function of electric field for TGG grown $BaTiO_3$ single crystal from a {111} oriented template crystal.

Table 2 Summary of polarization properties of TGG single crystal of $BaTiO_3$.

Property	Reported Value (single domain)	TGG Crystal
P_r ($\mu C/cm^2$)	26[§]	12
P_{sat} ($\mu C/cm^2$)	26[§]	21.5
P_{sat} (pyro) ($\mu C/cm^2$)	26[†]	19
E_c (kV/cm)	~1[§]	3
d_{33} (pC/N)	85.6[§], 140[*]	140

[†] S. H. Wemple, Phys. Review B 2 [7] 2679-89 (1970)

§ Jaffe, Cook and Jaffe, Piezoelectric Ceramics, Academic Press Ltd. (1971)

* S.-E. Park and S. Wada, Personal Communication, (1998)

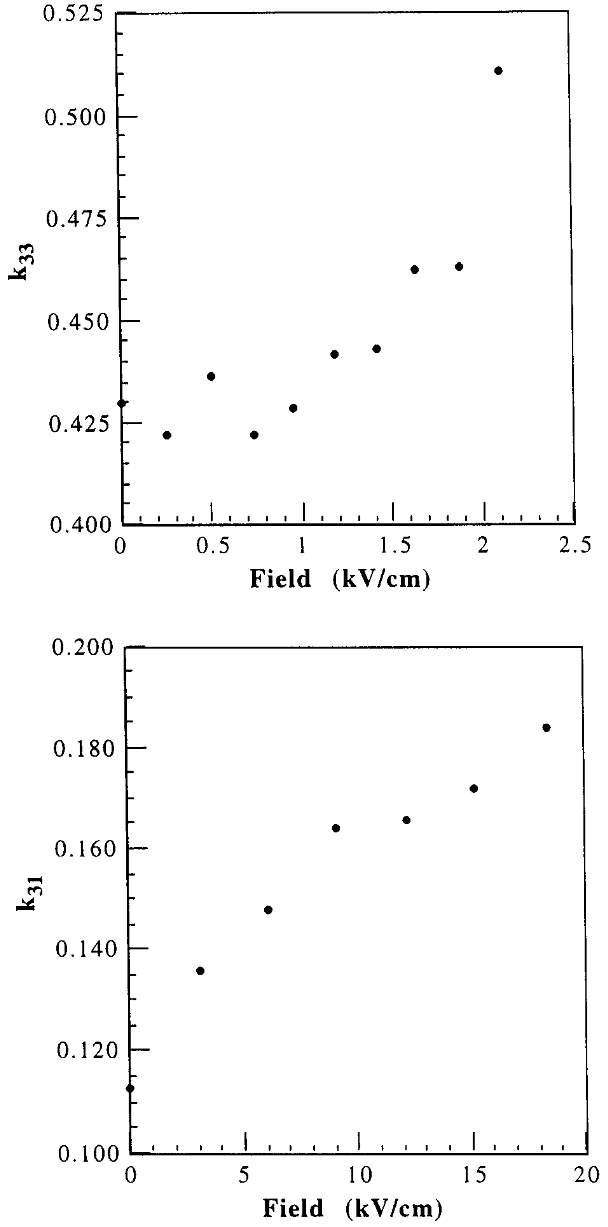

Fig. 8 Electromechanical coupling coefficients, k_{33} (a) and k_{31} (b), as a function of DC bias for TGG grown $BaTiO_3$ single crystal.

Table 3 Summary of piezoelectric, electromechanical and elastic compliance properties of TGG single crystal of $BaTiO_3$.

Property	Reported Value[§] (single domain)	TGG Crystal
k_{33}	0.56	0.51
S_{33}^{D} (10^{-12} m^2/N)	10.8	13.2
S_{33}^{E} (10^{-12} m^2/N)	15.7	17.8
d_{33} (pC/N)	140[*]	135
g_{33} (10^{-3} Vm/N)	57.5	30.6
k_{31}	0.315	0.18
S_{11}^{D} (10^{-12} m^2/N)	7.25	8.1
S_{11}^{E} (10^{-12} m^2/N)	8.05	8.4
d_{31} (pC/N)	-34.5	-26
g_{31} (10^{-3} Vm/N)	-23.0	-9.8

[§] B. Jaffe, W. R. Cook, and H. L. Jaffe, Piezoelectric Ceramics 49-114 (1971)

[*] S.-E. Park and S. Wada, Personal Communication, (1998)

APPENDIX C

PIEZOELECTRIC PROPERTIES OF ZIRCONIUM-DOPED BARIUM TITANATE SINGLE CRYSTALS GROWN BY TEMPLATED GRAIN GROWTH

Paul W. Rehrig,* Seung-Eek Park,* Susan Trolier-McKinstry,* and Gary L. Messing*
Beth Jones, Thomas R. Shrout*

Materials Research Laboratory, The Pennsylvania State University, University Park, Pennsylvania 16802

Single crystals of $Ba(Zr_xTi_{1-x})O_3$ were grown by templated grain growth (TGG). Millimeter size single crystals of $Ba(Zr_xTi_{1-x})O_3$ were produced by heating a $BaTiO_3$ crystal in contact with a sintered polycrystalline matrix of 4.5, 5.0 or 8.5 mol% Zr-doped barium titanate for 30 hours at 1350°C. To facilitate boundary migration, the ceramic compact was made 3 mol% TiO_2 excess. The 4.5 and 5.0 mol% Zr-doped crystals were orthorhombic at room temperature, and for a pseudocubic (001) orientation, they showed remanent polarizations of 13 $\mu C/cm^2$ and a high field d_{33} of 340-355 pC/N. The 8.5 mol% Zr-doped crystal (again oriented along the pseudocubic (001)) was rhombohedral at room temperature with a remanent polarization of 10 $\mu C/cm^2$. A k_{33} value of 0.74 from resonance measurements was observed for the 4.5 mol% Zr-doped crystal.

Based in part on the thesis submitted by Paul W. Rehrig for the Ph.D. degree in Materials Science and Engineering, Pennsylvania State University, University Park, PA 1998.

[*] Membership in the American Ceramic Society

I. Introduction

Ultrahigh electrically-induced strain levels (up to 1.7 %) were recently discovered in lead-based relaxor ferroelectric single crystals.[1] The composition of these perovskite crystals lies near a morphotropic phase boundary (MPB) between tetragonal and rhombohedral phases. It was found that lead zinc niobate – lead titanate and lead magnesium niobate – lead titanate rhombohedral crystals oriented and poled along the pseudocubic [001] axis had an enhanced piezoelectric response compared to [111] oriented crystals (which is the polar axis direction), which was related to an engineered domain state.[1,2] These enormous strain levels, coupled with the large piezoelectric constants and electromechanical coupling coefficients are extremely attractive for a variety of sensor and actuator applications. Another important result of the engineered domain state is a low level of hysteresis in the strain, at least to strain levels on the order of 0.6%. This is believed to be due to the fact that the four domain states in a poled crystal are equally favored by an applied electric field, so that there is no driving force for extensive domain wall motion. Hence, the question arises, "Is this concept of engineered domain state applicable to other ferroelectric crystals?"

Initial work on $BaTiO_3$ indicates that the concept of an engineered domain state can be applied to this system as well.[3] Piezoelectric coefficient, d_{33}, values up to 420 pC/N and 300 pC/N observed in orthorhombic (0°C) and rhombohedral (-100°C) crystals poled along the pseudocubic [001], appreciably higher than those measured for the tetragonal phase at room temperature (~125 pC/N), are the result of crystallographic engineering. This suggests that improved piezoelectric properties can be achieved in non-lead based perovskite crystals if the orthorhombic or rhombohedral phase is shifted to room temperature.

It is well known that the phase transition temperatures in $BaTiO_3$ can be altered by doping with either A or B-site substitutions.[4] Zirconium is one element that pinches the transition temperatures so that the rhombohedral-orthorhombic and orthorhombic-tetragonal phase transition temperatures are raised while the Curie temperature is lowered.[4-6] By varying the amount of dopant it is possible to stabilize either the rhombohedral and orthorhombic phases at room temperature.[5,6] In this work Zr-doped $BaTiO_3$ crystals were produced and the properties of resultant crystals poled along the pseudocubic [001] direction were investigated.

Preparation of single crystals is difficult and time-consuming for many systems, including $BaTiO_3$. In this work, templated grain growth was used to produce crystals with Zr concentrations between 4.5 and 8.5 mol% for rapid assessment of crystals of varying composition. This chapter describes the synthesis and piezoelectric properties of Zr-doped $BaTiO_3$ single crystals grown by TGG.

II. Experimental Procedure

Single crystal $BaTiO_3$ cut-offs (Lockheed Sanders Inc., Nashua, NH) were used as template crystals for TGG. The orientation of the crystals was determined by four-circle X-ray or backscattered X-ray Laue techniques. The crystals were sectioned along {001} faces using a diamond saw to sizes in the range of a few mm in size × 0.3 mm thick. One side of the template was polished with 1 μm diamond paste.

In prior research, it was demonstrated that $BaTiO_3$ crystals could be grown using TGG at 1350°C, above the eutectic temperature, with a Ti-rich initial powder.[11] This resulted in the formation of a liquid phase at the growth temperature that was found to accelerate the growth process. Therefore, a titanium-rich $BaTiO_3$ powder with a proper amount of Zr was used for TGG. The powder was obtained by mixing $BaCO_3$ (0.1 μm, Sakai Chemical Co., Sakai, Japan), TiO_2 (0.5 μm, Ishihara Chemical Co., Kobe, Japan), and ZrO_2 (0.05 μm, TAM Ceramics Inc., Niagara Falls, NY) powders in a Nalgene bottle with an aqueous dispersant (Tamol, T963), and high density ZrO_2 media at a pH of 10 in DI-H_2O. The slurry was milled overnight and then dried in a Pyrex pan. The powder was calcined in O_2 at 1150°C for 4 h, followed by further heating in air at 1200°C for 2 h. The final powder was attrition milled for 16 h and then sieved to less than 45 μm (-325 mesh) prior to being mixed with an organic binder (Acryloid B-7 MEK, Rohm & Haas, Philadelphia, PA). Pellets were pressed uniaxially at 140 MPa followed by cold isostatic pressing at 276 MPa and sintering at 1300°C- 1350°C for 2 h in air. The grain size of the 4.5 and 5.0 mol% Zr-doped $BaTiO_3$ sintered ceramics was ~15 μm and the samples were approximately 98% of theoretical density. The grain size of the 8.5 mol% Zr-doped $BaTiO_3$ sintered ceramics was ~25 μm and the sample was approximately 92% of theoretical density. One side of the sintered polycrystalline matrix was polished with 1 μm diamond paste.

For TGG, a {100} surface of the $BaTiO_3$ crystal was contacted, without pressure, with the sintered polycrystalline matrix and the assemblage was heated in air to 1350°C for 8 to 30 h. Cross sections of the growing crystal in the polycrystalline matrix were examined by scanning electron microscopy (SEM) (ISI Model DS 130) after polishing to 1 μm diamond paste and then thermal etching at 1300°C for 30 min.

Grown crystals were sectioned from the template and polycrystalline matrix so that dielectric measurements were performed on the grown crystals alone (i.e. none of the original $BaTiO_3$ crystal remained). The pseudocubic {001} faces of grown crystals were oriented via X-ray Laue techniques and polished with 1 μm diamond paste followed by gold-sputtering to form electrodes. A multifrequency meter (HP 4284A LCR meter) was used in conjunction with a computer controlled temperature chamber (Delta Design Inc., Model MK 9023) to measure the dielectric constant as a function of temperature on cooling (175°C to -100°C) at frequencies between 100 Hz and 100 kHz. Samples were poled either by field cooling (10 kV/cm) from temperatures above the dielectric maximum temperature (T_{max}) or by applying 40 kV/cm at room temperature. High field measurements (1-50 kV/cm) included simultaneous polarization (P) and strain (S) hysteresis curves obtained using a computer-controlled modified Sawyer Tower system and a linear variable displacement transducer (LVDT) sensor driven by a lock in amplifier (Stanford Research Systems, Model SR830). The voltage was supplied using either a Trek 609C-6 high voltage DC amplifier or a Kepco BOP 1000M amplifier. The same system was used to measure unipolar strain curves on poled crystals oriented along the pseudocubic ⟨001⟩. The value for d_{33} was estimated from the slope of the unipolar strain vs. electric field (E) curve. Electromechanical coupling was measured using the IEEE resonance technique (ANSI/IEEE Std. 176-1978) on samples poled by field cooling above the Curie temperature and 10 kV/cm.

III. Results and Discussion

Figure 1 shows a scanning electron micrograph of a cross-sectional view of the $Ba(Zr_{0.05}Ti_{0.95})O_3$ crystal (BZT-O5.0), the template crystal, and the polycrystalline matrix after 30 h at 1350°C. The boundary migrated as much as 825 μm into the polycrystalline matrix. Note that the crystal growth front is no longer parallel to the initial template surface, but has grown to a habit plane, as was shown previously for growth into pure $BaTiO_3$ matrices.[9,11] The grown crystal also incorporated approximately 2 vol% of the matrix porosity. The average growth rate from a $\langle 001 \rangle$ oriented template crystal after 30 h was 28 μm/h. However, the initial growth rate may have been faster when the matrix grain size was 15 μm. The final matrix grain size was 22 ± 17 μm, with a significant number (~10-15 vol%) with a grain size > 40 μm. Coarsening of matrix grains is known to decrease the driving force associated with boundary migration during TGG. As indicated by the variable porosity entrapped in the crystal, the rate of growth continuously decreased with time. In the top layer of the grown crystal the pores remain abundant and ~ 5-10 μm in size. After the growth rate slowed, fewer pores are trapped and those that remain coalesced before entrapment.

Figure 2 shows the dielectric constant (a) and dielectric loss (b) as a function of temperature and mol% zirconium at 1 kHz. The samples showed very little dispersion as a function of frequency and therefore only the 1kHz values are shown. As seen in polycrystalline Zr-doped $BaTiO_3$, the transition temperatures are pinched with increasing mol% zirconium.[4-6,12] The 4.5 (BZT-O4.5) and 5.0 (BZT-O5.0) mol% Zr samples show distinct transition temperatures with both the rhombohedral-orthorhombic and orthorhombic-tetragonal transition temperatures shifted up by approximately 80°C ($T_{R\text{-}O}$

= 0°C) and 45°C (T_{O-T} = 50°C), respectively. The amount of shift is similar to the amount of shift (75 and 49°C, respectively) predicted by Jaffe *et al.*[4] for these compositions. The result of this shift is that the orthorhombic phase is stabilized at room temperature. The Curie temperature for the 4.5 and 5.0 mol% Zr samples shifted down by approximately 20°C (T_C = 110°C), also similar to the shift (21°C) shown by Jaffe *et al.*[4] The room temperature dielectric constants are approximately 3200 and 3500 for unpoled BZT-O4.5 and BZT-O5.0, respectively. The room temperature dielectric loss is approximately 0.013- 0.016 for both materials. What is also important to note, as clearly observed in Figure 2, is the effect of a small change of 0.5 mol% Zr doping on the pinching behavior. This shows that the small change in matrix composition was reflected in the grown crystal. Above the dielectric maximum temperature, T_{max}, the Curie-Weiss law is obeyed with Curie constants and Curie-Weiss temperatures of 1.4 x 10^{5}°C and 104°C for BZT-O4.5 and 1.3 x 10^{5}°C and 102°C for BZT-O5.0, respectively; i.e. $\varepsilon_{R(BZT-04.5)} = 1.4 \times 10^{5^{\circ}} C/(T - 104^{\circ} C)$ and $\varepsilon_{R(BZT-05.0)} = 1.3 \times 10^{5^{\circ}} C/(T - 102^{\circ} C)$.

Figure 3 shows the dielectric constant as a function of temperature and frequency for the crystal with 8.5 (BZT-R8.5) mol% Zr. The room temperature dielectric loss was ~0.05. The dielectric response is pinched even more than for BZT-O4.5 and BZT-O5.0 and the transition behaviors are more diffuse. The rhombohedral-orthorhombic and orthorhombic-tetragonal transition temperatures shifted up by 135°C (T_{R-O} = 55°C) and 65°C (T_{O-T} = 70°C), respectively. The rhombohedral phase is stabilized at room temperature as a result of these shifts. T_{max} is shifted down by approximately 43°C (T_{max} = 90°C). These shifts in temperature are also similar to the shifts (106°C, 59°C, and 40°C, respectively) given by Jaffe, Cook, and Jaffe.[4]

Figure 4 shows the polarization and strain behavior for BZT-O4.5 and BZT-O5.0 crystals oriented along the pseudocubic ⟨001⟩ as a function of electric field at room temperature. Orthorhombic BZT-O4.5 and BZT-O5.0 crystals have remanent polarizations (P_r) and coercive fields (E_c) of approximately 13 μC/cm^2 and 1 kV/cm, respectively. The coercive field is lower and remanent polarizations higher[5,12] than reported for ceramics with similar composition, which is expected for a single crystal of this orientation. In the orthorhombic phase, the polarization vector is oriented along the pseudocubic <110> direction, the magnitude of this vector is obtained by multiplying the P_r value from Figure 4 with √2, which results in a value of 18 μC/cm^2.

For the Zr-doped crystals measured here, an engineered domain state with macrosymmetry 4mm is expected for poling along the pseudocubic ⟨001⟩ axis, similar to the case of rhombohedral relaxor-PT crystals[1]. As shown in Figure 4a, the top of the hysteresis loop is more rounded than in the case of relaxor-PT crystals. This indicates that the crystal partially depoles near zero field. The stability of the domain state was not studied.

Figure 5 shows the unipolar strain behavior at room temperature for BZT-O4.5 and BZT-O5.0 crystals poled and excited along the pseudocubic ⟨001⟩ as a function of electric field. Both crystals show maximum strain levels of approximately 0.48% at a maximum field of ~60 kV/cm, which includes ~0.35% strain associated with domain reorientation. After saturation, the strain behavior from 30-60 kV/cm corresponds to a d_{33} of 355 and 340 pC/N for BZT-O4.5 and BZT-O5.0, respectively.

Figure 6 shows the polarization and strain behavior for ⟨001⟩ oriented BZT-R8.5 as a function of electric field at room temperature. The larger hysteresis in the P vs. E curve (Figure 6a) relative to that for the orthorhombic crystals may be a result of inferior crystal quality, i.e. a greater volume of pores (BZT-R8.5 ~ 8 vol%, BZT-O4.5 ~ 2 vol%) and/or a higher space charge contribution to the dielectric displacement. Although P_r ~ 10 $\mu C/cm^2$ in Figure 6a, the top of the hysteresis loop is more rounded than for orthorhombic crystals. In the rhombohedral phase, the polarization vector is oriented along the pseudocubic <111> direction, the magnitude of this vector is obtained by multiplying the P_r value from Figure 6 with $\sqrt{3}$, which results in a value of 17 $\mu C/cm^2$.

The unipolar strain behavior at room temperature for a ⟨001⟩ poled rhombohedral crystal is shown in Figure 7. d_{33} calculated from the slopes of unipolar strain vs. E curves were a function of electric field, i.e. d_{33} became a maximum (~480 pC/N) at ~ 10 kV/cm, but decreases and subsequently saturates to 160 pC/N at E > 30 kV/cm. The high initial value is due, at least in part, to domain reorientation. Beyond that point, as an electric field along ⟨001⟩ prefers the tetragonal polar phase, it is possible that a modest bias field results in the transition from rhombohedral to tetragonal phase. It is noteworthy to mention that the high field d_{33} ~ 160 pC/N is similar to that of a single domain tetragonal $BaTiO_3$ crystal. This field-induced phase transition may be ascribed to the pinching effect, that is, the consequent decrease in free energy difference among polymorphic rhombohedral, orthorhombic, tetragonal, and cubic phases.

The electromechanical coupling data for 4.5 mol% Zr-doped orthorhombic $BaTiO_3$ single crystal (BZT-O4.5) grown by TGG is shown in Table 1. After poling, no resonance was observed for electromechanical coupling measurements. Under application of a 950V DC bias during the measurement the values as shown in Table 1 were obtained, showing k_{33} and d_{33} values of 0.74 and 340 pC/N, respectively. During removal of the field the values remained essentially constant down to 200V (1.0 kV/cm), also shown in Table 1. However, upon removal of all electric field, once again no resonance was detected after a few seconds. Therefore is was necessary to apply a DC bias to stabilize a domain state. The value for d_{33} is in close agreement with the value for d_{33} determined by unipolar strain data. The values for the dielectric constant and elastic compliances, S_{ij}^{D} (open circuited sample) and S_{ij}^{E} (close circuited sample), are higher than found for pure $BaTiO_3$ single crystals.

IV. Conclusions

In this work, single crystals of Zr-doped $BaTiO_3$ were prepared using TGG for 30 h at 1350°C. It is encouraging that TGG can be applied even in doped systems, so that the composition of the grown crystal has the same composition as the ceramic matrix. Room temperature orthorhombic (BZT-O4.5, BZT-O5.0) and rhombohedral (BZT-R8.5) crystals were successfully stabilized using 4.5-5.0 and 8.5 mol% Zr, respectively. Orthorhombic crystals exhibited a room temperature dielectric constant and dielectric loss of approximately 3500 and 0.01, as well as a remanent polarizations and coercive fields of 13 $\mu C/cm^2$ and 1 kV/cm, respectively. High field d_{33} values up to 355 pC/N were observed. This value was supported by resonance measurements, where a d_{33} value of 340 pC/N was observed. A k_{33} value of 0.74 was obtained under DC bias. The d_{33} and k_{33} values calculated for BZT-O4.5 (340-355 pC/N and 0.74, respectively) are almost twice the value of most non-lead materials with similar T_{max} and approaching polycrystalline PZT-5A's (DOD-type II).[1] Although the maximum d_{33}, as high as 480 pC/N (calculated from the S vs. E curves) for BZT-R8.5 is observed at low electric field due to domain reorientation, under additional increase in bias, the rhombohedral phase is probably converted to tetragonal due to the small energy difference between the two associated with the pinching effect. When the orthorhombic or rhombohedral phase is stabilized to room temperature to utilize crystallographic engineering for piezoelectric performance enhancement, the phase relationships and T_{max} must be properly engineered to ensure phase stability, i.e. due to the field-induced phase transition in the rhombohedral crystals the high field measurements (field induced tetragonal phase) may not correlate well with low field measurements (rhombohedral phase). Both BZT-O and BZT-R samples show high piezoelectric coefficients and an improvement in piezoelectric properties over what is currently available for non-lead systems, as a result of crystallographic engineering.

It is possible that the properties of these crystals may be improved further. In particular, better understanding of the role of crystal orientation and phase relationships on the stability of the domain state is necessary and could lead to improved composition selection. In addition, it is possible that eliminating the porosity from the crystals would result in improved electromechanical properties.

Acknowledgement: Financial support from the Defense Advanced Research Projects Agency on AFSOR Grant No. F49620-94-1-0428 and on ONR Grant No. N00014-98-1-0527 are gratefully acknowledged.

References

1) S.-E. Park and T. R. Shrout, "Ultrahigh strain and piezoelectric behavior in relaxor based ferroelectric single crystals," *J. Appl. Phys.*, **82** [4] 1804-11 (1997).

2) S. Wada, S.-E. Park, L. E. Cross and T. R. Shrout, "Domain Configuration and Ferroelectric Related Properties of Relaxor Based Single Crystals," *J. Kor. Phys. Soc.*, **32** [2] S1290-3 (1998).

3) S.-E. Park and S. Wada, "Properties of Engineered Domain State Barium Titanate Single Crystals," *In Preparation*, (1998).

4) B. Jaffe, W. R. Cook and H. L. Jaffe, "The Perovskite Structure"; pp. 49-114 in Piezoelectric Ceramics, Vol. 3, *Non-Metallic Solids*, Academic Press Ltd., New York, 1971.

5) D. Hennings and A. Schnell, "Diffuse Ferroelectric Phase Transitions in $Ba(Ti_{1-y}Zr_y)O_3$ Ceramics," *J. Am. Ceram. Soc.*, **65** [11] 539-44 (1982).

6) R. C. Kell and N. J. Hellicar, "Structural Transitions in Barium Titanate-Zirconate Transducer Materials," *Acustica*, **6** 235-8 (1956).

7) S. Matsuzawa and S. Mase, "Method for Producing a Single Crystal of Ferrite," *U.S. Patent 4339301* (Jul. 13, 1982).

8) M. Imaeda and S. Matsuzawa, "Growth of Yttrium Iron Garnet Single Crystal by Solid-Solid Reaction," *1st Japan International SAMPE Symposium*, 419-24 (Nov. 28-Dec. 1, 1989).

9) T. Yamamoto and T. Sakuma, "Fabrication of Barium Titanate Single Crystals by Solid-State Grain Growth," *J. Am. Ceram. Soc.*, **77** [4] 1107-9 (1994).

10) T. Li, A. M. Scotch, H. M. Chan, M. P. Harmer, S. Park and T. R. Shrout, "Single Crystals of $Pb(Mg_{1/3}Nb_{2/3})O_3$-35 mol% $PbTiO_3$ from Polycrystalline Precursors," *J. Am. Ceram. Soc.*, **81** [1] 244-8 (1998).

11) P. W. Rehrig, G. L. Messing and S. Trolier-McKinstry, "Templated Grain Growth of Barium Titanate Single Crystals," *In Preparation*, (1998).

12) T. R. Armstrong, L. E. Morgens, A. K. Maurice and R. C. Buchanan, "Effects of Zirconia on Microstructure and Dielectric Properties of Barium Titanate Ceramics," *J. Am. Ceram. Soc.*, **72** [4] 605-11 (1989).

List of Figures

Fig. 1. Scanning electron micrograph of $BaTiO_3$ template crystal, $Ba(Zr_{0.05}Ti_{0.95})O_3$ grown crystal, and the Ti-rich polycrystalline matrix $Ba(Zr_{0.05}Ti_{0.95})O_3$ + 3 mole% TiO_2 after 30 h at 1350°C.

Fig. 2. Dielectric constant (a) and dielectric loss (b) as a function of temperature at 1 kHz for TGG grown $Ba(Zr_xTi_{1-x})O_3$ single crystals, where $x = 0.045$ and 0.05. ($T_{R\text{-}O}$ = rhombohedral to orthorhombic transition, $T_{O\text{-}T}$ = orthorhombic to tetragonal transition)

Fig. 3. Dielectric constant as a function of temperature and frequency for TGG grown $Ba(Zr_{0.085}Ti_{0.915})O_3$ single crystal.

Fig. 4. Polarization (a) and strain hysteresis (b) as a function of electric field for ⟨001⟩ oriented TGG $Ba(Zr_xTi_{1-x})O_3$ single crystals, where $x = 0.045$ and 0.05.

Fig. 5. Unipolar strain hysteresis as a function of electric field for ⟨001⟩ oriented TGG $Ba(Zr_xTi_{1-x})O_3$ single crystals, where $x = 0.045$ and 0.05.

Fig. 6. Polarization (a) and strain hysteresis (b) as a function of electric field for ⟨001⟩ oriented TGG $Ba(Zr_{0.085}Ti_{0.915})O_3$ single crystal.

Fig. 7. Unipolar strain hysteresis as a function of electric field for ⟨001⟩ oriented TGG $Ba(Zr_{0.085}Ti_{0.915})O_3$ single crystal.

Table 1. Effective electromechanical coupling data for 4.5 mol% Zr-doped orthorhombic $BaTiO_3$ single crystal, oriented along the pseudocubic <001>, grown by TGG.

Fig. 1 Scanning electron micrograph of $BaTiO_3$ template crystal, $Ba(Zr_{0.05}Ti_{0.95})O_3$ grown crystal, and the Ti-rich polycrystalline matrix $Ba(Zr_{0.05}Ti_{0.95})O_3$ + 3 mole % TiO_2 after 30 h at 1350°C.

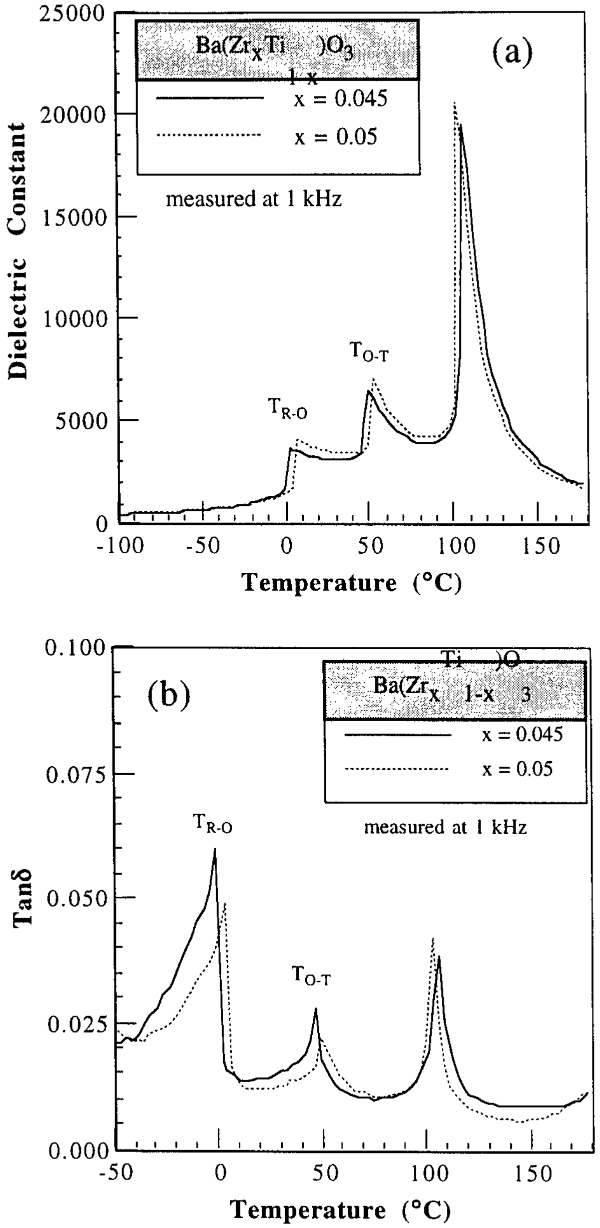

Fig. 2 Dielectric constant (a) and dielectric loss (b) as a function of temperature at 1 kHz for TGG grown $Ba(Zr_xTi_{1-x})O_3$ single crystals, where x = 0.045 and 0.05. ($T_{R\text{-}O}$ = rhombohedral to orthorhombic transition, $T_{O\text{-}T}$ = orthorhombic to tetragonal transition)

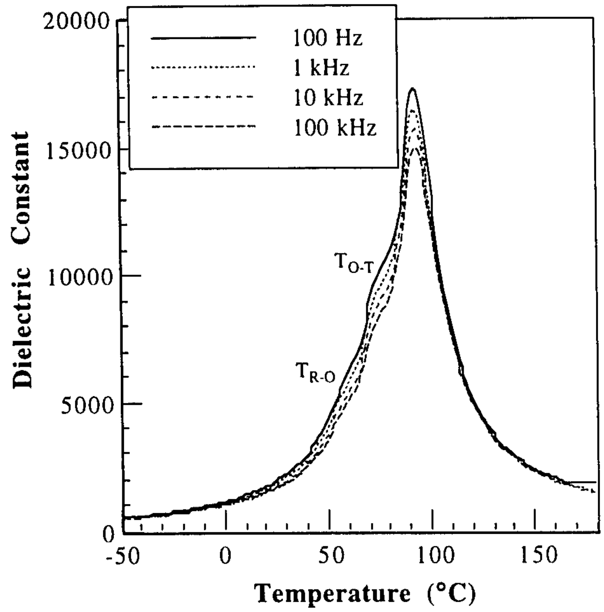

Fig. 3 Dielectric constant as a function of temperature and frequency for TGG grown $Ba(Zr_{0.085}Ti_{0.915})O_3$ single crystal.

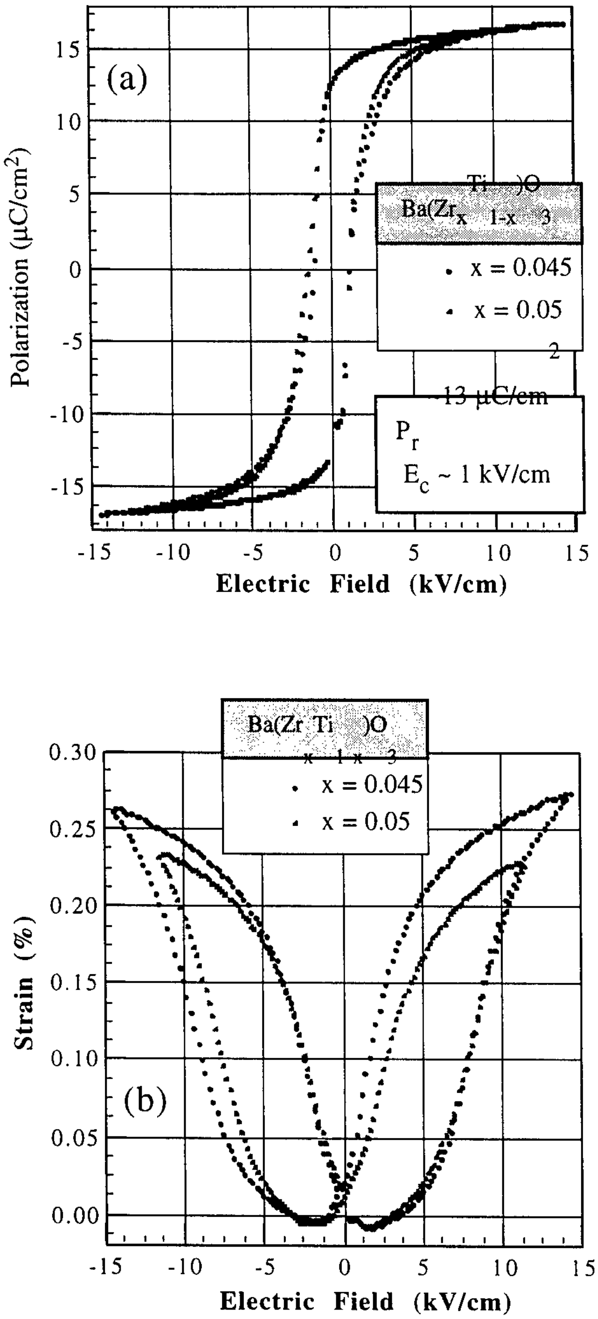

Fig. 4 Polarization (a) and strain hysteresis (b) as a function of electric field for ⟨001⟩ oriented TGG $Ba(Zr_xTi_{1-x})O_3$ single crystals, where x = 0.045 and 0.05.

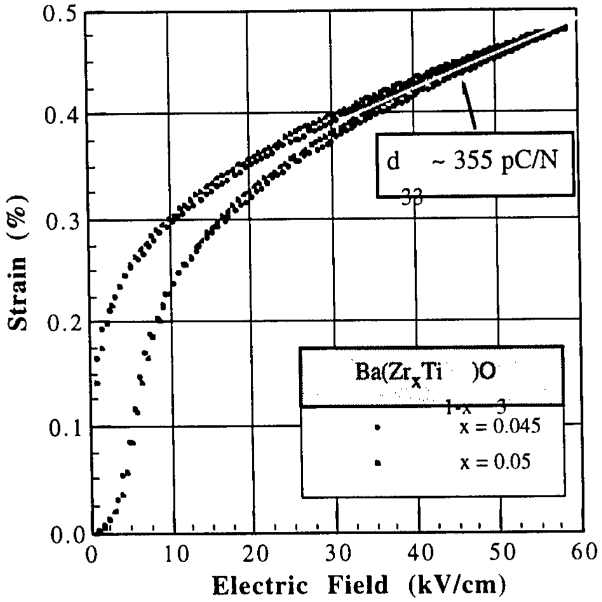

Fig. 5. Unipolar strain hysteresis as a function of electric field for ⟨001⟩ oriented TGG $Ba(Zr_xTi_{1-x})O_3$ single crystals, where x = 0.045 and 0.05.

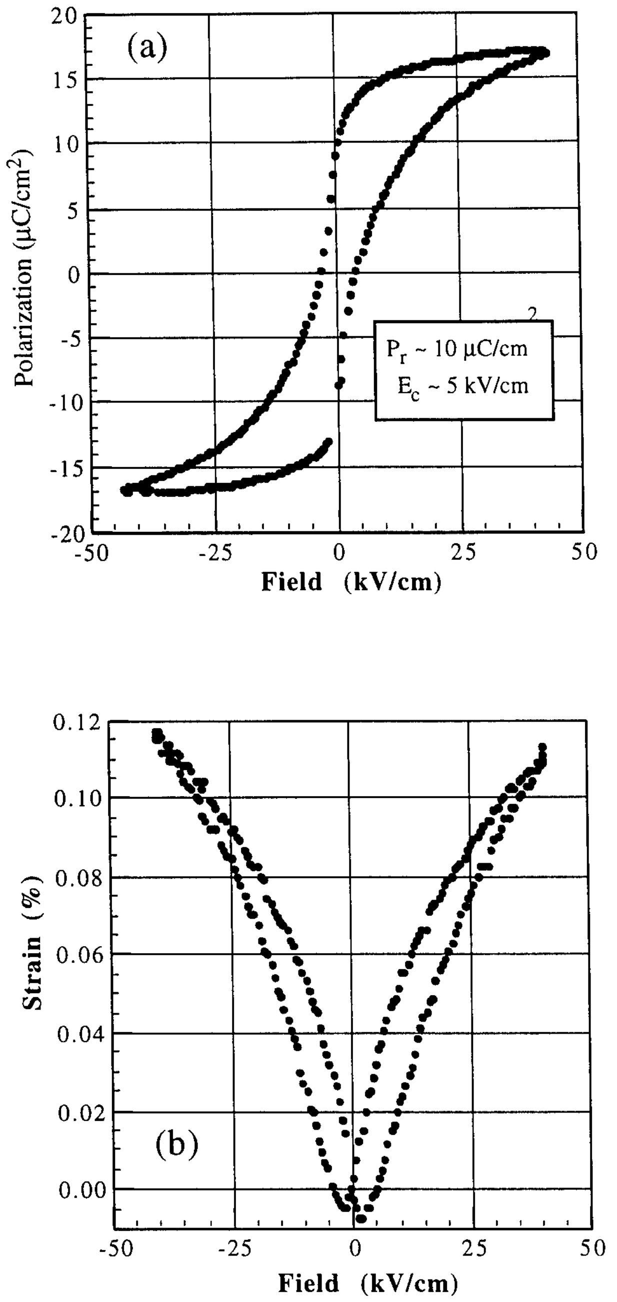

Fig. 6 Polarization (a) and strain hysteresis (b) as a function of electric field for ⟨001⟩ oriented TGG $Ba(Zr_{0.085}Ti_{0.915})O_3$ single crystal.

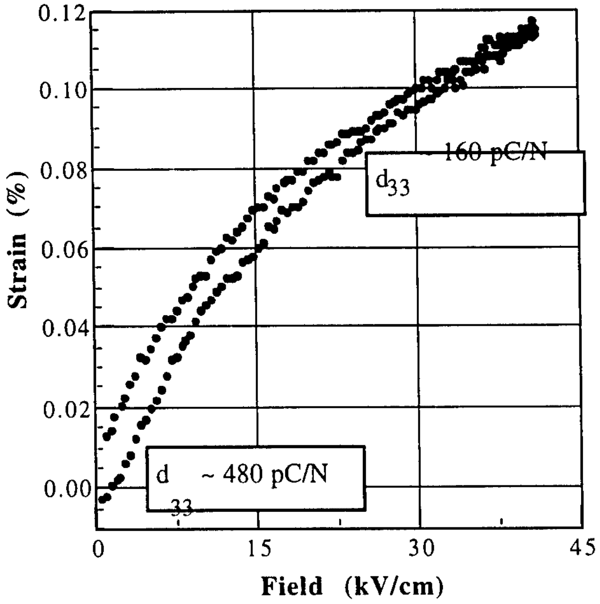

Fig. 7 Unipolar strain hysteresis as a function of electric field for ⟨001⟩ oriented TGG $Ba(Zr_{0.085}Ti_{0.915})O_3$ single crystal.

Table 1. Effective electromechanical coupling data for 4.5 mol% Zr-doped orthorhombic $BaTiO_3$ single crystal, oriented along the pseudocubic <001>, grown by TGG.

DC bias (kV/cm)	Freq. Constant (Hz•m)	k_{33}	ε_{33}^{T}	S_{33}^{D} (10^{-12} m^2N^{-1})	S_{33}^{E} (10^{-12} m^2N^{-1})	d_{33} (pC/N)
4.6	1691	0.74	770	14.5	31.7	340
1.0	1689	0.74	730	14.6	31.7	330

APPENDIX D

Crystallographic engineering in high-performance piezoelectric crystals

Seung-Eek Park*, Satoshi Wada, Paul W. Rehrig, Shi-Fang Liu,
L. Eric Cross, and Thomas R. Shrout

Materials Research Laboratory, The Pennsylvania State University, University Park,PA16802

ABSTRACT

Crystallographic engineering, a concept to utilize crystal anisotropy as well as an engineered domain configuration, resulted in significant enhancement in piezoelectric activity for normal ferroelectric $BaTiO_3$ crystals. Electromechanical couplings (k_{33}) ~ 85% and piezoelectric coefficients (d_{33}) as high as 500 pC/N, higher or comparable to those of lead based ceramics such as PZT and significantly larger than those of tetragonal $BaTiO_3$ crystals (k_{33} ~ 65%, d_{33} ~ 130 pC/N), were detected from crystallographically engineered orthorhombic $BaTiO_3$ crystals. Orthorhombic $BaTiO_3$ phase could be stabilized by Zr-doping at room temperature and enhanced electromechanical coupling (k_{33}) ~ 75% was detected also by using crystallographic engineering. Macroscopic symmetry (4mm) was suggested for <001> poled rhombohedral (3m) and orthorhombic (2mm) crystals, based on the engineered domain configuration.

Keywords : Perovskite crystal, relaxor-$PbTiO_3$, crystallographic engineering, engineered domain state, piezoelectrics, hysteresis.

1. INTRODUCTION

Recent crystallographic engineering of relaxor ferroelectric single crystals of $Pb(Zn_{1/3}Nb_{2/3})O_3$ (PZN), $Pb(Mg_{1/3}Nb_{2/3})O_3$ (PMN) and their solid solutions with the normal ferroelectric $PbTiO_3$ (PT) revealed piezoelectric properties much superior to morphotropic phase boundary (MPB) ceramics such as $Pb(Zr,Ti)O_3$ (PZT).[1-4] Previously, ultrahigh piezoelectric properties (k_{33} ~ 94%, d_{33} ~ 2500 pC/N), hysteresis minimized strain values as high as 0.6%, and large E-field induced strain values (1.7%) were reported (see figure 1)[5]. Actuator performance of these crystals was also found to be superior to polycrystalline ceramics, i.e. the strain energy density ~ 66400 J/m^3 was delivered at 20kV/cm for PZN-4.5%PT crystals, 5 times higher than hard PZT. These ultrahigh properties could be achievable from rhombohedral crystals oriented along their non-polar <001> axis, a key concept of crystallographic engineering. In contrast, rhombohedral crystals poled along their polar direction <111> exhibited significantly inferior properties, i.e. k_{33} < 50% and d_{33} ~ 100 pC/N.

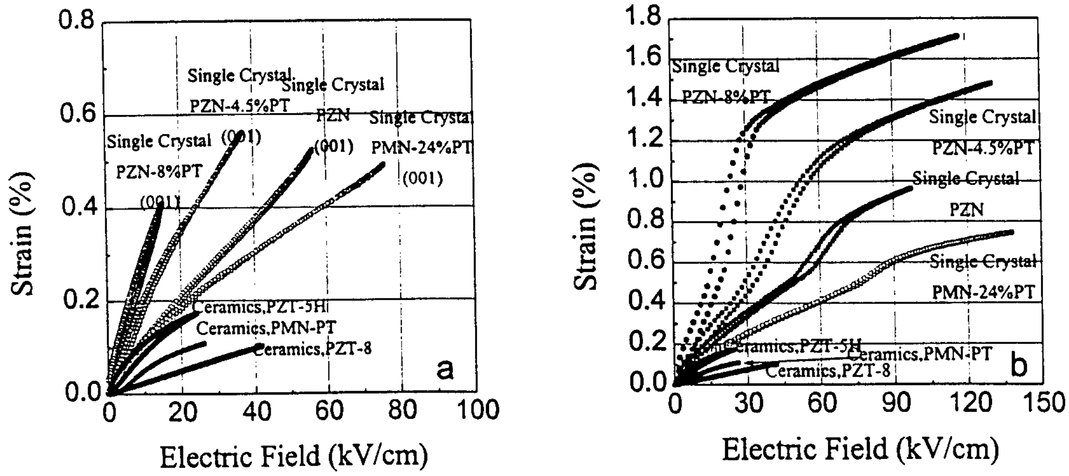

Figure 1 Strain vs. E-field behaviors for crystals of PZN-PT and PMN-PT and for various ceramics.

---

* Correspondence: Email:sxp37@psu.edu

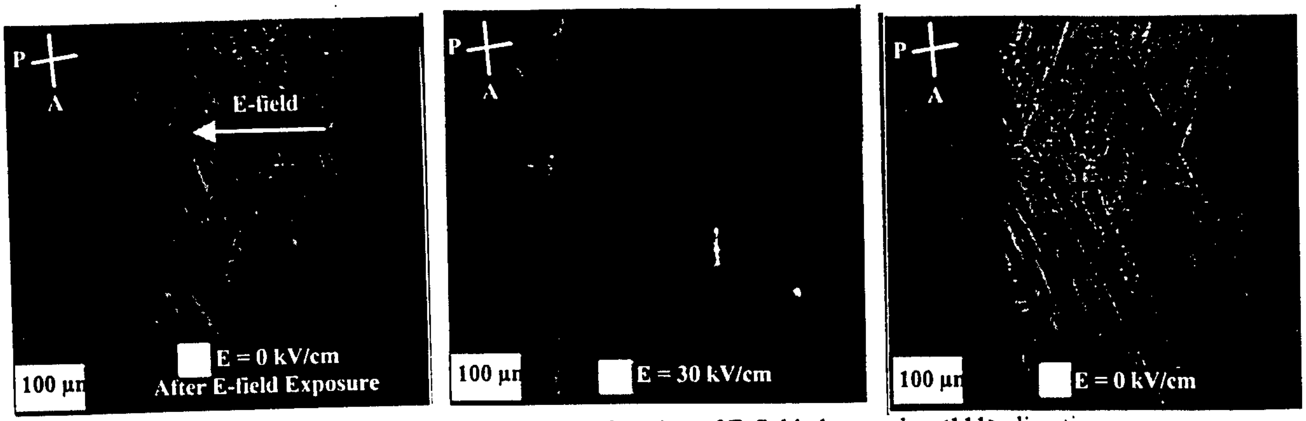

Figure 2 Domain configuration as a function of E-field along polar <111> direction

In addition to the ultrahigh piezoelectric performance, hysteresis minimized strain vs. E-field behavior (see figure 1a) was another important characteristic of crystallographically engineered relaxor ferroelectric single crystals. This behavior indicates minimal domain motion under bias, a phenomenon not expected for crystals of multi-domain state. The stable domain configuration resulted in highly reliable materials for actuation, i.e. no material degradation was detected for more than 10^7 unipolar driving cycles at high fields (>50 kV/cm, 1kHz).[5]

Based on the concept of crystallographic engineering used for high performance relaxor ferroelectric single crystals, single crystals or epitaxial form of any known ferroelectric materials may exhibit significant enhancement in electromechanical performance. It was the objective of this paper to review and apply the concept to other ferroelectric crystals such as $BaTiO_3$, in order to evaluate the possibility of piezoelectric performance enhancement. Strain vs. E-field behavior of engineered crystals will be discussed with respect to crystal structure and domain configuration.

2. ENGINEERED DOMAIN CONFIGURATION AND MACROSCOPIC SYMMETRY

In regard to crystallographic engineering, the ability to engineer a macroscopic symmetry different from the local symmetry (lattice symmetry) was suggested.[6] As can be found for the case of the poled piezoelectric ceramics, the macroscopic symmetry must be ∞mm regardless of the lattice symmetry resulting from randomly orientated grains where polar vectors are oriented as close to the direction of E-field as possible. For ferroelectric single crystals, single domain crystals may possess macroscopic symmetry identical to the lattice symmetry. Figures 2(a), 2(b) and 2(c) exemplify the domain configuration for PZN crystal oriented along their polar <111> as a function of E-field. At approximately 30 kV/cm (figure 2(b)), the PZN crystal became single domain. However, upon removal of the E-field, the initial multidomain state of figure 2(a) was recovered as shown in figure 2(c). This domain instability results in hysteresis in strain vs. E-field behaviors for <111> oriented PZN crystals as previously reported.[2,6] Therefore, the point group of <111> oriented rhombohedral crystals under bias (30 kV/cm for PZN crystals) are both macroscopically and microscopically 3m.

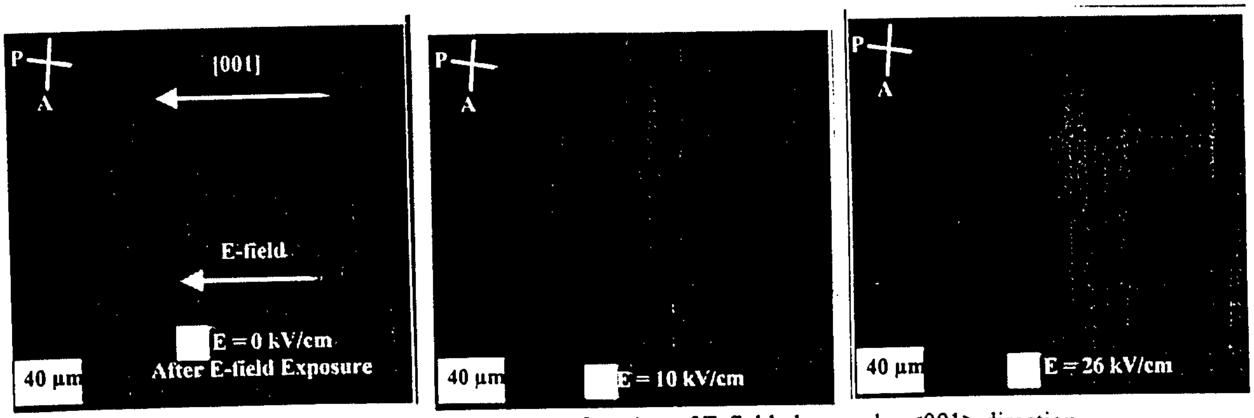

Figure 3 Domain configuration as a function of E-field along polar <001> direction

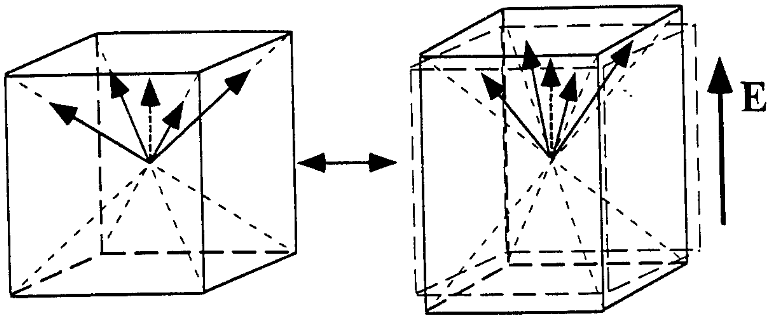

Figure 4 Schematic of engineered domain state in <001> poled rhombohedral perovskite crystals.

In contrast to the domain instability observed with <111> oriented PZN crystals, <001> oriented crystals exhibited a stable domain configuration as shown in figure 3. Domain configuration did not change under bias, being further evidenced by hysteresis minimized strain vs. E-field behavior as shown in figure 1(a). Similar domain behavior was found in other <001> oriented rhombohedral crystals such (1-x)PZN-xPT (x=0-0.09), or (1-y)PMN-yPT (y=0.2-0.35), or (1-z) PSN-zPT (z=0.25-0.45). As shown in figure 4, each domain in <001> oriented crystals must have four possible polarization directions, - <111>, <-111>, <1-11>, and <-1-11>. For <001> oriented crystals to exhibit a static domain configuration under bias, each domain must be distributed equivalently. As a result, each domain experiences the same driving force for reorientation with respect to an applied E-field, otherwise domain reorientation under bias would occur resulting in domain reorientation and subsequent hysteresis in the strain vs. E-field curve. Therefore, the coexistence of domains with four equivalent polar vectors results in 4-fold axes along [001], and consequently the macroscopic symmetry must be 4mm out of local 3m symmetry.

This issue of macroscopic symmetry is important specifically in transducer or actuator performance simulations as well as in measuring dielectric, piezoelectric, and elastic properties, because it determines the anisotropy and subsequently the number of independent electromechanical parameters. Although the lattice symmetry is rhombohedral 3m for PZN crystals, for example, the <001> poled crystals should be considered as tetragonal 4mm as discussed above. Figure 5 presents crystal sample shapes and orientation to measure the two independent dielectric constants, three piezoelectric constants and five elastic constants for <001> poled ferroelectric rhombohedral perovskite crystals.

It is believed that crystallographic engineering is key to acquire ultrahigh piezoelectric property in relaxor ferroelectric single crystals. Here, the question arises, will similar piezoelectric property enhancement be observed for normal ferroelectric perovskite crystals? - the topic of the following section.

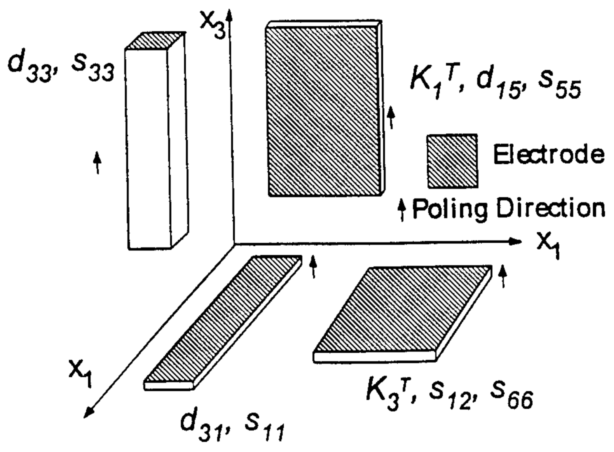

Figure 5 Sample shape and orientation for electromechanical property measurement.

Table 1 Phase transitions of $BaTiO_3$ crystal as a function of temperature

Temperature Range	*>130°C*	*120°C to 0°C*	*0°C to -90°C*	*<-90°C*
Primitive Cell Symmetry	Cubic	Tetragonal	Pseudo-monoclinic	Rhombohedral
Point Group	m3m	4mm	mm2	3m
Macro-symmetry*	-	4mm	4mm	4mm

* under dc-bias along <001>

3. CRYSTALLOGRAPHICALLY ENGINEERED $BaTiO_3$ BASED SINGLE CRYSTALS

3.1 $BaTiO_3$ crystals with high piezoelectric performance

Table 1 summarizes the phase transitions observed in $BaTiO_3$. As considered in the phenomenological theory by Devonshire[7], the unit cell symmetry dictates the direction of polar shift, i.e. orthogonal (4mm), face diagonal (mm2), and body diagonal (3m) based on the primitive perovskite cell. Also in orthorhombic crystals, four polarization directions (<101>, <011>, <-101>, <0-11>) are energetically equivalent and four types of domains will be equally populated under <001> E-field. As previously discussed, this configuration results in a macroscopic symmetry 4mm. As demonstrated in table 1, it is interesting to note that the macroscopic crystal symmetry retains 4mm regardless of lattice symmetry changes under <001> E-field.

Figure 6 presents longitudinal electromechanical coupling (k_{33}) as a function of temperature for <001> poled $BaTiO_3$ crystals, under dc-bias. Samples for measuring dielectric and piezoelectric properties were prepared using commercially available $BaTiO_3$ single crystals (optical grade, Fujikura Ltd.), grown by top seeded solution growth (TSSG) technique. At room temperature, the increase of k_{33} value from ~0.53 (0 kV/cm) to 0.65 (6kV/cm) was the result of domain reorientation, which had been partially depoled due to domain instability in the tetragonal crystal poled along its polar direction <001>. Note that a similar behavior was found for rhombohedral PZN crystals poled along its polar <111> direction as presented in the previous section. It is also noted that k_{33} ~ 0.53 (0 kV/cm), a value from partially depoled crystals in this work, corresponds to values reported earlier, i.e. ~0.56[8] and ~0.55[9] for tetragonal $BaTiO_3$ crystals.

At lower temperatures, k_{33} was also found to be dependent on dc-bias due to crystal depoling as a result of phase transitions as well as domain instability. For an orthorhombic crystal at -5°C, k_{33} ~ 0.7 initially detected at 0 kV/cm increased with increasing bias, followed by k_{33} as high as 0.83 at 6 kV/cm. After E-field exposure, the unbiased k_{33} value was as high as 0.79, being a starting point of second cycle (dashed arrows in figure 6). The initial lower value of coupling for the first cycle

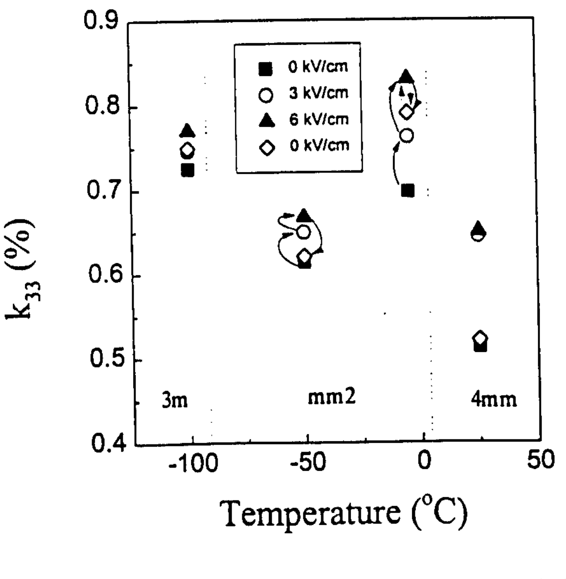

Figure 6 k_{33} as a function of temperature for <001> poled $BaTiO_3$ crystals under various dc-bias. (solid arrows : first cycle, dashed arrows: second cycle)

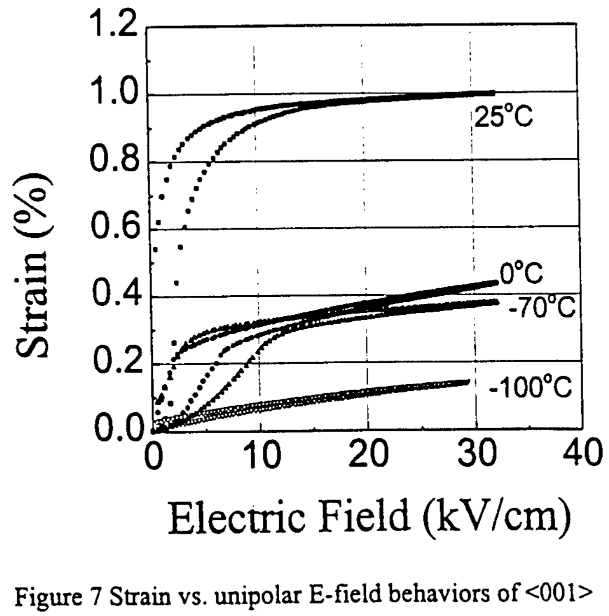

Figure 7 Strain vs. unipolar E-field behaviors of <001> $BaTiO_3$ crystal

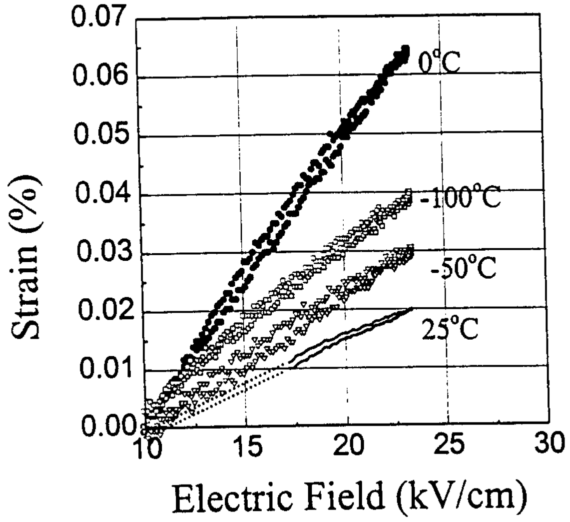

Figure 8 Strain vs. E-field behavior as a function of temperature for <001> oriented $BaTiO_3$ crystals (non-hysteretic portion).

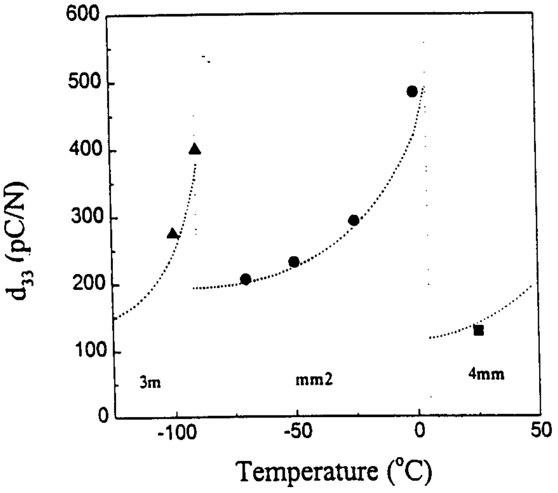

Figure 9 d_{33} as a function of temperature for <001> oriented $BaTiO_3$ crystals.

(solid arrows in figure 6) must be a consequence of depoling caused by the tetragonal-orthorhombic phase transition. Note that a k_{33} ~ 0.83 for non-lead $BaTiO_3$ crystals is significantly larger than room temperature k_{33} values of Pb-based polycrystalline PZT's (0.5 to 0.75), the current piezoelectric material of choice.

Figure 7 presents strain vs. unipolar E-field behavior for <001> poled $BaTiO_3$ crystals at various temperatures. Room temperature strain values as high as 1% is a consequence of depoling and domain reorientation. This significant c-a domain switching may be ascribed to the stress by LVDT probe. Note that total strain as high as 1.07% strain is involved with a full ferroelectric strain curve of $BaTiO_3$ crystals, however, it is not useful for practical actuation. Single domain state tetragonal crystals, reflected by the non-hysteretic strain vs. E-field behavior, could be achieved at E-fields > ~10 kV/cm at room temperature as shown in figure 7. Piezoelectric coefficient d_{33} ~ 128pC/N, similar to that theoretically simulated by Devonshire[7], was calculated from the non-hysteretic portion of strain vs. E-field behavior at 20 kV/cm.

The hysteresis found in the orthorhombic crystal (0°C, -70°C at E<10kV/cm in figure 7) was also ascribed to domain instability. In contrast, the engineered domain state of the rhombohedral crystal (-100°C) was found to be stable as can be seen in figure 7, resulting in the crystal retaining macro-symmetry 4mm for the overall range of applied E-field. Note relaxor based single crystals with stable engineered domain states are also rhombohedral. Although further study is required to clarify the relationship between crystal structure and engineered domain state, it is suggested that lattice symmetry should determine the (in)stability of the engineered domain state and that rhombic lattice distortion be critical to stabilize the domain state in <001> poled ferroelectric crystals.

For comparison of piezoelectric activity, only non-hysteretic portion of the strain vs. E-field (E>10 kV/cm) curves are presented in figure 8 and apparent d_{33}'s calculated from figure 8 are plotted in figure 9. As plotted, crystallographic engineering results in $BaTiO_3$ crystals with significantly enhanced piezoelectric activity such as d_{33} ~ 500 pC/N. This value is comparable to room temperature d_{33} values of PZT's. The rhombohedral $BaTiO_3$ crystal at -100°C exhibited d_{33} as high as 350 pC/N, also larger than that of polycrystalline PZT's at the same temperature.[10] Here another question arises, - can orthorhombic or rhombohedral $BaTiO_3$ be stabilized at room temperature? Piezoelectric properties of orthorhombic $Ba(Zr,Ti)O_3$ crystals is the topic of the following section.

3.2 Crystallographically Engineered $Ba(Zr,Ti)O_3$ Single Crystals

It is well known that the phase transition temperatures in $BaTiO_3$ can be altered by doping with either A or B-site substitutions.[8] Zirconium is one element that pinches the transition temperatures so that the rhombohedral-orthorhombic and orthorhombic-tetragonal phase transition temperatures are raised while the Curie temperature is lowered.[8] By varying the amount of dopant it is possible to stabilize either the rhombohedral and orthorhombic phases at room temperature.[11,12] A

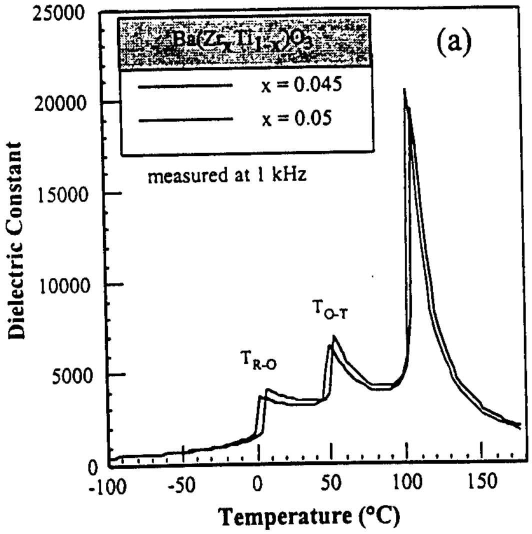

Figure 10 Dielectric constant as a function of temperature at 1 kHz for TGG grown Ba(Zr$_x$Ti$_{1-x}$)O$_3$ single crystals, where x = 0.045 and 0.05. (T$_{R\text{-}O}$ = rhombo. to ortho. transition, T$_{O\text{-}T}$ = ortho. to tetra. transition).

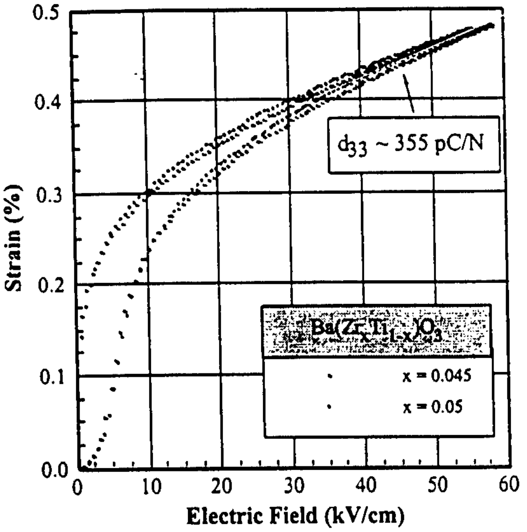

Figure 11 Strain vs. unipolar E-field behaviors for ⟨001⟩ oriented TGG Ba(Zr$_x$Ti$_{1-x}$)O$_3$ single crystals, where x = 0.045 and 0.05.

templated grain growth (TGG) was used to produce crystals with Zr concentrations between 4.5 and 8.5 mol% for rapid assessment of crystals of varying composition. Details in the crystal growth procedure can be found elsewhere.[13]

Figure 10 shows the dielectric constant (k_3^T) as a function of temperature and mol% zirconium. As seen in polycrystalline Zr-doped BaTiO$_3$, the transition temperatures are pinched with increasing mol% zirconium.[11,12,14] The 4.5 (BZT-4.5) and 5.0 (BZT-5.0) mol% Zr samples show distinct transition temperatures with both the rhombohedral-orthorhombic and orthorhombic-tetragonal transition temperatures shifted up by approximately 80°C (T$_{R\text{-}O}$ = 0°C) and 45°C (T$_{O\text{-}T}$ = 50°C), respectively. The result of this shift is that the orthorhombic phase is stabilized at room temperature.

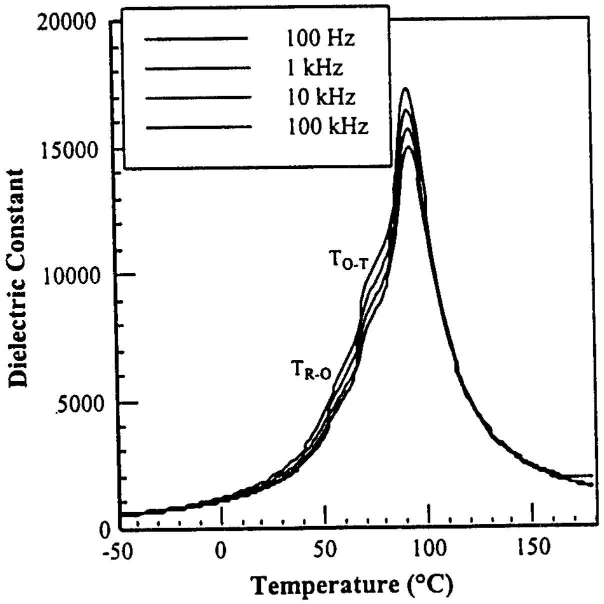

Figure 12 Dielectric constant as a function of temperature and frequency for TGG grown Ba(Zr$_{0.085}$Ti$_{0.915}$)O$_3$ single crystal.

Figure 11 shows the unipolar strain behavior at room temperature for BZT-4.5 and BZT-5.0 crystals poled and excited along the pseudocubic ⟨001⟩ as a function of electric field. Both crystals show maximum strain levels of approximately 0.48% at a maximum field of ~60 kV/cm, which includes ~0.35% strain associated with domain reorientation. It is noted that this partial depoling at lower field was also detected for orthorhombic $BaTiO_3$ crystals in the previous section. After saturation, the strain behavior from 30-60 kV/cm corresponds to a d_{33} of 355 and 340 pC/N for BZT-4.5 and BZT-5.0, respectively. Using the IEEE standard technique[14], k_{33} and d_{33} values of 0.74 and 340 pC/N, respectively, were also determined for 4.5 mol% Zr-doped orthorhombic $BaTiO_3$ single crystal (BZT-4.5), under 5 kV/cm. It is emphasized that further compositional tuning closer to MPB must result in further increased k_{33} and d_{33} values as in case of $BaTiO_3$ crystals (see figures 6 and 9).

In contrast to orthorhombic BZT crystals, piezoelectric coefficients and strain behavior could not be clearly determined for rhombohedral BZT crystals such as BZT-R8.5 (8.5mol% Zr) because the phase transitions were pinched even more with diffuse transition behavior, as shown in figure 12. Studies associated with further optimization of composition are ongoing to achieve enhanced piezoelectric properties by crystallographic engineering.

4. CONCLUSIONS

Crystallographic engineering resulted in ferroelectric perovskite single crystals with significantly enhanced piezoelectric properties. It was deduced from in-situ domain observation that an engineered domain configuration of <001> oriented rhombohedral and orthorhombic crystals results in the macroscopic tetragonal symmetry 4mm out of local rhombohedral 3m symmetry. Crystallographic engineering of $BaTiO_3$ crystals resulted in orthorhombic crystals (0°C) with k_{33} ~ 85% and d_{33} ~ 500 pC/N, better or comparable to those of PZT's. At -90°C, rhombohedral $BaTiO_3$ crystals with k_{33} ~ 79% and d_{33} ~ 400 pC/N were found to be superior to PZT's at the same temperature. Although possessing the same macroscopic symmetry 4mm, rhombohedral (3m) crystals (-100°C) exhibited a stable domain configuration whereas the adjacent orthorhombic crystal (-70°C) were depoled. Single crystals of room temperature orthorhombic $Ba(Zr,Ti)O_3$ prepared using templated grain growth technique exhibit k_{33} and d_{33} values up to 0.74 and 355 pC/N, respectively, also employing crystallographic engineering.

ACKNOWLEDGMENTS

Authors would like to thank Hua Lei for her help with sample preparation. We also appreciate Clive Randall for his valuable comments. This work was supported by ONR and DARPA.

REFERENCES

1. J. Kuwata, K. Uchino, and S. Nomura, "Dielectric and Piezoelectric Properties of 0. $91Pb(Zn_{1/3}Nb_{2/3})O_3$ -$0.09PbTiO_3$ Single Crystals," *Jap. J. Appl. Phys.*, **21** [9], pp. 1298-1302, 1982.
2. S.-E. Park and T. R. Shrout, "Ultrahigh Strain and Piezoelectric Behavior in Relaxor based Ferroelectric Single Crystals" *J. Appl. Phys.*, **82** [4], pp. 1804-1811, 1997.
3. S.-E. Park and T. R. Shrout, "Characteristics of Relaxor-Based Piezoelectric Single Crystals for Ultrasonic Transducers," *IEEE Trans. on Ultras., Ferro. Freq. Cont. on Ultras. Trans..*, **44** [5], 1140-1147, 1997.
4. S.-F. Liu, S.-E. Park, T. R. Shrout, and L. E. Cross, "E-field Dependence of Piezoelectric Properties for Rhombohedral $0.955Pb(Zn_{1/3}Nb_{2/3})O_3$-$0.045PbTiO_3$ Single Crystals," *J. Appl. Phys.*, in press.
5. S.-E. Park, V. Vedula, M.-J. Pan, W. S. Hackenberger, P. Pertsch, and T. R. Shrout, "Relaxor Based Ferroelectic Single Crystals for Electromechanical Actuators," *Proceedings on SPIE's 5th Annual International Symmposium on Smart Structures and Materials*, San Diego, CA, March 1998.
6. S. Wada, S.-E. Park, L. E. Cross, and T. R. Shrout, "Domain Configuration and Ferroelectric Related Properties of Relaxor-based Single Crystals," *J. Korean Phys. Soc.*, **32**, pp.1290-1293, 1998.
7. A. F. Devonshire, "Theory of Batium Titanate. - Park II," *Philosophical Magazine*, **42**, pp. 1065-1079, 1951.
8. B. Jaffe, W. R. Cook and H. L. Jaffe, *Piezoelectric Ceramics*, Academic Press Ltd., New York, 1971.
9. M. Zhonik, P. Bernasconi, M. Duelli, R. Schlesser, and P. Gunter, "Dielectric, elastic, piezoelectric, electro-optic, and elasto-optic tensors of $BaTiO_3$ crystals," Phys. Rev. B, **50** [9], pp. 5941-5948, 1994.
10. X. L. Zhang, Z. X. Chen, L. E. Cross, W. A. Schulze, "Dielectric and piezoelectric properties of modified lead titanate zirconate ceramics from 4.2 to 300K," J. Mat. Science, **18**, pp. 968-972, 1983.
11. D. Hennings and A. Schnell, "Diffuse Ferroelectric Phase Transitions in $Ba(Ti_{1-y}Zr_y)O_3$ Ceramics," *J. Am. Ceram. Soc.*, **65** [11], pp. 539-44, 1982.

12. R. C. Kell and N. J. Hellicar, "Structural Transitions in Barium Titanate-Zirconate Transducer Materials," *Acustica*, 6 , pp. 235-8, 1956.
13. P. Rehrig, "Templated grain growth of $BaTiO_3$ based perovskite single crystals," Ph. D. Thesis, The Pennsylvania State University, 1999.
14. IEEE Standard on Piezoelectricity, American National Standards Institue, 1976.

SPIE 99

Determination of elastic, piezoelectric and dielectric properties of $Pb(Zn_{1/3}Nb_{2/3})O_3$-$PbTiO_3$ single crystals

Jianhua Yin, Bei Jiang and Wenwu Cao

Material Research Laboratory
The Pennsylvania State University, University Park, PA16802

ABSTRACT

We report a set of measured material properties of $Pb(Zn_{1/3}Nb_{2/3})O_3$-$PbTiO_3$(PZN-PT) multi-domain single crystals. While deriving these properties, it was assumed that the rhombohedral PZN-PT crystals have 4mm symmetry when it is poled along the [001] of the original cubic direction. Samples with three pair of faces oriented in [001], [010] and [100] were made for the resonance measurements and additional samples with the orientations of [001], [110] and $[1\bar{1}0]$ were made for the ultrasonic measurements. Complete sets of the material constants were obtained for PZN-4.5%PT and PZN-8%PT. The coupling coefficient k_{33} is 94% for the PZN-8% PT and 90% for the PZN-4.5%PT. A piezoelectric constant d_{33} of 2300pC/N was obtained for the PZN-8% PT sample. These values are very encouraging for designing broadband ultrasonic transducers. Based these measurement results, the directional dependence of phase velocities and electromechanical coupling coefficients were analyzed. The calculations indicate that the coupling coefficient k_{31} and k_{33} has a maximum in the [110] and [001], respectively, a result consistent with the direct measurements. Errors in these measurements were also analyzed.

Keywords: PZN-PT crystal, Material properties, Piezoelectric, Ferroelectric, Ultrasonic measurement, Resonance.

INTRODUCTION

High electromechanical coupling coefficient and large piezoelectric constants are important for making broadband and high sensitivity ultrasonic transducers, actuators and other electromechanical devices. Recently, relaxor based ferroelectric single crystal $Pb(Zn_{1/3}Nb_{2/3})O_3$-$PbTiO_3$(PZN-PT) has generated a lot of interest because this crystal exhibited electromechanical coupling coefficient k_{33} more than 90% and the piezoelectric constant d_{33} exceeded 2000pC/N. If properly used, such high coupling coefficient and piezoelectric coefficient can produce a new generation of piezoelectric devices with much superior qualities.

The knowledge of material constants is essential for both fundamental studies and practical applications. Although high electromechanical coupling coefficient k_{33} and piezoelectric coefficient d_{33} have been reported for this PZN-PT crystal [1-3], many designers need more complete set of the material properties, including all the elastic, piezoelectric and dielectric constants. This paper reports a set of such data which were measured by using a combined method involving ultrasonic and resonance techniques.

In the ferroelectric state, the crystal symmetry of PZN-PT is rhombohedral if the PT concentration is less than 8%. Therefore, the dipoles in each of the unit cell will be formed along one of the eight possibly <111> orientations. Since the poling direction for the multi-domain system is along [001] of the cubic structure, the poled system statistically will have a pseudo-tetragonal symmetry. Our measurements in this paper were based on this assumption. For systems of 4mm symmetry, there are eleven independent constants in all of the elasto-piezo-dielectric matrices. The two dielectric constants ε_{11} and ε_{33} could be measured from low frequency capacitance. Two of the elastic constants s_{11}^E and s_{33}^D and two electromechanical coupling coefficients k_{33} and k_{31} could be calculated from the resonance and anti-resonance frequencies of the length-extension modes. Other five elastic constants $c_{11}^E, c_{12}^E, c_{44}^E, c_{66}^E$ and c_{44}^D could be determined from the measurements of phase velocities of the ultrasonic waves. Using this measurement scheme, only two types of orientations are needed, one is [001]/[010]/[100] and the other is [001]/[110]/ $[1\bar{1}0]$. Considering the strong geometry dependence of the material properties, the least number of samples will provide the most consistent data[4].

Unlike PZT ceramics, PZN-PT single crystal is not isotropic in the X-Y plane. The directional dependence of the material properties must be considered in the ultrasonic measurements. The relationship between phase velocity and elastic and piezoelectric coefficients can be obtained by solving the Christoffel wave equations for each given wave propagation direction. These velocities can be measured and used to calculate these material properties.

MEASUREMENT METHODS

A number of methods, such as static and quasi-static, impedance resonance, ultrasonic pulse-echo and Brillouin scattering, can be used to measure material properties[5-7]. These methods, except Brillouin scattering, were recommended and described in detail in the IEEE standards on piezoelectricity[5]. Impedance resonance and ultrasonic pulse-echo methods are often used because they are simple and relatively accurate, they are particularly suitable for high symmetry materials.

The impedance resonance method uses geometry control to single out a particular resonance mode, then use the coupling relation to calculate material properties based on the resonance and anti-resonance frequencies. Accurate measurement by this method requires a large aspect ratio of the sample in order to separate the modes. Ultrasonic method is to determine the material constants from the phase velocities of ultrasonic waves propagating in selected directions of the crystal. The velocities are determined by the time of flight of the ultrasonic echoes generated by the reflections at a pair of parallel surfaces of the sample.

Theoretically speaking, all of the independent elastic, piezoelectric and dielectric constants of a material with any crystal symmetry could be determined either by resonance method or by ultrasonic method alone if there are sufficient number of independently oriented samples. However, for materials of low symmetry, some geometry for resonance measurement might be difficult to prepare, especially when the available crystal is too small to make large aspect ratio samples, or there are certain crystal morphologies preventing growth in certain orientations. On the other hand, ultrasonic technique is accurate in measuring phase velocities, but large errors could be introduced when using them to calculate material constants from those complicate combinations of the velocities. In this work we try to use a combined scheme, which uses only those simple pure modes in each method. Two sets of samples were prepared and measured, one has 8% PT concentration and the other has 4.5% PT concentration. Results will be compared and discussed.

SAMPLE PREPARATION AND DETERMINATION OF INDEPENDENT CONSTANTS

PZN-PT went through a cubic to rhombohedral ferroelectric phase transition before being cooled down to room temperature. The dipoles of each unit cell could be formed along one of the eight <111> possible directions as shown in Fig. 1. However, due to the relaxor nature, the crystal can hold a large effective polarization only when the electric field is applied along one of the six <100> directions of the original cubic structure. As shown in Fig. 2 there are only four possible orientations left for the polarization after the application of the electric field. Such a poling field created a multi-domain system with equal probability of these four domain states. Statistically, the global symmetry should be close to 4mm. The orientations of the prepared samples with respect to the cubic coordinates were obtained from Laue X-ray diffraction pattern with an accuracy of .3°.

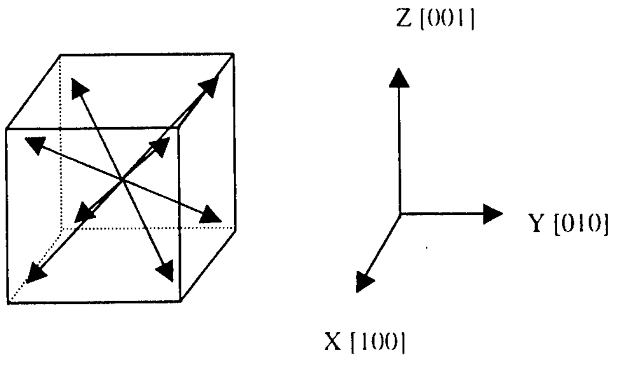

Fig. 1 Possible orientations of polarization in PZN-PT before poling

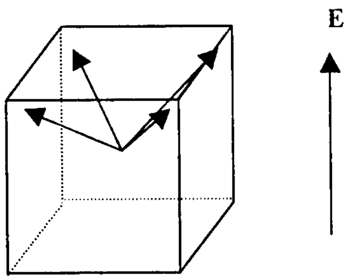

Fig. 2 Possible orientations of polarization in PZN-PT after poling

The as grown crystals were first orientated and cut into proper shape. Then, they were polished and spattered with gold electrodes, and finally being poled in the [001] direction by applying an external electric field of 10kV/cm. The final size of the samples for ultrasonic measurements was about 3x3x1 mm^3. For the length extension resonance measurements, the sample aspect ratio was about 5 to guarantee pure modes. In order to make the measurements more accurate we have prepared several sets of samples, particularly the bar samples with different aspect ratios, for comparison. In addition, a bar with its length in [110] and thickness in [001] was also made to verify the anisotropy effect.

The basic scheme used for determining the complete set of the material constants is given below in the diagram of Fig. 3. As one can see that all the independent material properties could be determined from samples of two type of orientations. In one type, the three pairs of faces are oriented in [100], [010] and [001], and the in the other type the orientations are [001], [110] and [$1\bar{1}0$].

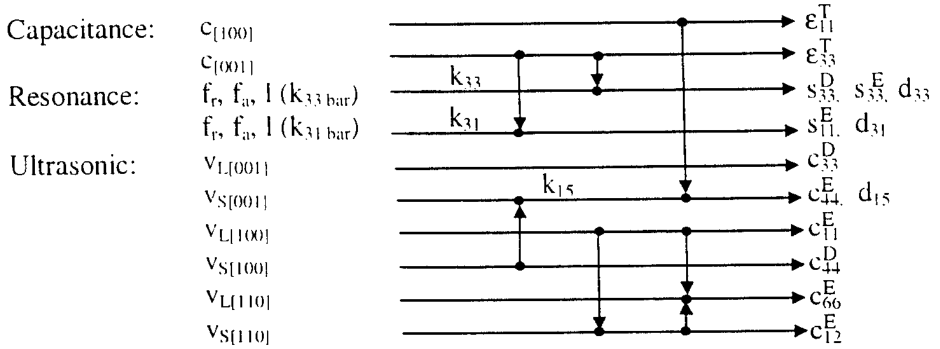

Fig. 3 Procedure of determination of independent material constants.

MEASUREMENT RESULTS

A 15MHz longitudinal wave transducer and a 20MHz shear wave transducer were used for the pulse-echo method. The pulse was exited by a Panametrics 200MHz Pulser/Receiver. The time of flight between echoes were measured by using a Tektronix digital oscilloscope. In any selected direction of the crystal, there are one longitudinal and two shear propagation modes. The two shear waves can be distinguished and tested by rotating the shear transducer by 90°. Table I shows part of

Table I Measured phase velocities (m/s) in PZN-4.5%PT crystal

Sample	v_l^{100}	v_s^{100}	v_l^{110}	v_{s1}^{110}	v_{s2}^{110}	v_l^{001}	v_s^{001}
#1				2842 2880	711	4149	2831
#2				2887	723	4099	2789
#3	3594	2854				4161	2855 2815
#4	3659	2829				4148	2803
#5			4622	2855	732	4125	2811
#6			4646				
#7						4103	2761
#8	3587	2800				3967	2843
Avg.	3613	2828	4634	2866	722	4107	2814
δ %	0.9	0.8	0.25	0.5	1.2	1.5	1.0

the measured phase velocities of ultrasound in the PZN-4.5%PT single crystals. For the length-extension resonance measurements, a HP 4194A impedance/gain-phase analyzer was used. The resonance and antiresonance frequencies, which are related to the minimum and maximum values of the impedance-frequency spectrum, can be measured accurately using the analyzer. Some of the measured results from the length extension resonance are shown in Table II.

Table II Measured f_r and f_a from the length extension resonance for PZN-4.5%PT

k_{33} bars

L	l/w	f_r	f_a	$2lf_a$	k_{33}
4.05	9	143.875	298.000	2414	0.895
2.90	6.3	222.500	427.500	2480	0.876
3.10	4.5	217.500	408.75	2534	0.869
3.62	3.9	202.375	372.250	2695	0.863

k_{31} bars

$k_{31[110]}$	$2lf_r$	$k_{31[100]}$	$2lf_r$
0.918	1723	0.480	1466
0.911	1752	0.449	1394
0.909	1766	0.491	1456
0.910	1737	0.488	1359

k_t plate

k_t^1	$2lf_r$
0.505	4102

Relative error: k_{33}: δ=3%, k_{31}: δ=2.8%, s_{33}^D: δ=2.6%, s_{11}^E: δ=1%

The electromechanical coupling coefficients, k_{33} and k_{31}, were also measured and listed in Table II for comparison. The lateral coupling coefficient k_{31} are different in [100] and [110], therefore we labeled them with the orientation in the subscripts. From the measured results in Table I and Table II, the complete set of elastic, piezoelectric and dielectric constants can be calculated and the final results are listed in Table III and Table IV for both PZN-8%PT and PZN-4.5%PT .

Large electromechanical coupling coefficient k_{33} was observed for both PZN-4.5%PT and PZN-8%PT. From the results the 8% PT sample is better than the 4.5% samples. However, even the 4.5%PT samples show a k_{33} value of 90%. The piezoelectric constant d_{33} is 3-4 times of the best PZT ceramic samples we have today, it reaches 2300 pC/N for the 8%PT and about 1800 pC/N for the 4%PT. Compared to the value for PZT ceramics with k_{33} =70% and d_{33} =650 pC/N, the single crystal samples are much superior. Piezoelectric materials having large electromechanical coupling coefficients can produce broader band transducers and the high piezoelectric coefficient will increase the sensitivity of sensors and transducers. The large d_{33} value is also good for other piezoelectric devices that demand high strains.

Despite the effort in our measurements, there are still some uncertainties in the measured results. The errors may come from several main sources: (1) measurement errors, including the size of the sample, parallel capacitance approximation for dielectric measurement and the measurement of the time of flight for the echoes; (2) misorientation of the sample; (3) inconsistency between different samples; (4) numerical errors from parameter calculations. We have quantified some of these errors in this work. Using a 15 MHz transducer, the error of measuring the sound velocity is less than 2% for sample with thickness larger than 1mm. The error in the measurement of capacitance is little large, around 5%. Error from misorientation can be analyzed from the calculations of sound velocities in different directions using the measured elastic, piezoelectric and dielectric constants, which will be discussed below. The largest error comes from item (3) above because the sample property depend strongly on the domain pattern and the domain pattern is controlled by the shape of the sample. This error could be very large for this single crystal system and it is the main cause of the inconsistencies in our measurements. We have tried to minimize this error by using less number of samples.

Table III Measured Material properties of PZN-8%PT Single Crystal.

Elastic Constants: c_{ij} (10^{10}C/m^2), s_{ij} (10^{-12} C/N)

c^E_{11}	c^E_{12}	c^E_{13}	c^E_{33}	c^E_{44}	c^E_{66}
11.1	10.2	9.97	10.2	6.1	6.56
c^D_{11}	c^D_{12}	c^D_{13}	c^D_{33}	c^D_{44}	c^D_{66}
12.6	11.7	7.93	13.0	6.45	6.56
s^E_{11}	s^E_{12}	s^E_{13}	s^E_{33}	s^E_{44}	s^E_{66}
82.0	-29.1	-51.5	110	16.4	15.2
s^D_{11}	s^D_{12}	s^D_{13}	s^D_{33}	s^D_{44}	s^D_{66}
59.0	-52.1	-4.17	12.8	15.5	15.2

Dielectric Constants: ε (ε_0), β ($10^{-4}/\varepsilon_0$)

ε^S_{11}	ε^S_{33}	ε^T_{11}	ε^T_{33}
2848	620	3012	6089
β^S_{11}	β^S_{33}	β^T_{11}	β^T_{33}
3.51	16.1	3.32	1.64

Piezoelectric Constants: e (C/m^2), d (10^{-12}C/N) g (10^{-3} m^2/C) and h (10^8N/C)

e_{15}	e_{31}	e_{33}	d_{15}	d_{31}	d_{33}
9.39	-9.15	12.2	154	-1100	2300
g_{15}	g_{31}	g_{33}	h_{15}	h_{31}	h_{33}
5.78	-20.7	42.5	3.73	-16.7	22.3

Electromechanical Coupling Constants:

k_{15}	k_{31}	k_{33}
0.23	0.53	0.94

Density: $\rho = 8315$ g/cm^3

Table IV Measured Material properties of PZN-4.5%PT Single Crystal

Elastic Constants: c_{ij} (10^{10}C/m^2) s_{ij} (10^{-12} C/N)

c^E_{11}	c^E_{12}	c^E_{13}	c^E_{33}	c^E_{44}	c^E_{66}
10.7	9.82	10.7	12.4	6.48	7.32
c^D_{11}	c^D_{12}	c^D_{13}	c^D_{33}	c^D_{44}	c^D_{66}
12.3	11.5	9.24	13.8	6.72	7.32
s^E_{11}	s^E_{12}	s^E_{13}	s^E_{33}	s^E_{44}	s^E_{66}
83.0	-34.4	-41.8	80.0	15.4	13.6
s^D_{11}	s^D_{12}	s^D_{13}	s^D_{33}	s^D_{44}	s^D_{66}
63.1	-54.3	-5.9	15.2	14.9	13.7

Dielectric Constants: ε (ε_0), β ($10^{-4}/\varepsilon_0$)

ε^S_{11}	ε^S_{33}	ε^T_{11}	ε^T_{33}
2988	856	3099	5242
β^S_{11}	β^S_{33}	β^T_{11}	β^T_{33}
3.346	11.67	3.227	1.908

Piezoelectric Constants: Piezoelectric Constants: e (C/m^2), d (10^{-12}C/N), g (10^{-3} m^2/C) and h (10^8N/C)

e_{15}	e_{31}	e_{33}	d_{15}	d_{31}	d_{33}
7.97	-11.2	9.91	123	-962	1734
g_{15}	g_{31}	g_{33}	h_{15}	h_{31}	h_{33}
4.48	-20.7	37.4	3.01	-14.8	13.1

Electromechanical Coupling Constants:

k_{15}	k_{31}	k_{33}
0.19	0.49	0.90

Density: $\rho = 8179$ g/cm^3

Table I and Table II show the ultrasonic and resonance measurement results from different samples. It is found that the difference among the measured elastic constants is small, but the difference among the coupling coefficients can be large. Moreover, since s_{33}^E is calculated from $s_{33}^E = s_{33}^D / (1 - k_{33}^2)$, the error of s_{33}^E transferred from the error of k_{33} will be very large. It is easy to derive that the relative error of the s_{33}^E is given by

$$\left|\frac{\delta s_{33}^E}{s_{33}^E}\right| = \left|\frac{2k_{33}\delta k_{33}}{(1-k_{33}^2)}\right|$$

When k_{33} reaches more than 90%, the error of s_{33}^E calculated from this formula will be an order of magnitude larger than the error of k_{33}. For example, if k_{33} is 0.90 with a relative error of 1%, the relative error for s_{33}^E will be about 8.5%.

ANISOTROPY OF MATERIAL PROPERTIES

Unlike PZT ceramics, PZN-PT single crystal is anisotropic in the X-Y plane. Therefore, the analysis of directional dependence of phase velocities and electromechanical coupling coefficients will be very helpful to understand the properties of PZN-PT crystals. We have carried out the anisotropy analysis by using the measured data given in Tables III and IV. Figure 4 gives the directional dependence of the phase velocities in the X-Y, Y-Z and [110]-Z planes. All waves propagating in these three planes are anisotropic except the shear wave propagating in the X-Y plane with the displacement polarized in [001]. The calculated results showed that the velocity of the longitudinal wave does not change significantly when the propagation direction is perpendicular to [001], [100] and [110] directions. The shear wave propagating in the X-Y plane and polarized also in this plane has a strong angular dependence. The phase velocity has a maximum along [100] and a minimum along [110], respectively. The phase velocity of the shear wave propagating in the Y-Z plane and polarized in the same plane also changes drastically with propagation directions. It has a maximum in [001] and a minimum in [011]. Therefore, the error of phase velocity measurement caused by misorientation could be much larger for shear waves than for the longitudinal waves.

The directional dependence of the electromechanical coupling coefficients and velocities of the length extension modes are shown in Figure 5. The electric field is applied in the poling direction which is in the direction parallel to the length of k_{33} bar and perpendicular to the length of k_{31} bar. The coupling coefficient k_{33} has a maximum value when the length is in [001] direction. The coupling coefficient of k_{31} is the largest when the length is perpendicular to [001] and k_{31} reaches its maximum when the length is in [110] direction. This was proved by the measurement results shown in Table II.

Since the formula for the length extension mode is based on the assumption of an infinite thin bar without lateral stress, to produce a pure mode requires a large aspect ratio in order to achieve high accuracy. Figure 6 presents calculated directional dependence of the coupling the coefficients k_{33} and k_t using the measured results in Tables III and IV. Here k_t is the coupling coefficient of the thickness mode for a flat plate. If the length to width ratio of the bar is less than 1, the measured coupling coefficient from the resonance would be closer to k_t rather than k_{33}, and the longitudinal velocity would also increase to approach the velocity of a one dimensional plane wave with constrained lateral dimensions. It can be seen from Fig. 6 that both k_{33} and k_t reach their maximum in [100] direction.

SUMMARY

The material properties of PZN-PT single crystal were measured by using the combined method of ultrasonic and resonance technique. Only [001]/[010]/[100] and [001]/[110]/[1$\bar{1}$0] oriented samples were needed for the measurements. The complete set of elastic, piezoelectric and dielectric constants of PZN-4%PT and PZN-8%PT were determined based on the resonance frequencies and the sound velocities. For PZN-8%PT, k_{33} reached 94% and d_{33} exceeded 2300pC/N. The property is slightly less for the 4.5%PT samples, however, k_{33} is still more than 90%. The directional dependence of the phase velocities of the acoustic waves propagating in the X-Y, Y-Z and [110]-Z planes was calculated based on the measured data. The calculated results showed that the phase velocities are anisotropic except the shear wave propagating in the X-Y plane with displacement along Z-direction. The directional dependence of the electromechanical coupling

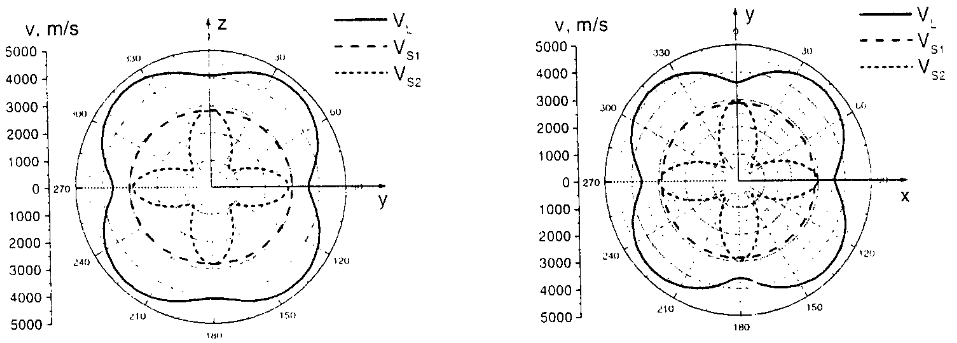

Y-Z plane X-Y plane

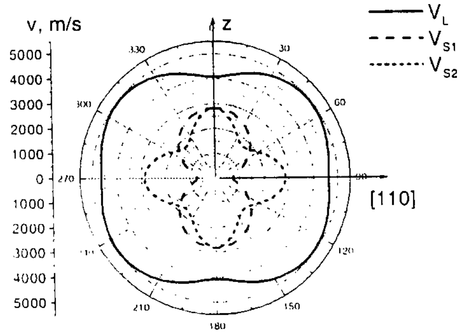

[110]-Z plane

Fig. 4 Orientational dependence of phase velocities in the X-Y, Y-Z, and [110]-Z planes.

coefficients was also calculated based on the measured results. The calculations showed that the maximum value of k_{33} is in the [001] direction while k_{31} was found to have a maximum in [110] direction. These results agree well with our experimental observations.

ACKNOLEDGEMENTS

This research was sponsored by the Office of Naval Research and the National Institute of Health. The crystals used for this study were grown by Drs. Thomas Shrout and S. E. Park through the ONR Piezo-crystal Resource of Penn State.

REFERENCES

1. S.E.Park, and T.R.Shrout, "Characteristics of relaxor-based piezoelectric single crystals for ultrasonic transducers", IEEE Trans. On UFFC **44**, pp1140-1147, 1997.
2. S.E.Park, and T.R.Shrout, " Ultrahigh strain and piezoelectric behavior in relaxor based ferroelectric single crystals", J.Appl.Phys. **82**, pp1804-1811, 1997.
3. S.F.Liu, S.E.Park, T.R.Shrout, and L.E.Cross, "Electric field dependence of piezoelectric properties for rhombohedral $0.955Pb(Zn_{1/3}Nb_{2/3})O_3$-$0.045PbTiO_3$ single crystal", J.Appl.Phys., March 1999, (in press)
4. S. Zhu, B. Jiang and W. Cao, "Characterization of piezoelectric materials using ultrasonic and resonant techniques" Proceedings of SPIE, Medical Imaging 1998, **3341**, pp154-162, 1998.
5. "IEEE standard on piezoelectricity, ANSI/IEEE std, 176-1987", IEEE, New York, 1987.
6. W. Hayers and R. Loudon, "Scattering of light by crystals", John Wiley, New York, pp327-353, 1978.
7. Z.Li, M.Grimsditch, X.Xu and S.K.Chan, "The elastic, piezoelectric and dielectric constants of tetragonal $PbTiO_3$ single crystal", Ferroelectrics, **141,** pp313-325, 1993.

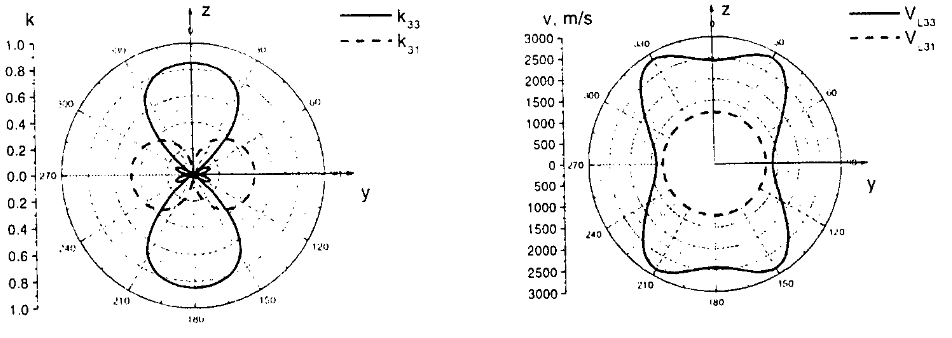

Y-Z plane

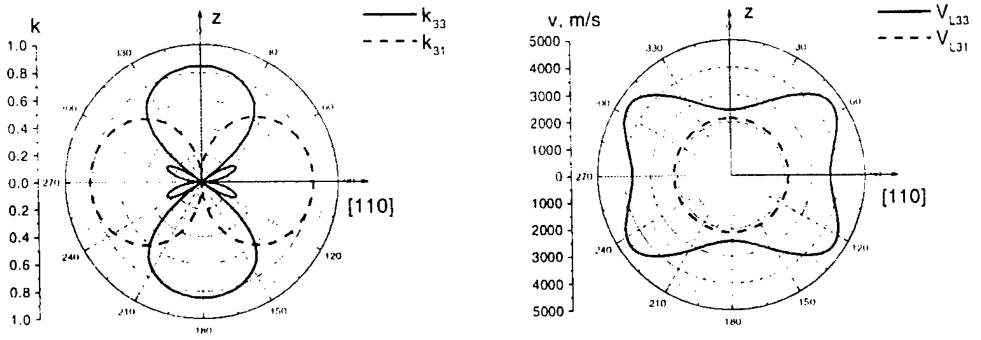

[110]-Z plane

Fig. 5. Directional dependence of coupling coefficients and velocities of length extension modes.

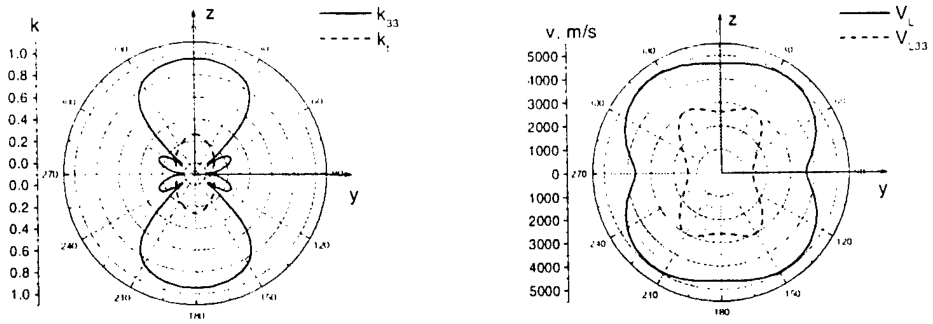

Fig. 6 Directional dependence of coupling coefficients k_{33}, k_{33}, k_{33} in the Y-Z plane.